University of Cyprus

DEPARTMENT OF ELECTRICAL AND COMPUTER ENGINEERING

DESIGN AND IMPLEMENTATION OF QUAD_BAND MICROWAVE DEVICES USING THE NEGATIVE REFRACTIVE INDEX TRANSMISSION- LINE TECHNIQUE

ANDREAS PAPANASTASIOU

A Dissertation Submitted to the University of Cyprus in Partial Fulfillment of the Requirements for the Degree of Doctor of Philosophy

May 2015

VALIDATION PAGE

Andreas Papanastasiou

Design and Implementation of Quad-band Microwave Devices using the Negative Refractive Index Transmission-Line Technique

The present Doctoral Dissertation was submitted in partial fulfillment of the requirements for the Degree of Doctor of Philosophy at the ***Department of Electrical and Computer Engineering****, and was approved on* ***25/05/2015*** *by the members of the* ***Examination Committee***

Research Supervisor ____
George E. Georghiou

Committee Member (Chairperson) ______________________________________
Stavros Iezekiel

Committee Member ____
Georgios Ellinas

Committee Member ____
Anastasis Polycarpou

Committee Member ____
Alexandros Feresidis

DECLARATION OF DOCTORAL CANDIDATE

The present doctoral dissertation was submitted in partial fulfillment of the requirements for the degree of Doctor of Philosophy of the University of Cyprus. It is a product of original work of my own, unless otherwise mentioned through references, notes, or any other statements.

Andreas Papanastasiou

……………………………………………

ABSTRACT

Ο όρος Μεταϋλικά, χρησιμοποιείται για την περιγραφή τεχνητών, σύνθετων, περιοδικών δομών με μέγεθος μικρότερο του μήκους κύματος, οι οποίες έχουν ασυνήθιστες ηλεκτρομαγνητικές ιδιότητες, δηλαδή ταυτόχρονα αρνητική διηλεκτρική σταθερά και μαγνητική διαπερατότητα. Υλικά με τέτοιες ιδιότητες, δεν υπάρχουν στη φύση από μόνα τους. Αυτές οι ιδιότητες επιτρέπουν το σχεδιασμό μικροκυματικών συσκευών που είναι εγγενώς πολυσυχνοτικά και μικρότερα σε μέγεθος από τα συμβατικά αντίστοιχά τους.

Στις πλείστες σύγχρονες ασύρματες συσκευές, η δυνατότητα πολλαπλών συχνοτήτων επιτυγχάνεται χρησιμοποιώντας μία αρχιτεκτονική συνάθροισης υποσυστήματων, στην οποία το κάθε υποσύστημα λειτουργεί σε μία μόνο ζώνη συχνοτήτων. Αυτό το είδος της σχεδιασμού συστημάτων, έχει ως αποτέλεσμα τη χρήση περισσοτέρων στοιχείων, γεγονός το οποίο αυξάνει το κόστος, την πολυπλοκότητα και το μέγεθος της συσκευής. Κατά τη διάρκεια της περασμένης δεκαετίας, οι προσπάθειες για την κατασκευή μικροκυματικών συσκευών που να λειτουργούν σε δύο συχνότητες χρησιμοποιώντας μεταϋλικά ήταν πολλές. Έχει αποδειχτεί ωστόσο ότι ο σχεδιασμός και κατασκευή τετραζωνικών συσκευών, ήταν πιο δύσκολος.

Ο κύριος στόχος αυτής της έρευνας ήταν η σχεδίαση, ανάπτυξη και κατασκευή παθητικών τετραζωνικών συσκευών, χρησιμοποιώντας την τεχνολογία μεταϋλικών, που μπορεί τελικά να χρησιμοποιηθεί σε ένα σύστημα πολλαπλών συχνοτήτων. Ένας άλλος στόχος ήταν να αναπτύξει τη μεθοδολογία σχεδιασμού για την υλοποίηση των τετραζωνικών συσκευών, η οποία είναι απαραίτητη για την εξάπλωση της τεχνολογίας αυτής. Το κίνητρο πίσω από αυτό, είναι το γεγονός ότι κατά την προσπάθεια να σχεδιάσουν πρακτικές και πραγματοποιήσιμες συσκευές, πρέπει κανείς να λάβει υπόψη τις γραμμές μεταφοράς υποδοχής. Σε αντίθετη περίπτωση, απαιτούνται πολλές επαναλήψεις του σχεδιασμού πριν από την επίτευξη των στόχων του σχεδιασμού. Η θεωρία που αναπτύχθηκε, λαμβάνει υπόψη το γεγονός αυτό και η προδιαγραμμένη απόδοση επιτυγχάνεται με μικρές μόνο αλλαγές. Κατά τη διάρκεια της έρευνας αυτής, έχουν σχεδιαστεί και κατασκευαστεί παθητικές τετραζωνικές συσκευές μεταϋλικών, όπως για παράδειγμα διαιρέτες ισχύος, συζεύκτες και φίλτρα, τα οποία αποτελούν αναπόσπαστα τμήματα υποσυστημάτων, όπως μίκτες, ενισχυτές και μετασχηματιστών φάσης. Τα αποτελέσματα της χρήσης της των γραμμών μεταφοράς, δηλαδή της παρασιτικής χωρητικότητας, επαγωγής, αντίστασης και αγωγιμότητας, λαμβάνονται υπόψη και χρησιμοποιώντας τη θεωρία που αναπτύχθηκε, μπορεί να επιτευχθεί πραγματοποιήσιμος σχεδιασμός τετραζωνικών συσκευών μεταϋλικών.

ABSTRACT

Metamaterials is a general term for artificial, composite, subwavelength periodic structures that have unusual electromagnetic properties (simultaneously negative permittivity and permeability) not found in any known media in nature. Such properties enable the design of microwave devices that are inherently multiband and smaller than their conventional counterparts.

In most modern wireless devices, multiband capability is achieved using a stacked architecture of subsystem blocks, each operating at a single frequency band. This type of design results in redundant hardware being used which increases the cost, complexity and size of the device. During the past decade, attempts for constructing dual-band microwave components using metamaterials were numerous. Quad-band devices however have been more challenging to design and fabricate.

The main objective of this research was the design, development and fabrication of passive quad-band components using metamaterial technology which can ultimately be used in a multiband system. Another goal was to establish a design methodology for the realization of quad-band devices which is essential to the spread of this technology. The motivation behind this is the fact that when trying to design practical and realizable devices, one must take into account the effects of the host transmission lines. Otherwise, too many design iterations are required before reaching the design goals. The theory developed takes this into account and performance is achieved with only minor changes. The design of passive metamaterial quad-band components, namely, dividers, rat-race couplers and filters has been performed, which are integral parts of subsystem blocks such as mixers, amplifiers and phase shifters. The effects of parasitic capacitance, inductance, resistance and conductance are all taken into account and using the theory developed, realizable quad-band metamaterial devices can be achieved.

ACKNOWLEDGMENTS

First of all, I would like to sincerely thank my supervisor, Dr. George E. Georghiou, who without his support, this work would have not been completed. Through our stimulating discussions, his constant encouragement and his inspiring personality, he managed to guide me through the long but very fruitful endeavor of this research effort. More importantly, I am grateful for the friendship we developed throughout the years, which I am certain, will be a lasting one.

I would also like to thank Prof. George V. Eleftheriades who laid the foundations in the field of metamaterials and has set the direction for me to follow during the early stages of my PhD degree.

I would also like to thank Dr. Stavros Iezekiel, Dr. George Ellinas, Dr. Anastasios Polycarpou and Dr. Alexandros Feresidis for being members of my Ph.D. examination committee and for providing me with valuable feedback on my thesis.

DEDICATION

I would like to dedicate this work to my mother and to the loving memory of my father, who helped me become who I am and who were always there for me, unconditionally.

I also dedicate this work to my wife Maria, who sacrificed so much time and effort during my long absences from family life, in preparation for this work, throughout the last few years. I wholeheartedly thank you Maria, for your strength and your belief in me.

Contents

List of Figures

List of Tables

Chapter 1

1. Introduction

Metamaterials provide enabling technologies for numerous applications in the field of microwave engineering such as couplers, phase shifters, filters, antennas, imaging systems and even cloaking devices. Substantial work has been made in recent years to fully understand their electromagnetic properties.

The permittivity ε and permeability μ of a material, are the two main parameters used to characterize the electric and magnetic properties of that material. Metamaterials comprise a wide set of artificially structured composites with tunable values of ε and μ that are difficult to obtain with naturally occurring materials. Whereas an ordinary material is made of atoms or molecules, a metamaterial is constructed from lattices of artificial unit cells consisting of subwavelength sized features. If the size and periodicity of the unit cell structure is smaller than the wavelength, the metamaterial can be regarded as homogeneous and its properties can be represented by macroscopic effective material parameters ε and μ.

The development of metamaterials is primarily concerned with the design of appropriate unit cells. This provides the engineer with multiple degrees of freedom and makes it principally possible to engineer a material with desired values of ε and μ. The unit cells and the features that make up a metamaterial unit cell are scalable and can be easily designed to work at different frequency bands. Materials with simultaneously negative values of ε and μ known as negative refractive index (NRI), left-handed (LHM), double negative (DNG) or backward wave materials, represent a special class of metamaterials and form the basis of this thesis.

1.1 Motivation

In recent years, there has been an obvious push towards unified commercial satellite communication systems (e.g. block upconverters, LNBs) that operate simultaneously in the C, X and Ku bands. In addition, there are scientific and military instruments that require multiband capability such as radiometers, scatterometers and radar where the use of multiple frequency bands enables more accurate interpretation of the objects under study. In personal communication systems, devices that combine mobile telephony, multimedia access, GPS capabilities and wi-fi are driven to become smaller and lighter. Today, this property of multi-frequency operation is in many cases achieved using hardware designed at single frequencies or frequency bands closely spaced together. For bands that are further apart a different set of hardware must be used to operate at those frequencies, resulting in a stacked hardware architecture. It is crucial to achieve the above goals using the least possible hardware to keep the cost of such systems low. For commercial wireless devices, cost is the driving factor to the success of a particular device. In the case of the scientific space borne instruments mentioned above, the cost of using multiple receivers to cover each band can become prohibitive and the weight of the system becomes essential to the success of the mission. Considering the above constraints, only by envisioning new devices supporting multi-frequency operation can solutions be found. The idea that materials with negative refractive index would enable applications with non-intuitive characteristics has been around since the 1960's [1]. The application of the negative refractive index or left-handedness (LH) of these new materials to microwave devices has only recently become possible and has been the driving force behind this work, in an attempt to address the constraints and requirements laid out above.

1.2 Electromagnetic Metamaterials

Metamaterials is a general term for artificial, composite but effectively homogeneous subwavelength periodic structures that have unusual electromagnetic properties. A material is effectively homogenous when its structural cell size $d << \lambda_g$, which makes the electromagnetic wave traveling through this material to be "myopic" to the lattice. An effectively homogeneous material can then be described by an effective dielectric permittivity ε and a magnetic permeability μ as is the case for conventional materials.

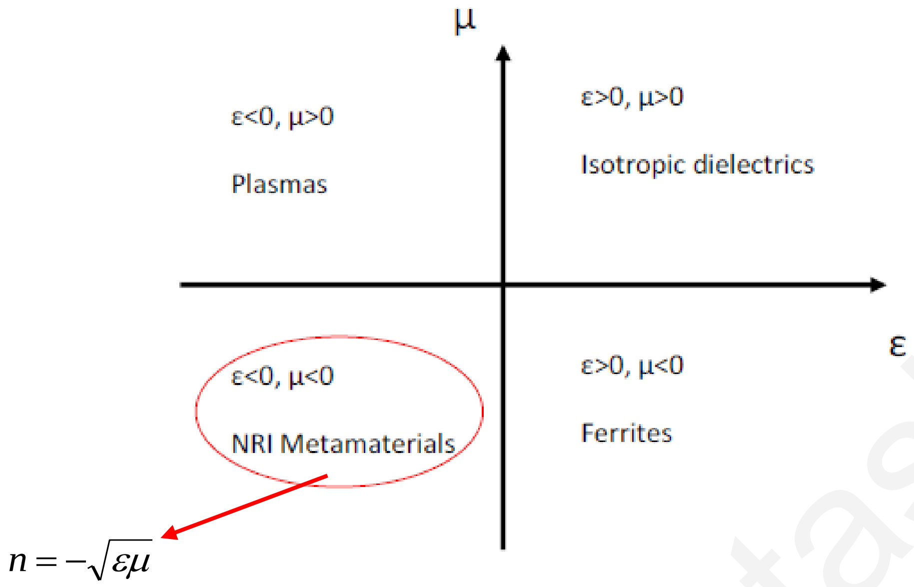

Fig. 1-1. Electromagnetic material classification according to their ε and μ

When both ε and μ are simultaneously negative, as seen in Fig. 1-1, the index of refraction n of the effectively homogeneous material becomes negative, and this material supports left-handed wave propagation. The realization by V. G. Veselago in 1968 that there is nothing prohibitive in Maxwell's equations for a medium to have simultaneously negative permittivity and permeability and thus a negative index of refraction [1], led the way for scientists to begin searching for such materials. Veselago also realized that the electric-field vector E, the magnetic-field vector H and the wave vector k in such media form a left-handed triplet and that the phase and group velocities of a wave in a left-handed medium have opposite signs. In addition he showed that simultaneous negative values of ε and μ can be realized only in dispersive media [1].

Shelby, Smith and Shultz in 2001 were the first ones however, to experimentally verify a negative index of refraction. They presented in [2] a structure that consisted of a two-dimensional array of repeated unit cells of copper strips and split ring resonators on interlocking strips of standard circuit board material. Using this structure, they measured scattering data at microwave frequencies that directly confirmed a negative n.

The problem with negative refractive-index (NRI) metamaterials made from wire strips and split ring resonators is that the choice of operating frequency is limited to that above the ring resonance which requires bulky unit cells. In 2002, Iyer and Eleftheriades proposed that planar transmission line networks that support backward waves and left-handedness can be used to demonstrate negative index of refraction. Such networks are periodically loaded transmission lines (TLs) with capacitive and inductive elements in a high-pass configuration as shown in Fig. 1-2 and Fig. 1-3 [4]. These structures that possess incremental unit length have an equivalent circuit that is the dual of that for a transmission line. In addition, these structures operate at wavelengths much smaller that the unit cell length, thus they can be considered as effective media with negative parameters ε and μ. Because of the TL nature of these metamaterials, the term negative refractive-index TL (NRI-TL) was coined.

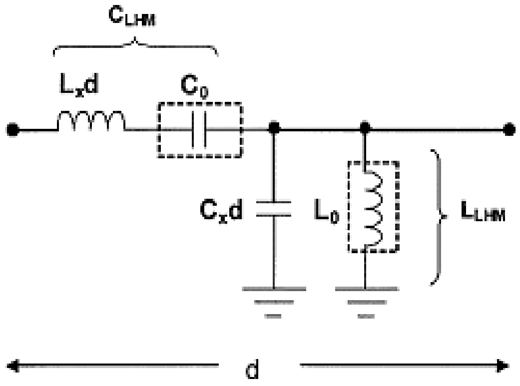

Fig. 1-2. 1-Dimensional TL with loading elements. After [36].

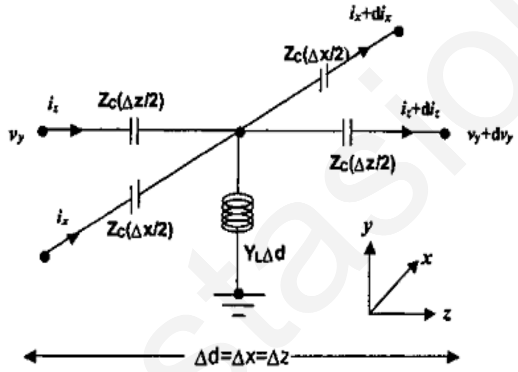

Fig. 1-3. 2-D TL with loading elements. After [4].

The ability to use standard microwave fabrication techniques for constructing metamaterials paved the way to the fabrication of various microwave devices that exploited the unique properties of such effective media. Left-handed wave propagation in electromagnetic media enables the design of microwave devices that are inherently multiband and smaller than their conventional purely right-handed counterparts.

In most modern wireless devices, multiband capability is achieved using a stacked architecture of subsystem blocks, each operating at a single frequency band. This type of design results in redundant hardware being used which increases the cost, complexity and size of the device. During the past decade, attempts for constructing dual-band microwave components using metamaterials were numerous. Quad-band devices however have been more challenging to design and fabricate. This work focuses on the development of the design methodology and the fabrication of quad-band components that can ultimately be used in wireless systems for size, cost and complexity reduction.

1.3 Metamaterial Device Overview

The first device to use metamaterial technology in the microwave region was a phase shifter reported by Antoniades and Eleftheriades in 2003. In [5], a phase shifter that used cascaded sections of NRI metamaterials and positive refractive index (PRI) TLs was proposed that offered significant size advantages and a linear phase response around the design frequency compared to a conventional phase shifter. The proposed phase shifter had the ability to incur positive, negative or 0 degree phase shifts depending on the values of the loading elements and was independent of the size of the structure. The paper showed comparisons of simulated and measured results of single and multi-stage 0 degree and 10 degree metamaterial phase shifters. The linearity the designed phase shifters exhibited around the design frequency also resulted in shorter group delays, a very significant advantage over the traditional delay line phase shifter and a characteristic especially useful in broadband applications. An active, tunable version of a metamaterial phase shifter was reported in [6] which used varactor diodes to load the transmission line and exhibited a linearly tunable performance at C-Band. Other active metamaterial phase shifters reported in the literature were operating at L-Band and used Shottky diodes for its capacitive loading [7] and operating at Ku-Band and used ferroelectric varactors [8].

Islam and Eleftheriades examined a metamaterial coupler that featured co-directional forward traveling waves but contra-directional power flow, resulting in power delivered backwards. It was shown in [9] and [11] that a metamaterial coupler made of a regular microstrip (MS) line and a NRI line has superior performance in terms of coupled power and port isolation when compared to a traditional coupled line microstrip coupler of the same length. Further development led to the publication of [13] , which exhibited a very high isolation of 72 dB and 45 dB of directivity at center frequency.

In [41], a hybrid ring coupler (rat-race) was presented that took advantage of the miniaturization properties of metamaterial transmission lines to design a coupler that was 67% smaller compared to its conventional counterpart operating at the same frequency. This proposed hybrid showed 58% and 49% bandwidth enhancements at 2 GHz in the 180^o out-of-phase and in-phase operations, respectively.

In another publication by Antoniades and Eleftheriades in 2005, a broadband series 1:4 power divider was proposed [12]. In this publication, 0^0 phase shifting metamaterial lines were employed between the output ports in place of the one-wavelength long lines typically used in a conventional transmission line 1:4 series divider. This resulted in a much smaller design, with a 165% increase in the input return loss bandwidth and a 157% bandwidth increase in the through measurements.

Whereas the above attempts in constructing metamaterial devices considered the miniaturization and bandwidth-increase properties of metamaterials, they did not consider the possibility of multiband operation. Caloz and Itoh in [14] first presented a dual-band non-harmonic branch-line coupler (BLC) that is constructed by replacing the branch lines with NRI-TL lines. In Fig. 1-4, the measured performance of the dual-band coupler is shown. The additional band originated from the fact that an arbitrary pair of frequencies can be intercepted by the phase curve at -90^{o} and -270^{o}. Quadrature phase differences were obtained with errors less than 1.5^{o} and an amplitude imbalance less than 0.5 dB in both passbands between S21 and S31 as seen on Fig. 1-5 for the two operating frequencies.

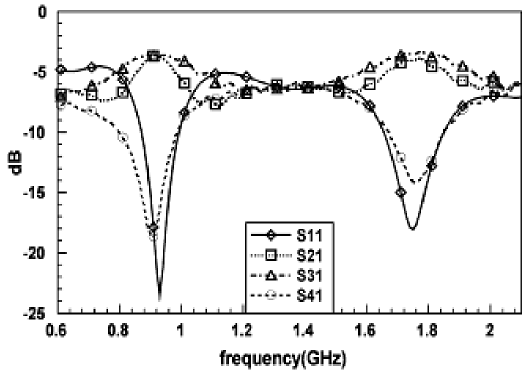

Fig. 1-4. Dual-band branch-line coupler magnitude response. After [14].

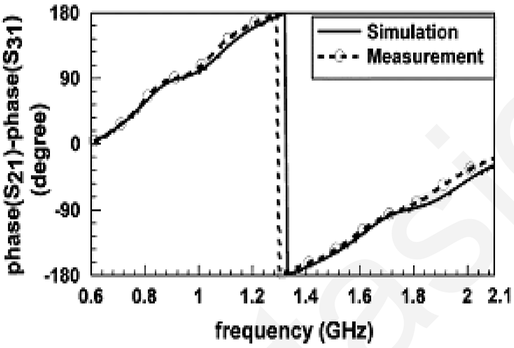

Fig. 1-5 Dual-band branch-line coupler phase response. After [14].

In [15], the fabrication of a dual-band rat race coupler (RRC) was also reported. In that design, the conventional $\lambda/4$ transmission lines that make up the RRC are replaced by NRI-TLs as shown in Fig. 1-6. The operating frequencies for this RRC where chosen to be 1.5 GHz and 3 GHz. The six NRI-TL λ /4 segments of the RRC each operate at two different frequencies, one with a phase response of -90^{o} and the other with a -270^{o} phase response. The measured S-parameters and the phase difference between S_{21} and S_{31} are shown in Fig. 1-7 and Fig. 1-8 respectively.

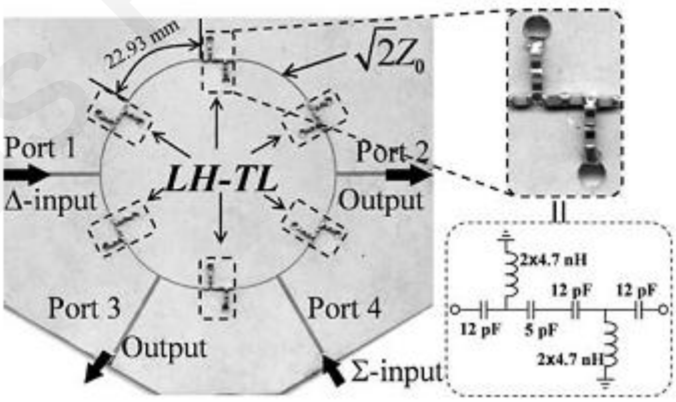

Fig. 1-6 RRC photograph and NRI unit cell schematic. After [15].

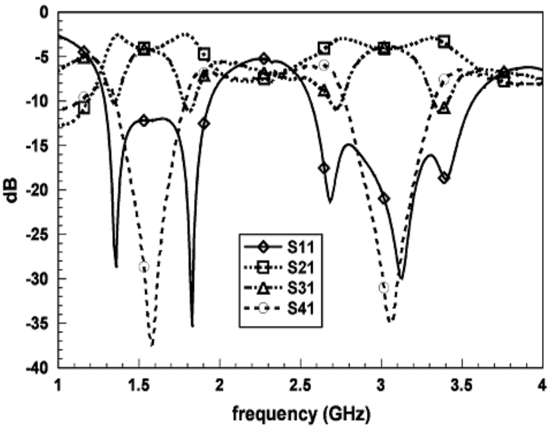

Fig. 1-7. Measured S-Parameters of the dual-band RRC. After [15].

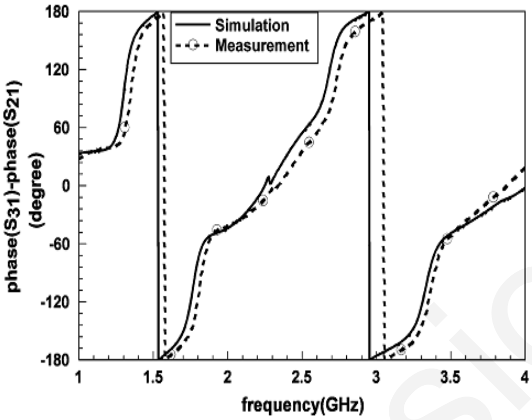

Fig. 1-8. Phase difference between S_{21} and S_{31} of RRC. After [15].

In Fig. 1-8, the phase difference between S_{21} and S_{31} can be observed to be $+180^o$ and -180^o respectively for each operating frequency with phase error less than 4^o. The amplitude imbalance was 0.2 dB or less in both passbands.

The dual-band characteristics of the NRI-TL (otherwise termed as CRLH-TL) were utilized to design dual-band bandpass and bandstop filters in [31]. In this 2006 paper by Tseng and Itoh, the methodology is presented for designing arbitrary frequency dual-band filters based on the replacement of quarter-wave shorted and open-circuited filter sections with NRI-TL sections. By doing so, the complicated dual-band inverter design is avoided.

In 2007, Eleftheriades proposed a generalized NRI-TL (GNRI-TL) metamaterial transmission line for dual-band and quad-band applications. Using a new circuit model as shown in [17], Eleftheriades demonstrated that such a generalized NRI-TL could be used for a variety of microwave components, including filters, branch-line couplers, and dividers. Indeed, this paper represented a breakthrough in the further development of the theory of quad-band NRI-TL unit cells and components and has been referenced extensively in the literature.

A very interesting application of the dual-band NRI-TL branch-line coupler was published in [21]. A group from the Universitat Autònoma de Barcelona presented a dual-band mixer using composite right/left handed transmission lines. The authors of [21], used the schematic shown in Fig. 1-9 to construct the dual-band mixer, which operated at 860 MHz and 2.15 GHz. A typical balanced mixer consists of two or more identical single-ended mixers with a 3 dB hybrid junction. This mixer, used a 180^o 3 dB hybrid implemented by the branch-line coupler with the addition of a 90^o transmission line at one of the outputs. The branch-line coupler was used to feed the RF and LO signals towards the mixer diodes, while at the same time providing the necessary port isolation. The LO and RF branches were both split into two branches with 180^o phase difference. The measured results for this metamaterial mixer agreed well with the simulated results. Fig. 1-11 shows that the RF-LO port isolation was higher than 35 dB at the first frequency and higher than 21 dB at the second. In addition, Fig. 1-12 shows that the conversion loss for the mixer when used as an upconverter is less than 8.5 dB. This measurement was performed by injecting a 13 dBm LO signal at 860 MHz and 2.15 GHz and sweeping a 0 to 400 MHz signal into the IF port at -10 dBm. The operating bandwidth can be seen to be around 220 MHz. Similar results were obtained when the mixer is used as a down-converter.

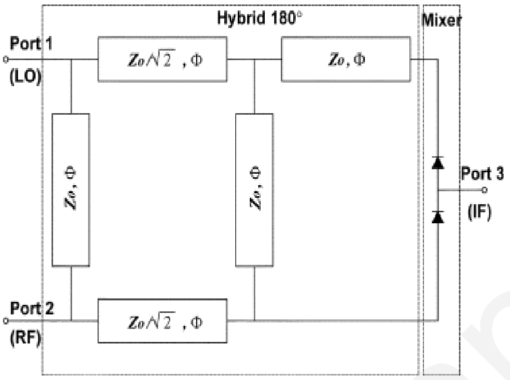

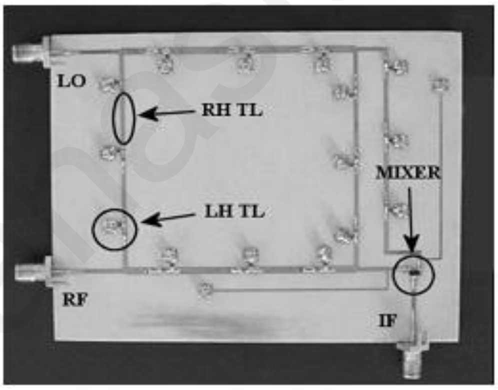

Fig. 1-9. Conceptual schematic of the dual-band mixer. After [21].

Fig. 1-10. Photograph of the fabricated dual-band mixer. After [21].

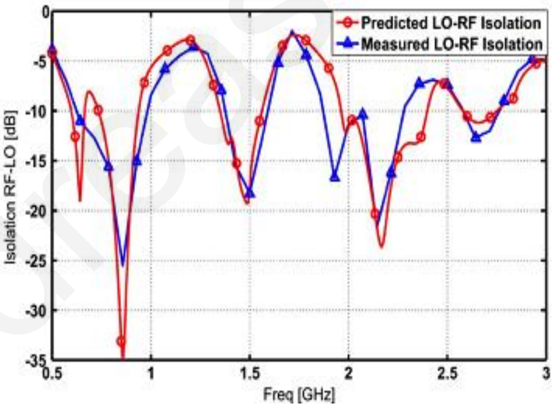

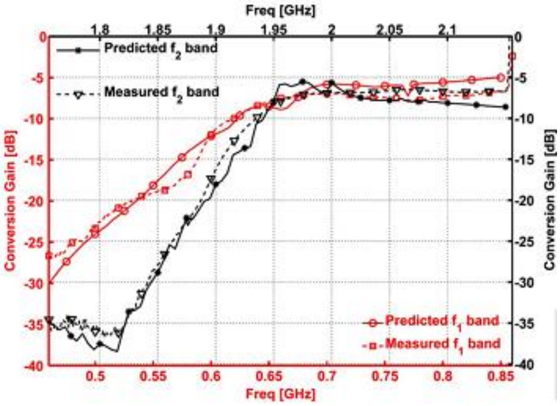

Fig. 1-11. Simulated and measured LO-RF port isolation for the dual-band mixer. After [21].

Fig. 1-12. Simulated and measured conversion loss for dual-band mixer when used as an up-converter. After [21].

In 2008, Pei-Ling Chi, Cheng-Jung Lee and Tatsuo Itoh, published a paper titled “A Compact Dual-Band Metamaterial-Based Rat-Race Coupler for a MIMO System Application” [22]. In this paper, by using composite right/left-handed (CRLH) transmission lines (TLs) and investigating all possible combinations of phase responses of the individual TLs in the coupler, a dual-band and miniaturized rat-race coupler was implemented. This dual-band rat-race coupler showed a 55% size reduction. This metamaterial-based coupler was then used as a mode decoupling network in a dual-band front-end MIMO system, along with a planar antenna array, to split two orthogonal radiation modes from the connected array. A pair of compact dual-band antennas was built and closely spaced to demonstrate pattern diversity by in-phase or out-of-phase excitations from the coupler. Good experimental isolation of the system, -29 dB at 2.4GHz and -34.2 dB at 5.2 GHz, was exhibited verifying the desired decoupling property.

Another way of implementing metamaterial transmission lines is with the use of complementary spit ring resonators (CSRRs), which were introduced by Falcone *et al*. in 2004 as new resonant particles for the synthesis of metamaterials with negative effective permittivity [77]. It was demonstrated that by etching these elements in the ground plane of a microstrip line, the structure was able to inhibit signal propagation in the vicinity of their resonance frequency. Later, the first left-handed line based on CSRRs was implemented by etching series capacitive gaps in the conductor strip, above the positions occupied by the CSRRs [78]. The series gaps were then responsible for the negative effective permeability of the structure. Thus by combining these elements (gaps and CSRRs), a narrow band with simultaneously negative permittivity and permeability appeared in the vicinity of the resonance frequency of the resonators and, hence, a left-handed behavior in that band. Such CSRRs were used in 2008 to implement a dual-band 1:2 Y-junction power divider as reported in [80]. For this divider, the CSRRs shown in Fig. 1-13, impedance inverters were designed at 35.35 Ohms to provide a -90^0 and $+90^0$ phase shift at 0.9 GHz and 1.8 GHz.

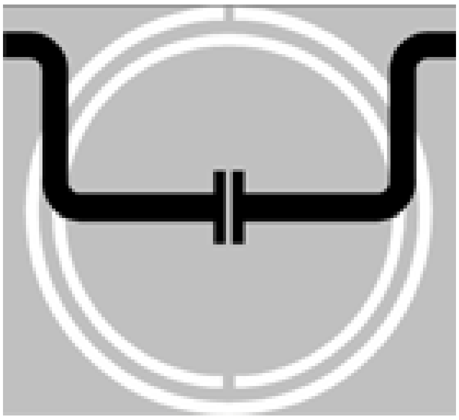

Fig. 1-13 CSRR dual-band quarter-wavelength impedance inverter. After [80].

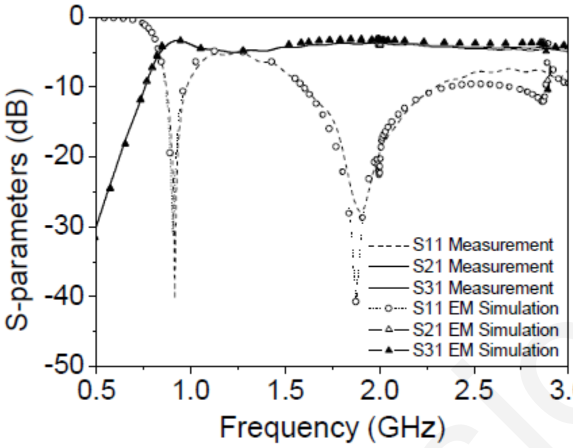

Fig. 1-14. Simulated and measured power splitting (S_{21}, S_{31}) and matching (S_{11}) for the fabricated dual-band CSRR-based power divider. After [80].

The design of another dual-band rat-race coupler using metamaterial transmission lines was proposed in 2009 [23], [24]. This coupler was implemented based on CSRRs. This design used the diplexer action of a pair of CSRR lines, one of them designed to exhibit right-handed wave propagation and the other one left handed wave propagation at the lower and upper frequency bands, respectively.

Based on the GNRI-TL circuit model from [17], F. Martin *et al.* in 2010, implemented a fully planar GNRI-TL unit cell based on CSRRs and open complementary split ring resonators (OCSRRs) [59]. The GNRI-TL component values for each resonator where calculated and curve fitting was subsequently used to obtain the resonator geometries. This unit cell was then used to implement a quad-band Y-junction power divider. The topology of this fully planar unit cell is shown in Fig. 1-15, and the simulated performance in Fig. 1-16.

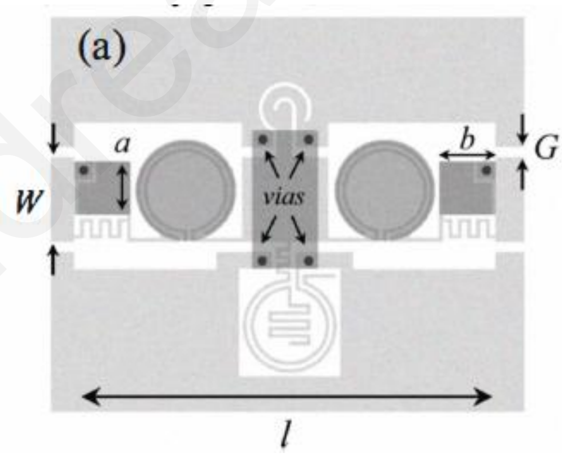

Fig. 1-15. Fully planar GNRI-TL unit cell. After [59].

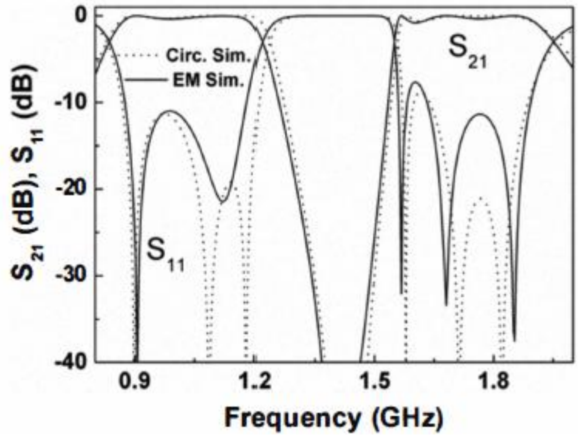

Fig. 1-16. Circuit and EM simulation comparison of insertion and return loss. After [59].

Another fully planar implementation of a quad-band unit cell was reported in 2012 in [63], using a GNRI-TL implementation (Extended CRLH or E-CRLH) using substrate integrated waveguide (SIW), which exhibited lower insertion loss compared to previous fully planar attempts. A Y-junction power divider was then fabricated using this type of unit cell as an impedance inverter.

Metamaterial unit cells have also been implemented in a balanced lattice configuration [72], [73], [90]. These structures however, suffer from difficulties in their manufacturing and are of lesser practical use, due to their balanced nature. Another fully planar implementation of a quad-band GNRI-TL unit cell was published by Ryan and Eleftheriades in 2012, using a bridged-T circuit, resulting in an all-pass performance [64]. In this paper, the transformation from the GNRI-TL configuration of [26] to the bridged-T configuration is shown, using an intermediate lattice structure. The result is a single-ended device that is easier to fabricate compared to lattice equivalent configurations, and shares the all-pass and lower group delay characteristics of the lattice-type arrangement.

A different fabrication technology was used to design a dual-band rat-race coupler in [25] in which half-mode substrate integrated waveguide (HMSIW) transmission lines were used. The CRLH behaviour of the HMSIW TL was obtained by etching the interdigital slot on the waveguide surface. It supports the propagation of the backward wave below the characteristic waveguide cutoff frequency in the left-handed (LH) region and the forward-wave in the right-handed (RH) region.

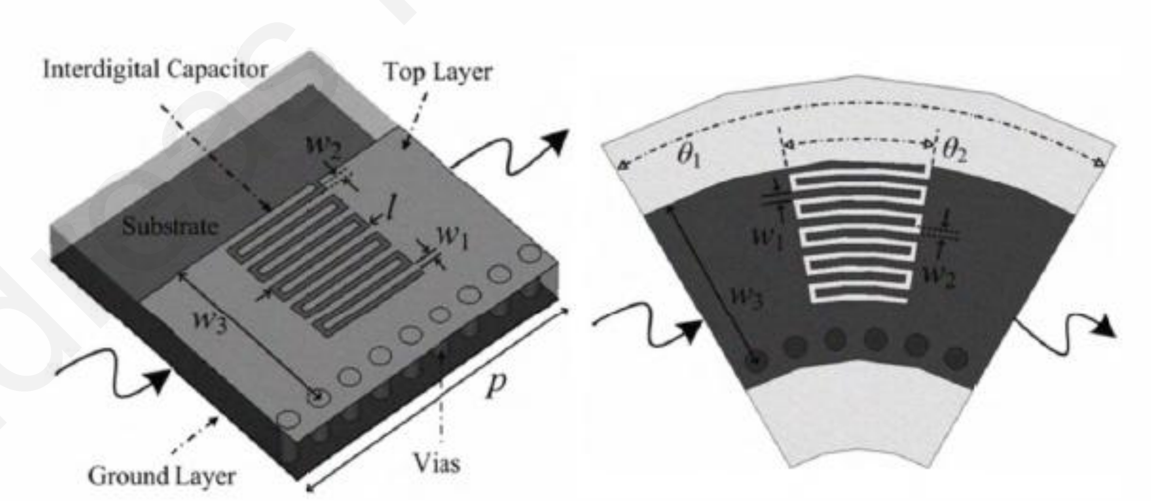

Fig. 1-17 CRLH half-mode substrate integrated waveguide (HMSIW) transmission lines. After [25].

Fig. 1-17 shows the CRLH HMSIW unit cell design used for the fabrication of the rat-race coupler. Other HMSIW metamaterial publications include [75], [76].

Diplexers using metamaterial technology have also been published. In [96], T. Kokkinos *et al.*, reported a fully printed diplexer based on double spiral resonators, and in [97], another diplexer based on NRI-TL lines. In [99] a diplexer based on SIW and CSRR technology was reported, and in [98], [100] and [101], diplexers using the dual-CRLH (D-CRLH) were fabricated.

In a 2011 publication, a novel approach to hybrid multiplexer using CRLH lines was described, where two CRLH lines are connected to two identical dual band filters. These in turn were connected to two broadband hybrid couplers to form one module. By doing this, each module was able to handle two frequencies instead of a single frequency as in conventional systems. This new technique was based on the frequency dispersive characteristic of the CRLH lines. The proposed multiplexer consisted of four channels using two modules at 1.6, 1.9, 2.2, and 2.5 GHz, showing good agreement between simulated and experimental results.

Metamaterials have also found application in many active devices, as can be seen from [102]-[112]. Other interesting applications include a crossover [115], and a frequency doubler [116].

1.4 Research Objectives

The above survey of metamaterial device design and fabrication publications indicates that little has been achieved on the quad-band metamaterial front. Most of the work done is in metamaterial devices operating in only two frequency bands, or that exploits other aspects of the technology, such as the ability to offer broader bandwidths or smaller device sizes. The fact that additional resonators are required for quad-band operation, and the degree of precision that has to be achieved between them, has proven challenging for most of the metamaterial research groups.

With this research, the following goals were attempted to be achieved:

1. To enable successful unit cell designs, the existing GNRI-TL unit cell design theory had to be modified. The existing theory, which enabled the calculation of the required component values for the ideal unit cell schematic, was not adequate for a practical circuit. In other words, in any realizable circuit, the existence of transmission line sections is unavoidable. The effect of these TL sections modifies the characteristics of the ideal unit cell by shifting the target design frequencies and if not accounted for, the design will give poor results. Thus, this research aimed to provide an extension to the existing

theory that incorporates such physical variations to the ideal model. In effect, the actual component values that have to be used for a successful first iteration in the design vary significantly from the ideal component values.

2. Another objective of this work was to create microwave circuit and full-wave electromagnetic models in commercial software packages such as Microwave Office and HFSS, in order to simulate the unit cell's performance under the theory developed and compare it to the ideal and the required performance of the unit cells.

3. The unit cells on their own have little use in wireless systems. In most cases, they have to be used as building blocks of devices that perform specific subsystem functions, such as power division, unbalanced to balanced conversion, filtering and interfacing with the air. The consequence of this reasoning is that a methodology of cascading unit cells must be found, such that the devices achieve the required subsystem design goals, such as functionality, insertion and return loss and insertion phase characteristics. Again, the ideal interconnection varies from the real-world case, and it has to be accounted for as well through proper modeling and simulations.

4. Once the cascading methodology has been found, devices can be designed using the unit cell models and simulations, and these devices can in turn be simulated to estimate performance. Specifically, a quad-band Wilkinson divider, a rat-race coupler, and a bandpass filter have been designed. These are common devices that can find application in most wireless systems.

5. According to the review of the state-of-the-art and the previous work done in this field, no coherent methodology was found to be able to take the high-level requirements of a quad-band metamaterial device and translate them directly into detailed component values, good first design and completed design after only a few iterations. In addition, it was aimed to develop and realize the first ever quad-band GNRI-TL devices using lumped elements.

6. Finally, an objective of this research was to analyze the effects the resistance and conductance have on any realizable GNRI-TL microstrip transmission line device. To achieve this objective, the supporting theory first would have to be developed and subsequently comparative analysis performed through simulations to draw conclusions on the magnitude of these effects on realizable designs.

1.5 Contributions of the Thesis

The main contributions of the thesis can be listed as follows:

- In Chapter 3, the analysis of the NRI-TL unit cell has been extended to the case where the impedances of the input and output series branches of the unit cell are unequal. In this fashion, the asymmetrical NRI-TL unit cell can be used for the design of single-band bandpass filters. Through dispersion analysis, a new dispersion relation has been developed and the equations needed to calculate the required component values presented. Results of two NRI-TL unit cells in a back-to-back configuration are shown and compared to an equivalent Chebyshev filter. Also in Chapter 4, the analysis of an asymmetrical GNRI-TL is performed and new equations presented for the calculation of the dispersion characteristics and component values. A dual-band bandpass filter is simulated using the theory developed.
- In Chapter 4, a quad-band Wilkinson power divider has been designed and tested for the first time, using the extended GNRI-TL theory. Simulated and measured results are shown. In fact, in a paper published in 2008, Papanastasiou, Georghiou and Eleftheriades realized for the first time a metamaterial quad-band device that used such GNRI-TL unit cells for the design of a quad-band Wilkinson power divider [18]. Details on this device are given below, as part of the work performed. This paper has been cited numerous times [53]-[63], in further attempts in the design of multiband metamaterial devices.
- A GNRI-TL quad-band rat-race coupler has also been implemented for the first time and results are presented. Another contribution of Chapter 4 is the design of a quad-band shorted λ/4 bandpass filter using GNRI-TL unit cells.
- In Chapter 5, a complete model of the GNRI-TL unit cell is presented, which includes the effects of a realistic host transmission line, including its resistance and conductance. After the host transmission parameters are evaluated, an equivalent model is created to verify its validity and its dispersion characteristics analyzed. Subsequently, a method is shown for making all the necessary corrections to the original GNRI-TL unit cell, using new equations that keep the unit cell in the closed stopband condition. Example designs are calculated and the effects of the transmission line parameters that cannot be rectified are quantified.

- The advantages of designing and implementing metamaterial devices using the GNRI-TL technique as developed in this Thesis, are the following:
    1. The inherent multiband feature of the unit cells can readily be applied to replace conventional transmission line sections of standard designs in a very straightforward fashion. There is no need for convoluted geometrical features such as multiple stubbing in order to make a design multiband as in the current state-of-the-art. This results in a reduction in the overall design complexity.
    2. The arbitrary phase-shifting feature of GNRI-TL unit cells leads to very significant miniaturization of the devices that use them and are limited only by the physical size of the components or resonators used in the design and not on the natural transmission-line phase shift as in the case for conventional designs. By taking advantage of this feature the resultant designs are lighter and occupy less board real-estate. This in turn results in cost and weight savings, both of which are important in today’s wireless devices.
    3. The equations developed provide a useful tool for the designer to go from simulation to implementation without multiple iterations by making the necessary corrections needed for realizable designs and taking into account the expected losses that will result from using the GNRI-TL unit cells.

1.6 Outline of the Thesis

In the second chapter of the Thesis, the negative refractive-index transmission line theory is derived starting from basic electromagnetic theory. The complete analogy between a TEM wave traveling in dielectric media and a TEM wave traveling in a two-conductor transmission line is presented and through this analogy, circuit analysis techniques are used to derive the wave’s phase and group velocity. Using the definitions of refractive-index, the negative index of refraction is justified from the negative phase velocity for NRI and NRI-TL media.

Also in Chapter 2, the GNRI-TL theory is presented. The closed-stopband condition is derived from the dispersion relation and the relationship between the impedances of the horizontal and vertical branches of the unit cell. Equations that yield the constituent component values are also derived.

In Chapter 3, a new NRI-TL unit cell is presented, that features different input and output impedances. The new dispersion relation for this unit cell is derived along with the new relationship between the impedance and admittance of the horizontal and vertical branches of the unit cell respectively. The unit cell’s component values are obtained from new equations that keep the closed stopband condition. An example unit cell is designed and subsequently a back-to-back configuration of two asymmetrical unit cells is simulated in a configuration of a typical 5-pole bandpass filter. The simulated results are compared to the simulated results of a standard 5-pole Chebyshev filter using classical filter theory. The two sets of results are shown to be nearly identical, which proves the applicability of such an asymmetrical unit cell in single-band bandpass filter applications.

Also in Chapter 3, new equations yielding the component values of an asymmetrical GNRI-TL unit cell are presented. These equations are derived using the same methodology as for the NRI-TL unit cell and an example is shown on how a dual-band asymmetrical GNRI-TL bandpass filter can be constructed.

Chapter 3 also expands on the existing GNRI-TL theory by means of adding into the GNRI-TL unit cell model, the host transmission lines using the line impedance and phase shift method and presenting the new dispersion relation that accounts for these host transmission lines.

In Chapter 4, a novel quad-band Wilkinson power divider is presented. This new type of Wilkinson divider replaces the conventional 70.7 Ohm/ 90^{o} transmission line sections with quad-band GNRI-TL unit cells, each with a Bloch impedance of 70.7 Ohms and a phase shift of 90^{o} at four different frequencies. Simulated and measured results are then compared.

A quad-band rat-race coupler is also presented in Chapter 4. As in the case of the Wilkinson divider, the conventional transmission line sections are replaced by GNRI-TL unit cells of proper impedance and phase shift at four distinct frequencies. The modified GNRI-TL unit cells were designed using the host transmission line circuit parameter method in order to make the necessary component value corrections. Simulated and experimental results of both the single unit cell and the entire coupler are presented and compared.

Chapter 4 also discusses the method for the design of a quad-band shorted $\lambda/4$ 3-pole bandpass filter by means of replacing each transmission line section of the single-band conventional filter with GNRI-TL unit cells. The simulated magnitude and phase results are then shown.

In Chapter 5, a complete GNRI-TL model is shown, that incorporates the host transmission line distributed capacitance, inductance, resistance and conductance. The new dispersion relation is derived and the amount of frequency shift that occurs when trying to realize an ideal GNRI-TL unit cell using host transmission lines is calculated. The theory and the methodology for the rectification of the frequency shift effects are discussed. Finally, the losses incurred by such a realizable unit cell are presented by performing simulations using two typical microwave substrate materials with different loss tangents.

Chapter 6 summarizes the work done and discusses possible future lines of research that could follow the work done in this Thesis.

Chapter 2

2 Negative Refractive-Index Transmission Line Theory

In this Chapter, the negative-refractive-index transmission-line theory is presented. Starting from basic electromagnetic theory, the analogy between a TEM wave traveling in lossless isotropic dielectric media and a TEM wave traveling in a two-conductor transmission-line is established and then is used to derive the refractive-index characteristics of the transmission line. The generalized NRI-TL unit cell is also presented along with the necessary equations that yield the constituent component values of the unit cell.

2.1 Electromagnetic and circuit analysis

Any material supporting wave propagation can be characterized by a dielectric constant ε and a magnetic permeability constant μ. Assuming TEM wave propagation in the z-direction for lossless isotropic dielectric materials belonging to the first quadrant of Fig. 1-1, Maxwell's equations tell us that

$$\frac{dE_x}{dz} = -j\omega\mu H_y \tag{2.1}$$

$$-\frac{dH_y}{dz} = j\omega\varepsilon E_x . \tag{2.2}$$

By differentiating (2.1) and substituting into (2.2) with respect to *z*, we get the one-dimensional Helmholtz equation (2.3) [65]:

$$\frac{d^2E_x}{dz^2} = -\omega^2\varepsilon\mu E_x \tag{2.3}$$

and similarly, by differentiating (2.2) and substituting into (2.1) we get the second Helmholtz equation as:

$$\frac{d^2 H_y}{dz^2} = -\omega^2 \varepsilon \mu H_y \tag{2.4}$$

in which the wave number is defined as

$$k = \omega\sqrt{\mu\varepsilon}\ . \tag{2.5}$$

The wave impedance η is also defined as

$$\eta = \sqrt{\frac{\mu}{\varepsilon}}\ . \tag{2.6}$$

There also exists an interrelationship of the wave equation in perfect dielectric materials with the wave equation in a two-conductor transmission line, as detailed in [65]. Considering the infinitesimally small section Δz of a lossless transmission line and the circuit in Fig. 2-1:

By Ampere's Law,

$$Voltage\ change = \frac{\partial V}{\partial z}dz = -Ldz\frac{\partial I}{\partial t} \tag{2.7}$$

where the voltage $V=V(z,t)$ is a function of both space and time. In the sinusoidal steady-state case however, $V(z,t)=Re\{V(z)\cdot e^{j\omega t}\}$ and the length dz may be cancelled, thus (2.7) becomes

$$\frac{dV}{dz} = -j\omega LI \tag{2.8}$$

and accordingly by Faraday's Law

$$Current\ Change = \frac{\partial I}{\partial z}dz = -Cdz\frac{\partial V}{\partial t} \tag{2.9}$$

In the sinusoidal steady-state case however, $I(z,t)=Re\{I(z)\cdot e^{j\omega t}\}$ and again by cancelling dz, (2.9) becomes

$$\frac{dI}{dz} = -j\omega CV\ . \tag{2.10}$$

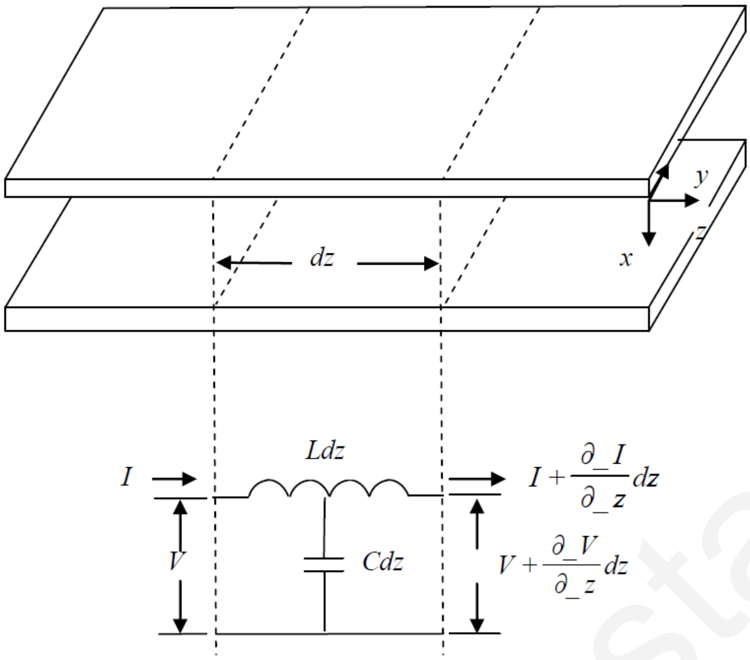

Fig. 2-1. Section of a representative transmission line and its equivalent circuit for a differential length

By taking the derivative of (2.10) and substituting into (2.8) the following relation is derived

$$\frac{d^2V}{dz^2} = -\omega^2 LCV . \tag{2.11}$$

By taking the derivative of (2.8) and substituting into (2.10), a second relation is derived:

$$\frac{d^2I}{dz^2} = -\omega^2 LCI \tag{2.12}$$

(2.11) and (2.11) are the one-dimensional transmission line wave equations (Helmholtz equations) with wave number

$$k = \omega\sqrt{LC} \tag{2.13}$$

and wave impedance

$$Z = \sqrt{\frac{L}{C}} . \tag{2.14}$$

From this discussion, the analogy between the plane-wave solutions and the wave solutions for the ideal transmission line becomes apparent, and in fact it is a complete one, as can be seen tabulated below:

Plane wave solution	Transmission Line solution
$\frac{d^2E_x}{dz^2} = -\omega^2\varepsilon\mu E_x$	$\frac{d^2V}{dz^2} = -\omega^2 LCV$
$\frac{d^2H_y}{dz^2} = -\omega^2\varepsilon\mu H_y$	$\frac{d^2I}{dz^2} = -\omega^2 LCI$
$k = \omega\sqrt{\mu\varepsilon}$	$k = \omega\sqrt{LC}$
$\eta = \sqrt{\frac{\mu}{\varepsilon}}$	$Z = \sqrt{\frac{L}{C}}$

Table 1. Comparison of Plane-wave and transmission line solution parameters

In short, by making the substitutions $\mu\leftrightarrow L$, $\varepsilon\leftrightarrow C$, $E\leftrightarrow V$ and $H\leftrightarrow I$, the one set of equations can derive the other. Through this analogy, Eleftheriades *et. al.* in [4] and [66] realized that since there is nothing prohibitive in Maxwell’s equations for a medium to have simultaneously negative permittivity and permeability and thus a negative index of refraction (according to Veselago [1]), from an impedance point of view, imposing a negative L to obtain a negative μ and a negative C to obtain a negative ε, essentially exchanges their inductive and capacitive roles. This means that the negative series inductor becomes a positive series capacitor, and the negative shunt capacitor becomes a positive shunt inductor. The emerging structure is easily recognized as having the topology of a high-pass filter network, which is the dual of the conventional transmission line. An electrically small section of this sort of transmission line can be seen in Fig. 2-3.

To understand why a negative μ and ε result in a negative refractive index, we consider the following relation for the refractive index [65] :

$$n = \frac{c}{v_p} \tag{2.15}$$

which shows that n is inversely proportional to the phase velocity v_p. If v_p then can take on negative values, which is known to be the case for backward-wave propagation, then n also becomes negative. If we then consider that conventional media with positive μ and ε support propagation with a positive phase velocity and thus a positive refractive index (PRI), then the choice of the sign for the square root in (2.16) has to be the positive one. Conversely, for media with negative μ and ε, the phase velocity v_p is negative and the choice of the sign in (2.16) has to be the negative one to also satisfy (2.15). These media can then be termed negative refractive index (NRI) media.

$$n = \pm\sqrt{\mu\varepsilon} \tag{2.16}$$

From this discussion, a conventional transmission line, as seen in Fig. 2-2, could then be considered as a PRI medium, and its high-pass dual of Fig. 2-3, an NRI medium.

To analyze these two media from an impedance point of view, Kirchhoff's voltage and current laws can be used to these very small sections of transmission lines and perform classical circuit analysis to them. Hence, a simplification of the analysis of these electromagnetic circuits can be achieved, compared to using Maxwell's equations.

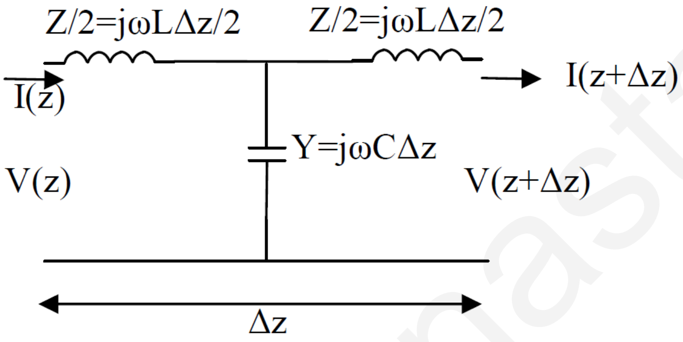

Fig. 2-2. Conventional transmission line model [67]

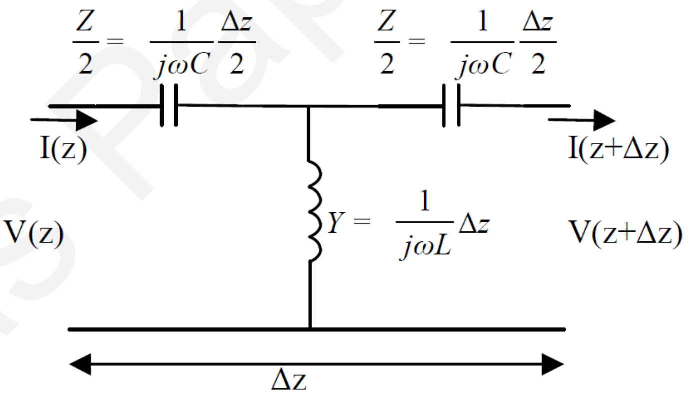

Fig. 2-3. Distributed dual transmission line model [67]

2.1.1 Positive Refractive Index Medium Analysis

Applying Kirchhoff's voltage law to the PRI Medium of Fig. 2-2, we get

$$V(z) - \frac{Z}{2}I(z) - \frac{Z}{2}I(z+\Delta z) - V(z+\Delta z) = 0 \tag{2.17}$$

or

$$V(z) - V(z+\Delta z) = \frac{Z}{2}I(z) + \frac{Z}{2}I(z+\Delta z) \tag{2.18}$$

and from Kirchhoff’s current law,

$$I(z+\Delta z) - I(z) = YV(z) - I(z)\left(\frac{Z}{2}\right)Y\,. \tag{2.19}$$

From the above equations, as Δz→0, we get [65]:

$$\frac{dV(z)}{dz} = -ZI(z) \tag{2.20}$$

$$\frac{dI(z)}{dz} = -YV(z) \tag{2.21}$$

which can be recognized as the Telegrapher’s equations, and subsequently, the wave equations can be constructed from them, as was done previously. Specifically, the wave equations in this case are the following:

$$\frac{d^2V(z)}{dz^2} - ZYV(z) = 0\,. \tag{2.22}$$

$$\frac{d^2I(z)}{dz^2} - ZYI(z) = 0\,. \tag{2.23}$$

In (2.22) and (2.23) the propagation constant (wave number) is simply $\gamma = \alpha + j\beta = \sqrt{ZY}$, which for a lossless medium (α=0) becomes

$$\beta = - j\sqrt{ZY} \tag{2.24}$$

and since *Z=jωL* and *Y=jωC*, the propagation constant becomes

$$\gamma = j\beta = j\omega\sqrt{LC}\,. \tag{2.25}$$

The phase velocity for a transmission line is defined as

$$v_p = \frac{\omega}{\beta}\,. \tag{2.26}$$

Hence in the case of the lossless, conventional dispersionless transmission line of Fig. 2-2,

$$v_p = \frac{1}{\sqrt{LC}}\,. \tag{2.27}$$

The group velocity for a transmission line is defined as [65]:

$$v_g = \frac{d\omega}{d\beta} = \left(\frac{d\beta}{d\omega}\right)^{-1} . \tag{2.28}$$

Hence in the case of the conventional transmission line,

$$v_g = \frac{1}{\sqrt{LC}} . \tag{2.29}$$

It can be seen from (2.27) and (2.29) that both phase and group velocities are positive, as expected.

2.1.2 Negative Refractive Index and NRI-TL Medium Analysis

To perform the same analysis for the NRI Medium, we start by realizing that the topology of Fig. 2-3 is the same as that of Fig. 2-2, so applying Kirchhoff's voltage and current laws would result in the same results for the Telegrapher's and wave equations from an impedance perspective.

For NRI media however, $Z=1/j\omega C$ and $Y=1/j\omega L$, so the propagation constant becomes [65]:

$$\gamma = j\beta = \sqrt{ZY} = \sqrt{\frac{1}{j\omega C}\frac{1}{j\omega L}} = \frac{-j}{\omega\sqrt{LC}} \tag{2.30}$$

The phase velocity is

$$v_p = \frac{\omega}{\beta} = -\omega^2\sqrt{LC} \tag{2.31}$$

and the group velocity is

$$v_g = \frac{d\omega}{d\beta} = \omega^2\sqrt{LC} . \tag{2.32}$$

It can be seen from (2.31) and (2.32) that phase velocity is negative and group velocity is positive, as expected from a medium supporting backward waves. A typical ω-β diagram showing just this, can be seen in Fig. 2-4. A structure then of the form shown in Fig. 2-3 can have a negative refractive index.

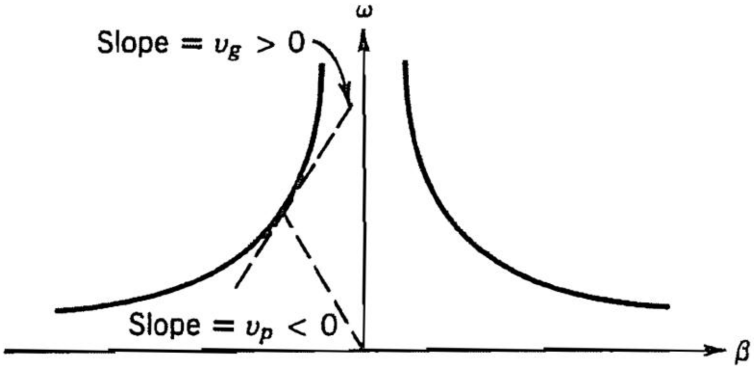

Fig. 2-4 ω-β (dispersion) diagram for an NRI medium

The important novelty of [4] and [66], lies with the fact the PRI and NRI media could be combined and realized in the form of loading a microstrip transmission line (which is the PRI medium) with series capacitors and shunt inductors, to create the negative-refractive index transmission-line (NRI-TL), through which many important improvements to conventional microwave technologies could be achieved. The idea was that the NRI-TL can behave in many ways like a conventional section of a transmission line, while at the same time having other important properties such as both a frequency dependant positive or negative refractive index. A very small section of an NRI-TL would have a circuit diagram such as the one shown in Fig. 2-5 and can also be termed as an NRI-TL unit cell.

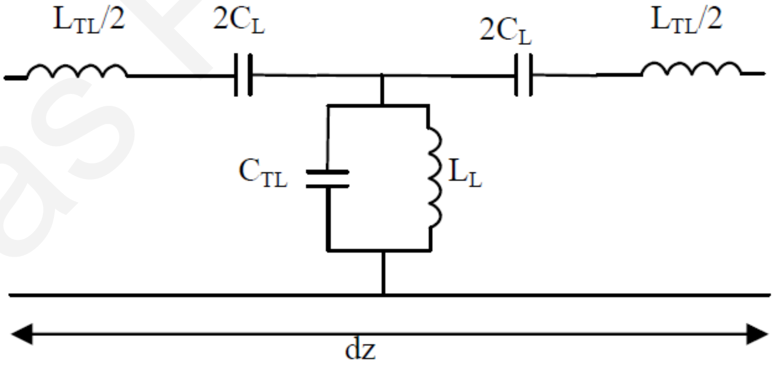

Fig. 2-5. NRI-TL circuit representation

The inductor L_{TL} and capacitor C_{TL} represent the distributed inductance and capacitance of the transmission line and the capacitance C_L and inductance L_L are the loading elements. A dispersion diagram of such a unit cell can be seen in Fig. 2-6 [36]. In this graph, the frequencies where the refractive index is positive (RH passband) and negative (LH passband) can clearly be seen. The stopband region in-between is also identified.

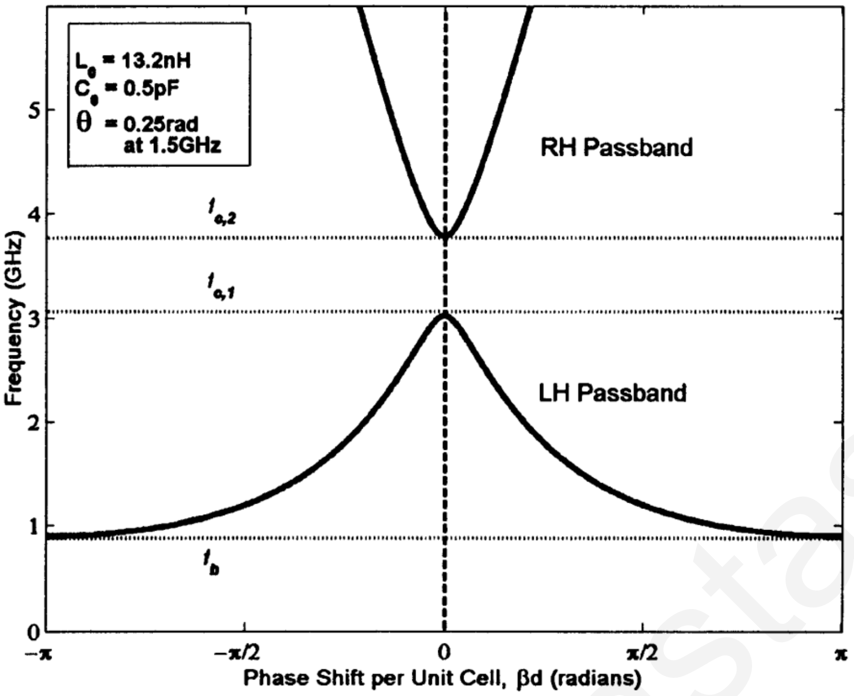

Fig. 2-6. Typical dispersion diagram for an NRI-TL unit cell

2.2 Generalized Negative-Refractive-Index Transmission-Line (GNRI-TL) Theory

Through the publication of [17] in 2007 by Prof. Eleftheriades, it was realized that the way to extend the applicability of the NRI-TL unit cell of Fig. 2-5 to quad-band applications, was to add a parallel LC resonator in the horizontal branch of the NRI-TL unit cell and a series LC resonator in the vertical branch of the unit cell. This configuration, as shown in Fig. 2-7, leads to a periodic artificial line which yields two pairs of alternating backward-wave/forward-wave bands in the first Brillouin zone (BZ) instead of just one pair as in the plain NRI-TL. By inserting additional pairs of parallel resonators in the horizontal branch and series resonators in the vertical branch, further pairs of backward/forward bands can be added, resulting in a multiband operation.

The first step in designing quad-band GNRI-TL metamaterial unit cells is to be able to calculate the component values required for its desired operation. The inputs to this process are the desired four frequencies of operation and the desired insertion phase shift that we need at those frequencies. Fig. 2-7 shows the schematic of a typical Generalized NRI-TL unit cell.

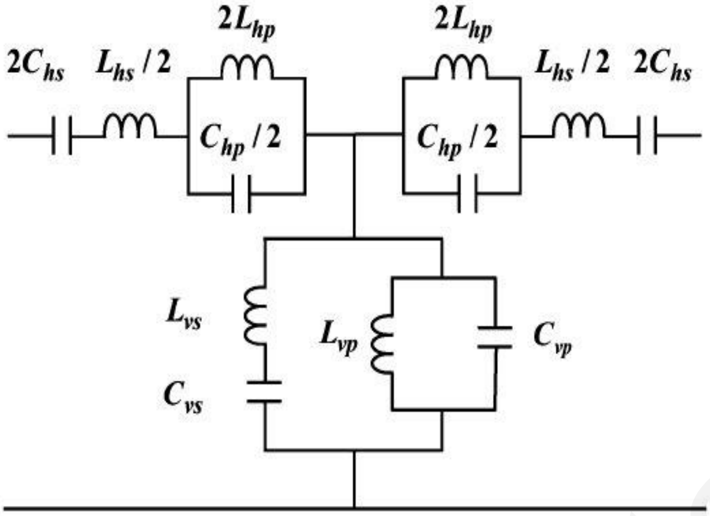

Fig. 2-7. Generalized NRI-TL circuit Model. After [17].

To begin with the design process, as outlined in [26], the circuit of Fig. 2-7 can be represented by the following two-port network, which has the ABCD matrix of (2.33).

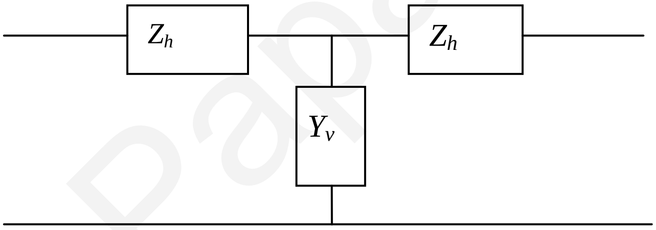

Fig. 2-8. Two-port impedance network representation of the circuit of Fig. 2-7.

The ABCD matrix of the above two-port circuit is given by the well-known relation [42] :

$$\begin{bmatrix} A & B \\ C & D \end{bmatrix} = \begin{bmatrix} 1 + Z_h Y_v & Z_h (2 + Z_h Y_v \\ Y_v & 1 + Z_h Y_v \end{bmatrix} \tag{2.33}$$

where in the case of the Generalized NRI-TL unit cell,

$$Z_h = j\omega L_{hs}/2 + \frac{1}{j\omega 2C_{hs}} + \frac{1}{j\omega C_{hp}/2 + \frac{1}{j\omega 2L_{hp}}} \tag{2.34}$$

and

$$Y_v = j\omega C_{vp} + \frac{1}{j\omega L_{vp}} + \frac{1}{j\omega L_{vs} + \frac{1}{j\omega C_{vs}}}. \tag{2.35}$$

Considering that the resonant frequencies of the resonators in the circuit are described by :

$$\omega_{hs}^2 = 1/\sqrt{L_{hs}C_{hs}} \tag{2.36}$$

$$\omega_{hp}^2 = 1/\sqrt{L_{hp}C_{hp}} \tag{2.37}$$

$$\omega_{vp}^2 = 1/\sqrt{L_{vp}C_{vp}} \tag{2.38}$$

$$\omega_{vs}^2 = 1/\sqrt{L_{vs}C_{vs}} \tag{2.39}$$

Then, Z_h and Y_v can be rewritten as

$$Z_h = j\omega L_{hs}/2(1 - \frac{\omega_{hs}^2}{\omega^2}) - \frac{j}{\omega C_{hp}/2(1 - \frac{\omega_{hp}^2}{\omega^2})} \tag{2.40}$$

$$Y_v = j\omega C_{vp}(1 - \frac{\omega_{vp}^2}{\omega^2}) - \frac{j}{\omega L_{vs}(1 - \frac{\omega_{vs}^2}{\omega^2})}. \tag{2.41}$$

From the theory on the analysis of infinite periodic structures, for the case of a nonattenuating, propagating wave on the periodic structure, the corresponding Bloch propagation constant (dispersion relation) of the above unit cell, is given by the following equation:

$$\cos\beta d = (\frac{A+D}{2}) \tag{2.42}$$

By substituting (2.40) and (2.41) into (2.42), we obtain the following dispersion relation:

$$\cos\beta d = 1 + Z_h Y_v. \tag{2.43}$$

Under the closed stopband condition, we get two passbands, separated by a stopband centered at ω_{or}, which is the resonant frequency of the parallel resonator in the horizontal branch of the circuit ω_{hp}, as well as the series resonator in the vertical branch of the circuit ω_{vs}. At the center of the passband, the phase velocity is infinite and this can be expressed as the frequencies where β=0. The stopband at ω_{or} is created when the vertical branch becomes short circuited and the horizontal branch becomes open circuited. This means that at the stopband, there is no propagation and this can be expressed as the frequencies where

β is infinite. By (2.43), the β=0 frequencies are found by if we set $Z_h = 0$ and $Y_v = 0$. To find the frequencies where $Z_h = 0$ and $Y_v = 0$, we set (2.40) and (2.41) equal to zero, resulting in the following equations [26]:

$$\omega_{hor\_zero} = 0.5(\omega_{hp}^2 + \omega_{hs}^2 + \omega_{hshp}^2) \pm 0.5\sqrt{(\omega_{hp}^2 + \omega_{hs}^2 + \omega_{hshp}^2)^2 - 4\omega_{hs}^2\omega_{hp}^2} \quad (2.44)$$

where

$$\omega_{hshp}^2 = 4 / L_{hs}C_{hp} \quad (2.45)$$

$$\omega_{ver\_zero} = 0.5(\omega_{vs}^2 + \omega_{vp}^2 + \omega_{vsvp}^2) \pm 0.5\sqrt{(\omega_{vs}^2 + \omega_{vp}^2 + \omega_{vsvp}^2)^2 - 4\omega_{vs}^2\omega_{vp}^2} \quad (2.46)$$

where

$$\omega_{vsvp}{}^2 = 1/L_{vs}C_{vp} \quad (2.47)$$

By setting these two sets of zero frequencies equal, we get the closed stopband condition, when

$$\omega_{hp} = \omega_{vs} = \omega_{or} \quad (2.48)$$

$$\omega_{hs} = \omega_{vp} \quad (2.49)$$

$$\omega_{hshp} = \omega_{vsvp} \text{ or } \frac{L_{hs}C_{hp}}{4} = L_{vs}C_{vp} \quad (2.50)$$

Equation (2.50), defines the center of the stopband that separates the two passbands. This can be seen by inspection of Fig. 2-7, where at the frequency ω_{or} the parallel resonator in the horizontal branch becomes open circuited and the series resonator in the vertical branch becomes short circuited. The passband centers are defined by equation (2.47), which are defined at the frequencies where β=0.

In addition, as a result of equations (2.48)-(2.50), the impedance of the horizontal branch Z_h and the admittance of the vertical branch Y_v become equal within a constant, defined below by the calculation of the Bloch impedance of the circuit.

Again, from the analysis of periodic structures, we know that

$$Z_{Bloch} = \frac{A - D + \sqrt{(A+D)^2 - 4}}{2C}. \quad (2.51)$$

By substitution of the ABDC parameters, we then obtain

$$Z_{Bloch} = \sqrt{\frac{Z_h}{Y_v}}\sqrt{2 + Z_{hY_v}} \cdot \tag{2.52}$$

At around the β=0 frequencies, (2.52) becomes:

$$Z_{Bloch} \approx \sqrt{\frac{2Z_h}{Y_v}} \tag{2.53}$$

$$\Rightarrow 2Z_h = Z_{Bloch}Y_v \tag{2.54}$$

$$\Rightarrow 2Z_h = qY_v \tag{2.55}$$

where $q = Z_{Bloch}$ is the Bloch impedance at the centers of the passbands where *β=0*. Substituting (2.40) and (2.41) into (2.53), results in the following expression:

$$Z_{Bloch} \approx \sqrt{\frac{L_{hs}}{C_{vp}}} \cdot \tag{2.56}$$

From (2.43) and (2.55),

$$A^2 = -\frac{2(1-\cos\beta d)}{(q)^2} = -Y_{vp}{}^2 \,. \tag{2.57}$$

From (2.35) and (2.55), the following polynomial is established [2]:

$$\omega^4 - \frac{A}{C_{vp}}\omega^3 - (\omega_{or}^2 + \omega_{vp}^2 + \omega_{vsvp}^2)\omega^2 + \frac{A\omega_{or}^2}{C_{vp}}\omega + \omega_{or}^2\omega_{vp}^2 = 0 \cdot \tag{2.58}$$

The above polynomial has the four roots, *-ω_1, ω_2, -ω_3, ω_4*. Therefore, the polynomial yields four equations for the four unknowns *C_{vp}, ω_{or}, ω_{vp}, ω_{vsvp}*. By relating the known roots to the polynomial coefficients, we get:

$$C_0 = \omega_1\omega_2\omega_3\omega_4 = \omega_{or}^2\omega_{vp}^2 \tag{2.59}$$

$$C_1 = (-\omega_1 + \omega_2 - \omega_3 + \omega_4) = \frac{A}{C_{vp}} \tag{2.60}$$

$$C_2 = (\omega_1\omega_2 \quad \omega_1\omega_3 + \omega_1\omega_4 + \omega_2\omega_3 \quad \omega_2\omega_4 + \omega_3\omega_4) = (\omega_{or}^2 + \omega_{vp}^2 + \omega_{vsvp}^2) \tag{2.61}$$

$$C_3 = (-\omega_1\omega_3\omega_4 + \omega_2\omega_3\omega_4 - \omega_1\omega_2\omega_3 + \omega_1\omega_2\omega_4) = \frac{A\omega_{or}^2}{C_{vp}} \ . \tag{2.62}$$

From the above four equations, the four unknowns can be solved.

$$C_{vp} = \frac{A}{C_1} \tag{2.63}$$

$$\omega_{or}^2 = \frac{C_3}{C_1} \tag{2.64}$$

$$\omega_{vp}^2 = C_0 \frac{C_1}{C_3} \tag{2.65}$$

$$\omega_{vsvp}^2 = C_2 - \frac{C_3}{C_1} - C_0 \frac{C_1}{C_3} \ . \tag{2.66}$$

Then, the rest of the component values can be evaluated.

$$L_{vp} = \frac{1}{\omega_{vp}^2 C_{vp}} \tag{2.67}$$

$$L_{vs} = \frac{1}{\omega_{vsvp}^2 C_{vp}} \tag{2.68}$$

$$C_{vs} = \frac{1}{\omega_{or}^2 L_{vs}} \tag{2.69}$$

$$L_{hs} = qC_{vp} \tag{2.70}$$

$$C_{hs} = \frac{1}{\omega_{vp}^2 L_{hs}} \tag{2.71}$$

$$C_{hp} = \frac{4L_{vs}C_{vp}}{L_{hs}} \tag{2.72}$$

$$L_{hp} = \frac{1}{\omega_{or}^2 C_{hp}} \ . \tag{2.73}$$

In brief, Equations (2.57), (2.59)-(2.73) is all that is required for calculating the ideal component values, once the four desired frequencies of operation are given and the phase shift at these frequencies. As explained earlier though, attempting to build the unit cell with the calculated component values, will not yield good results due to the interaction of the transmission line parameters with the parameters of the unit cell.

2.3 Summary

In this Chapter, the negative refractive-index transmission line theory was derived starting from basic electromagnetic theory. The complete analogy between a TEM wave traveling in dielectric media and a TEM wave traveling in a two-conductor transmission line was presented and through this analogy, circuit analysis techniques were used to derive the wave’s phase and group velocity. Using the definitions of refractive-index, the negative index of refraction was justified based on the negative phase velocity for NRI and NRI-TL media.

Also in this Chapter, the GNRI-TL theory was presented. The closed-stopband condition was derived from the dispersion relation and the relationship between the impedances of the horizontal and vertical branches of the unit cell. Equations that yield the constituent component values were also derived.

Chapter 3

3 GNRI-TL Theory for filter applications

In this Chapter, the NRI-TL and GNRI-TL theory is developed for unit cells that are asymmetrical in terms of their input and output impedance. The dispersion relations are developed and the equations that provide the values for the required component values under the closed stopband condition are presented. Example simulations for filter applications are used to demonstrate the applicability of such unit cells to the design of single and dual-band filters. Also in this section, the expanded GNRI-TL theory is developed that takes into account the host TL using the impedance and phase-shift method.

3.1 Single band filters using NRI-TL unit cells

To use the NRI-TL unit cell for bandpass filter design purpose, one must use a cascade of asymmetric unit cells (in terms of the input and output impedance values) as the basic building block for such filters. It is well known that filter sections have different characteristic impedances within the same filter, and in order for them to be well matched between them, a unit cell with different input and output impedances must be designed. Such a unit cell is shown in Fig. 3-1.

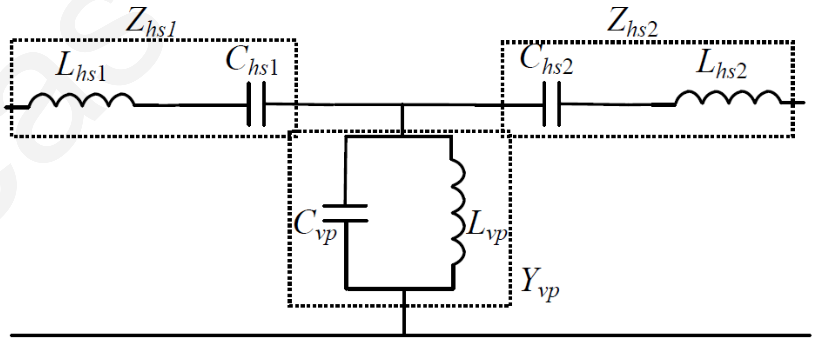

Fig. 3-1 Asymmetric Generalized Dual-Band NRI-TL Unit Cell

From Fig. 3-1, it can be seen that the series parallel resonator and the shunt series resonator have been dropped compared to Fig. 2-7, so that the circuit looks like the NRI-TL unit cell of Fig. 2-5. This unit cell can only be used for single-band bandpass filters, but it serves well for performing the analysis that follows.

Using the same reasoning used previously in the development of the GNRI-TL theory, the ABCD matrix for such a unit cell is given below:

$$\begin{bmatrix} A & B \\ C & D \end{bmatrix} = \begin{bmatrix} (1+Z_{hs1})Y_{vp} & Z_{hs1}+Z_{hs2}+Z_{hs1}Z_{hs2}Y_{vp} \\ Y_{vp} & (1+Z_{hs2})Y_{vp} \end{bmatrix} \tag{3.1}$$

where:

$$Y_{vp} = j\omega C_{vp}(1-\frac{\omega_{vp}^2}{\omega^2}) \tag{3.2}$$

$$Z_{hs1} = j\omega L_{hs1}(1-\frac{\omega_{hs1}^2}{\omega^2}) \tag{3.3}$$

$$Z_{hs2} = j\omega L_{hs2}(1-\frac{\omega_{hs2}^2}{\omega^2}) \tag{3.4}$$

$$\omega_{hs1} = \frac{1}{\sqrt{L_{hs1}C_{hs1}}} \tag{3.5}$$

$$\omega_{hs2} = \frac{1}{\sqrt{L_{hs2}C_{hs2}}} \tag{3.6}$$

and

$$\omega_{vp} = \frac{1}{\sqrt{L_{vp}C_{vp}}} \tag{3.7}$$

which is the resonant frequency of the vertical branch of the unit cell.

The Bloch propagation constant can then be found as follows:

$$\cos\beta d = \frac{A+D}{2} = \frac{1+Z_{hs1}Y_{vp}+1+Z_{hs2}Y_{vp}}{2} = 1+\frac{Y}{2}(Z_{hs1}+Z_{hs2}) \tag{3.8}$$

$$=> Y_{vp} = \frac{2(\cos\beta d-1)}{Z_{hs1}+Z_{hs2}} = -\frac{2(1-\cos\beta d)}{Z_{hs1}+Z_{hs2}} \tag{3.9}$$

Under the closed stopband condition, the resonant frequencies of the horizontal branches are set equal to the resonant frequency of the vertical branch of the unit cell ($\omega_{hs1} = \omega_{hs2} = \omega_{vp}$) which also define the center of the unit cell passband.

At around $\beta \approx 0$ the Bloch impedance is:

$$Z_{Bloch} = \sqrt{\frac{Z_{hs1} + Z_{hs2}}{Y_{vp}}} \tag{3.10}$$

From (3.2), the constant factor between the horizontal impedances and the shunt admittance is given by:

$$=> Z_{hs1} + Z_{hs2} = q^2 Y_{vp} \tag{3.11}$$

where $q = Z_{Bloch}$ at the center of the passband. From (3.10) and (3.1)-(3.3), the Bloch impedance can be written as:

$$Z_{Bloch} = \sqrt{\frac{L_{hs1} + L_{hs2}}{C_{vp}}} \tag{3.12}$$

Thus at the center of the passband,

$$q = \sqrt{q_1 q_2} \tag{3.13}$$

$$q_1 = \sqrt{\frac{L_{hs1}}{C_{vp}}} \tag{3.14}$$

which is the impedance at the input terminal of the unit cell and

$$q_2 = \sqrt{\frac{L_{hs2}}{C_{vp}}} \tag{3.15}$$

which is the impedance at the output terminal of the unit cell. Combining (3.8) and (3.9), results in:

$$Y_{vp}{}^{2} = -\frac{2(1-\cos\beta d)}{(Z_{hs1} + Z_{hs2})^2} = -A^2 \tag{3.16}$$

$$=> Y_{vp}{}^{2} + A^2 = 0 \tag{3.17}$$

$$=> -\omega^2 C_{vp}{}^{2}\left(1 - \frac{\omega_{vp}{}^{2}}{\omega^2}\right) + A^2 = 0 \tag{3.18}$$

$$=> -\omega^2 C_{vp}{}^{2}\left(1 - \frac{2\omega_{vp}{}^{2}}{\omega^2} + \frac{\omega_{vp}{}^{4}}{\omega^4}\right) + A^2 = 0 \tag{3.19}$$

$$=> -\omega^2 C_{vp}{}^{2} + 2\omega_{vp}{}^{2} C_{vp}{}^{2} - \frac{C_{vp}{}^{2}\omega_{vp}{}^{4}}{\omega^2} + A^2 = 0 \tag{3.20}$$

$$=> -\omega^4 C_{vp}{}^{2} + 2\omega^2 \omega_{vp}{}^{2} C_{vp}{}^{2} + \omega^2 A^2 - C_{vp}{}^{2}\omega_{vp}{}^{4} = 0 \tag{3.21}$$

$$=> \omega^4 - \omega^2 (2{\omega_{vp}}^2 + \frac{A^2}{{C_{vp}}^2}) + {\omega_{vp}}^4 = 0 \tag{3.22}$$

which is a biquadratic equation with two positive and two negative roots. To find the roots, we substitute $x=\omega^2$ which results in:

$$x^2 - x(2{\omega_{vp}}^2 + \frac{A^2}{{C_{vp}}^2}) + {\omega_{vp}}^4 = 0 \tag{3.23}$$

$$x_1 = \frac{2{\omega_{vp}}^2 + \frac{A^2}{{C_{vp}}^2} + \frac{A}{C_{vp}}\sqrt{8{\omega_{vp}}^2 + \frac{A^2}{{C_{vp}}^2}}}{2} \tag{3.24}$$

$$x_2 = \frac{2{\omega_{vp}}^2 + \frac{A^2}{{C_{vp}}^2} - \frac{A}{C_{vp}}\sqrt{8{\omega_{vp}}^2 + \frac{A^2}{{C_{vp}}^2}}}{2} \tag{3.25}$$

Thus, the four roots of the biquadratic equations are the following four frequencies:

$$\omega_1 = \sqrt{\frac{2{\omega_{vp}}^2 + \frac{A^2}{{C_{vp}}^2} + \frac{A}{C_{vp}}\sqrt{8{\omega_{vp}}^2 + \frac{A^2}{{C_{vp}}^2}}}{2}} \tag{3.26}$$

$$\omega_2 = -\sqrt{\frac{2{\omega_{vp}}^2 + \frac{A^2}{{C_{vp}}^2} + \frac{A}{C_{vp}}\sqrt{8{\omega_{vp}}^2 + \frac{A^2}{{C_{vp}}^2}}}{2}} \tag{3.27}$$

$$\omega_3 = \sqrt{\frac{2{\omega_{vp}}^2 + \frac{A^2}{{C_{vp}}^2} \quad \frac{A}{C_{vp}}\sqrt{8{\omega_{vp}}^2 + \frac{A^2}{{C_{vp}}^2}}}{2}} \tag{3.28}$$

$$\omega_4 = -- \quad \sqrt{\frac{2{\omega_{vp}}^2 + \frac{A^2}{{C_{vp}}^2} \quad \frac{A}{C_{vp}}\sqrt{8{\omega_{vp}}^2 + \frac{A^2}{{C_{vp}}^2}}}{2}} \tag{3.29}$$

By relating the known roots of (3.22) with the polynomial coefficients, the following equations result:

$$C_0 = \omega_1 \omega_2 \omega_3 \omega_4 = \omega_{vp}^4 \tag{3.30}$$

$$C_1 = \omega_1 + \omega_2 - \omega_3 - \omega_4 = 0 \tag{3.31}$$

$$C_2 = -\omega_1\omega_2 + \omega_1\omega_3 + \omega_1\omega_4 + \omega_2\omega_3 + \omega_2\omega_4 - \omega_3\omega_4 = 2\omega_{vp}{}^2 + \frac{A^2}{C_{vp}{}^2} \tag{3.32}$$

$$C_3 = \omega_1\omega_3\omega_4 + \omega_2\omega_3\omega_4 + \omega_1\omega_2\omega_3 + \omega_1\omega_2\omega_4 = 0 \tag{3.33}$$

From (3.32), we can find the value of C_{vp} as:

$$C_{vp} = \sqrt{\frac{A^2}{C_2 - 2\omega_{vp}{}^2}} \tag{3.34}$$

The value of ω_{vp} can be found as

$$\omega_0 = \omega_{vp} = \sqrt{\omega_1\omega_3} \tag{3.35}$$

The rest of the components of the unit cell can now be found as follows:

$$L_{vp} = \frac{1}{\omega_{vp}{}^2 C_{vp}} \tag{3.36}$$

$$L_{hs1} = \frac{1}{q_1{}^2 C_{vp}} \tag{3.37}$$

$$C_{hs1} = \frac{1}{\omega_{vp}{}^2 L_{hs1}} \tag{3.38}$$

$$L_{hs2} = \frac{1}{q_2{}^2 C_{vp}} \tag{3.39}$$

$$C_{hs2} = \frac{1}{\omega_{vp}{}^2 L_{hs2}}\,. \tag{3.40}$$

Thus, when given two frequency points at a desired phase along with the input and output terminal Bloch impedances, one can now obtain the asymmetric NRI-TL component values using the above equations.

To check the validity of the above, as an example, the following asymmetric NRI-TL was designed using the following design parameters:

f_1=1.5 GHz

f_2=- f_1

f_3=2.5 GHz

f_4=- f_3

q_1=50 Ohms

q_2=60 Ohms

Unt cell phase shift $\varphi=\beta d$=90^o

By using equations (3.30)-(3.40) the resulting unit cell component values are derived: L_{hs1}=10.27 nH, C_{hs1}=0.66 pF, L_{hs2}=14.79 nH, C_{hs2}=0.46 pF, C_{vp}=4.11 pF and L_{vp}=1.64 nH. The dispersion plot for this unit cell can be seen in Fig. 3-2 below:

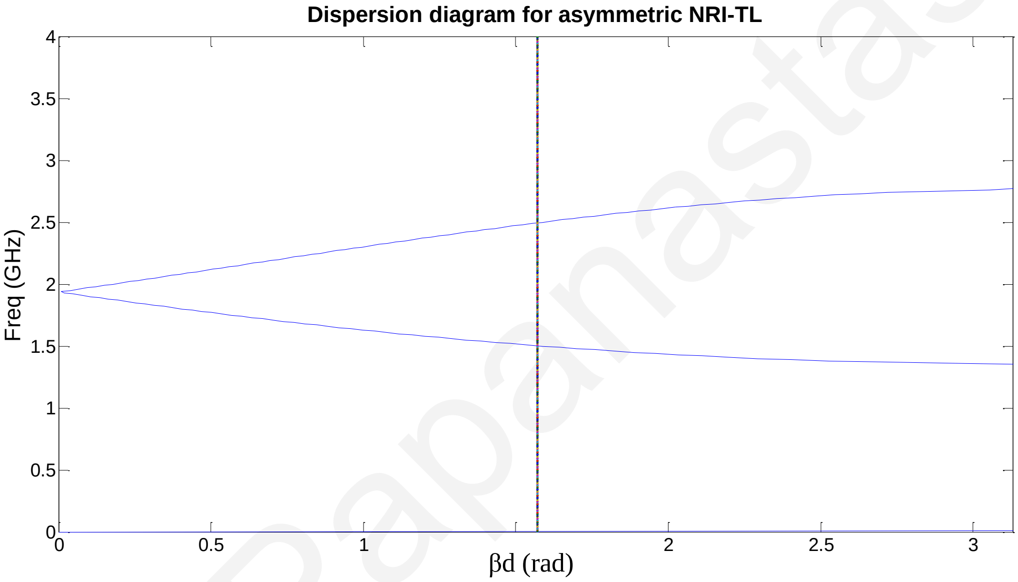

Fig. 3-2. Dispersion plot for asymmetric NRI-TL unit cell with q_1=50 and q_2=60 with 90 degree phase shift

In Fig. 3-2 the closed stopband condition still holds, which can be seen from the fact that there is no bandgap between the right and left handed regions of the dispersion diagram. The frequencies at which the dispersion diagram is 90 degrees is shown by the intersection of the vertical line with the dispersion plot. These frequencies are 1.5 GHz and 2.5 GHz, which are the desired design frequencies.

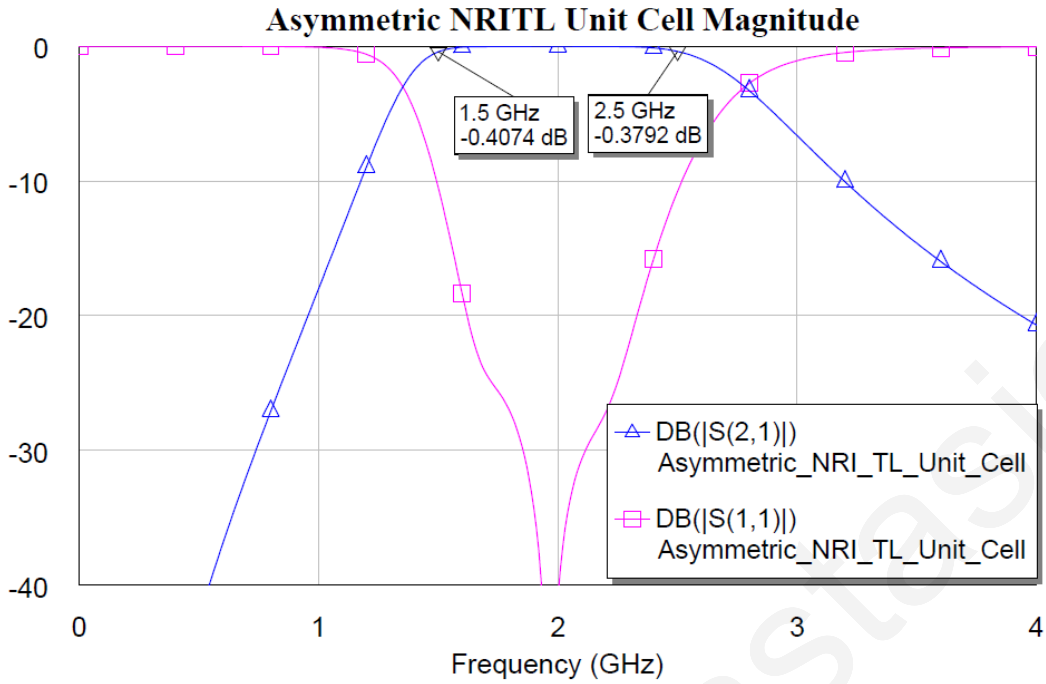

Fig. 3-3. Magnitude response of the asymmetric NRI-TL unit cell with q_1=50, q_2=60 and βd=90^o

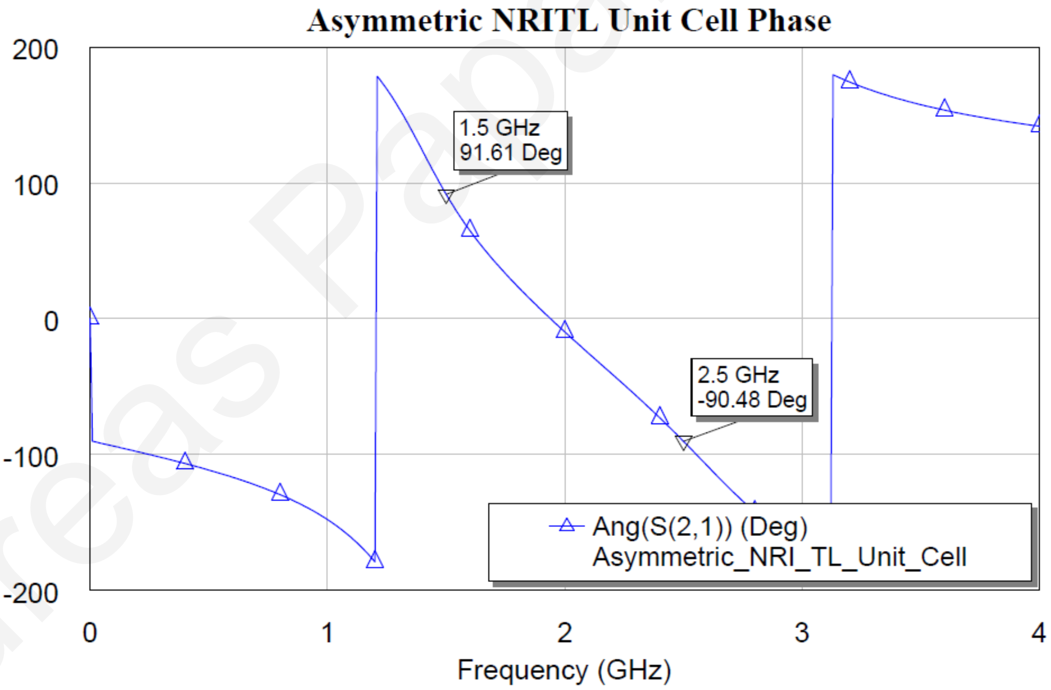

Fig. 3-4. Insertion phase response of the asymmetric NRI-TL unit cell with q_1=50, q_2=60 and βd=90^o

The unit cell has also been modeled in Microwave Office, yielding the plots of Fig. 3-3 and Fig. 3-4. In these plots the magnitude and phase response of this NRI-TL unit cell is shown. The bandpass nature of the structure is prominent. The return loss of the unit cell is degraded compared to a symmetric unit cell, because of the impedance mismatch created in a 50 ohm system. From the markers on the insertion phase plot, the phase shift at the two operating frequencies can be seen to be very close to 90 degrees.

The use of such an asymmetrical unit cell becomes more apparent when two such unit cells are placed in series to create a bandpass filter structure as shown in Fig. 3-5. With the dual-band NRI-TL unit cell, a single-band bandpass filter can be designed. The operating frequencies f_1 and f_2 will represent the band edges, as long as the phase shift at these frequencies is +/- π.

When cascading two unit cells, the second unit cell should be mirrored in order to get an overall symmetric structure, as shown in Fig. 3-5 below.

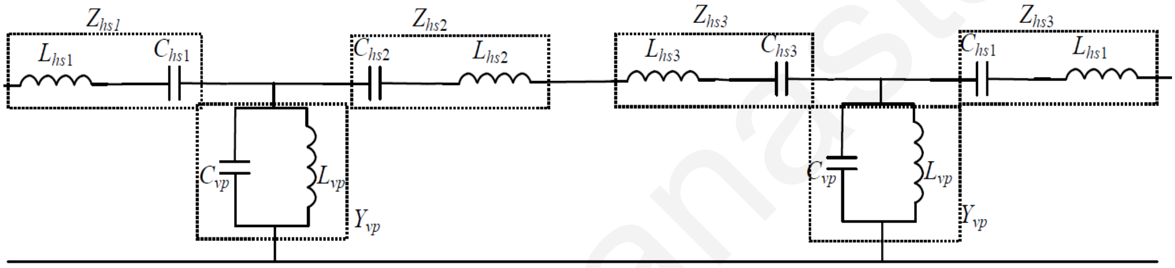

Fig. 3-5 A cascade of two unit asymmetric unit cells

The ABCD matrix of the two-cell structure of Fig. 3-5 can be obtained as follows:

$$\begin{bmatrix} A & B \\ C & D \end{bmatrix} = \begin{bmatrix} A1 & B1 \\ C1 & D1 \end{bmatrix} \begin{bmatrix} A2 & B2 \\ C2 & D2 \end{bmatrix} \tag{3.41}$$

$$\begin{bmatrix} A & B \\ C & D \end{bmatrix} = \begin{bmatrix} 1 + Z_{hs1}Y_{vp} & Z_{hs1} + Z_{hs2} + Z_{hs1}Z_{hs2}Y_{vp} \\ Y_{vp} & 1 + Z_{hs2}Y_{vp} \end{bmatrix} \begin{bmatrix} 1 + Z_{hs3}Y_{vp} & Z_{hs1} + Z_{hs3} + Z_{hs1}Z_{hs3}Y_{vp} \\ Y_{vp} & 1 + Z_{hs1}Y_{vp} \end{bmatrix} \tag{3.42}$$

$$A = (1 + Z_{hs1}Y_{vp})(1 + Z_{h3}Y_{vp}) + Y_{vp}(Z_{hs1} + Z_{hs2} + Z_{hs1}Z_{hs2}Y_{vp}) \tag{3.43}$$

$$B = (1 + Z_{hs1})(1 + 2Z_{hs1} + Z_{hs2} + Z_{hs3} + Z_{hs1}Z_{hs2}Y_{vp} + Z_{hs1}Z_{hs3}Y_{vp}) \tag{3.44}$$

$$C = Y_{vp}[(1 + Z_{hs1}Y_{vp}) + (1 + Z_{hs3}Y_{vp})] \tag{3.45}$$

$$D = (1 + Z_{hs1}Y_{vp})(1 + Z_{hs2}Y_{vp}) + Y_{vp}(Z_{hs1} + Z_{hs3} + Z_{hs1}Z_{hs3}Y_{vp}) \tag{3.46}$$

The Bloch propagation constant is then given by the well known formula:

$$\cos \beta d = \frac{A + D}{2}$$

This yields the following dispersion relation:

$$\cos\beta d = 1 + (Z_{hs1} + Z_{hs2} + Z_{hs3})Y_{vp} + Z_{hs1}Y_{vp}^2(Z_{hs2} + Z_{hs3}) \tag{3.47}$$

For simplicity and without loss of generality, Z_{hs2} can be set equal to Z_{hs3} and q_2=q_3 in order to get a symmetric fifth order bandpass filter.

Two unit cells have been simulated using the following design parameters:

f_1=1.5 GHz

f_2=2.5 GHz

q_1=63.9 Ohms

q_2=59.4 Ohms

q_3=59.4 Ohms

Unit cell phase shift $\varphi=\beta d=117^{o}$

Making use of equations (3.30)- (3.40), the component values derived are: L_{hs1}=10.27 nH, C_{hs1}=0.66 pF, L_{hs2}=14.79 nH, C_{hs2}=0.46 pF, L_{hs3}=14.79 nH, C_{hs3}=0.46 pF C_{vp}=4.11 pF and L_{vp}=1.64 nH. Furthermore, a comparison was made to the performance of a Chebyshev fifth order filter using the following parameters and the lowpass to bandpass frequency transformations from [69]:

Passband Ripple L_{Ar}=0.1 dB							
n=	g_0	g_1	g_2	g_3	g_4	g_5	g_6
5	1	1.1468	1.3712	1.9750	1.3712	1.1468	1

Table 2. Element Values for Chebyshev lowpass prototype filters (g_0=1, ω_c=1)

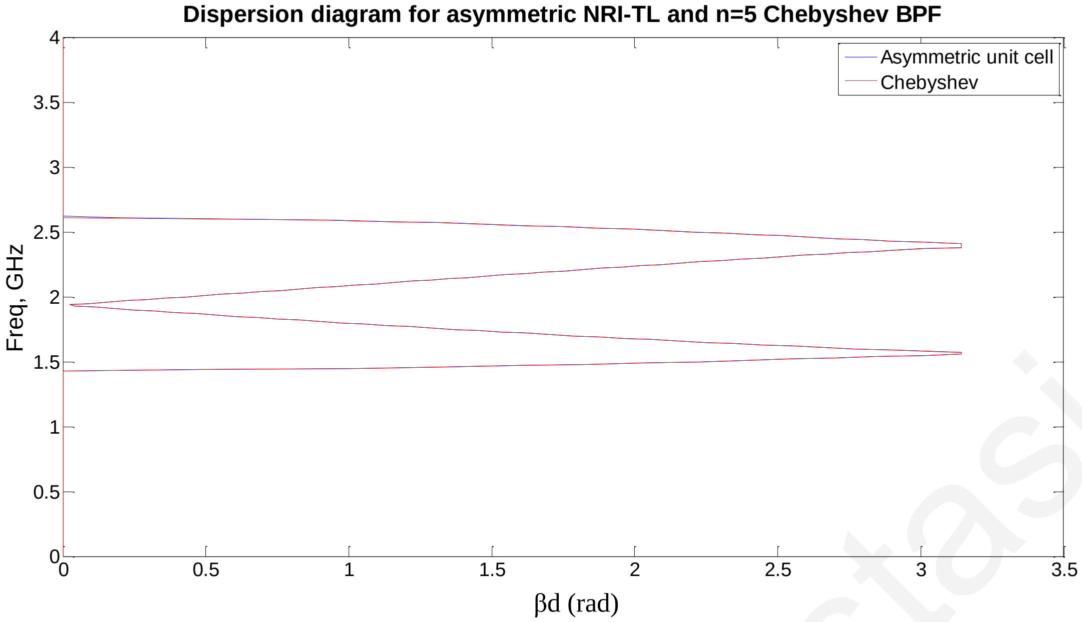

Fig. 3-6. Comparison of dispersion for NRI-TL unit cell structure of Fig. 3-5 and n=5 Chebyshev BPF

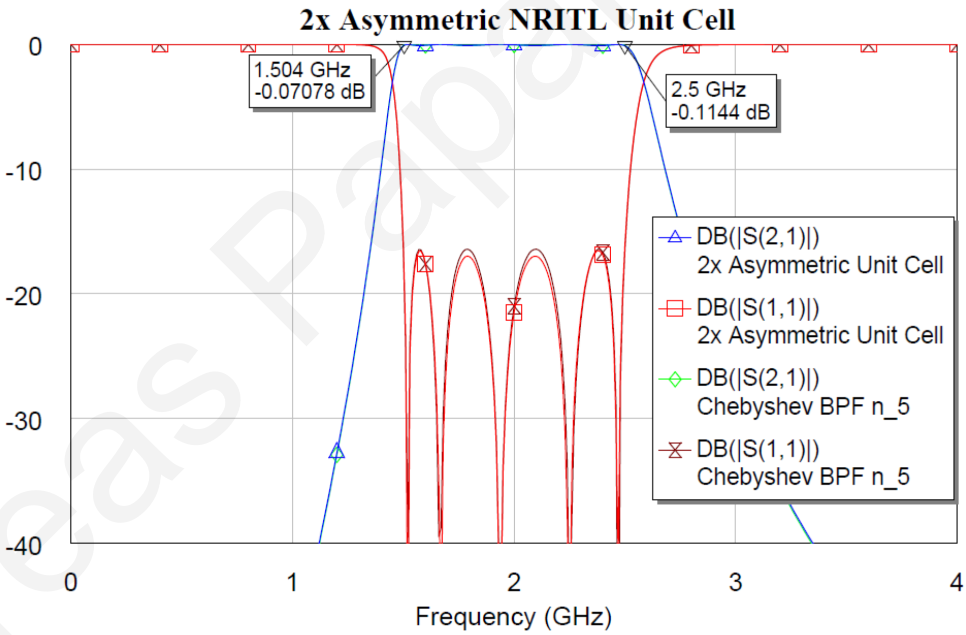

Fig. 3-7. Comparison of Magnitude response for NRI-TL unit cell structure of Fig. 3-5 and n=5 Chebyshev BPF

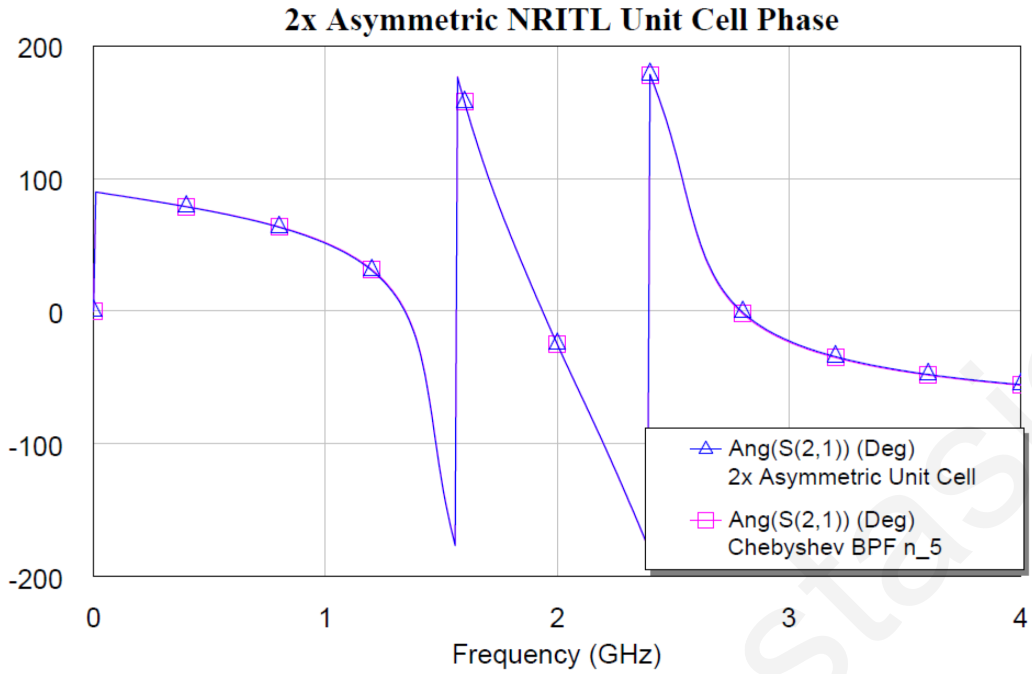

Fig. 3-8. Comparison of Insertion Phase response for NRI-TL unit cell structure of Fig. 3-5 and n=5 Chebyshev BPF

Fig. 3-6- Fig. 3-8 above indicate that using the NRI-TL method for synthesizing a bandpass filter yields exactly the same performance as a bandpass filter synthesized from classical filter theory.

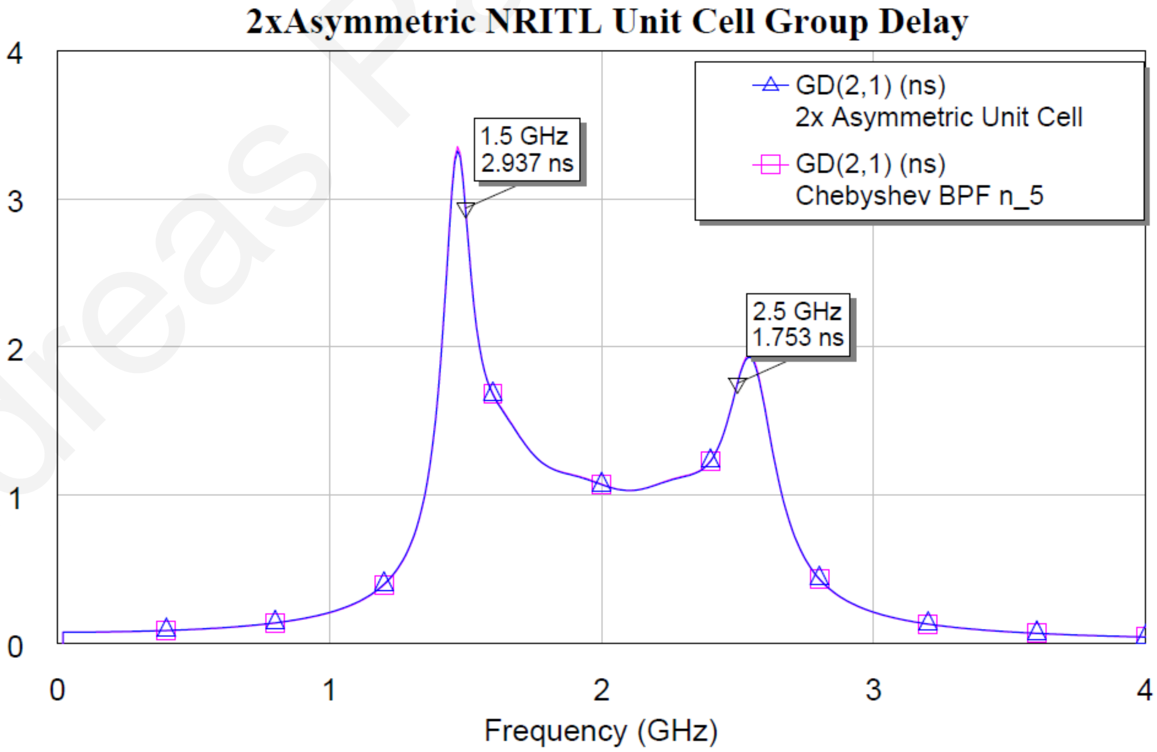

Fig. 3-9. Group delay comparison between the filter constructed with NRI-TL unit cells and the reference Chebyshev filter

A comparison of the group delay performance of the two designs in Fig. 3-9, shows that both designs share the same group delay characteristics. This also proves the applicability of the method in such designs, not as a replacement of classical filter theory, but as a versatile tool in designing practical filters comparable to the ones predicted by classical theory.

3.2 Dual-band filters using GNRI-TL unit cells

For applying the previous analysis for dual-band filters, and by using the exact same reasoning as for the above designs, one can move a step further and use the asymmetric Quad-Band GNRI-TL Unit Cell, as seen in Fig. 3-10.

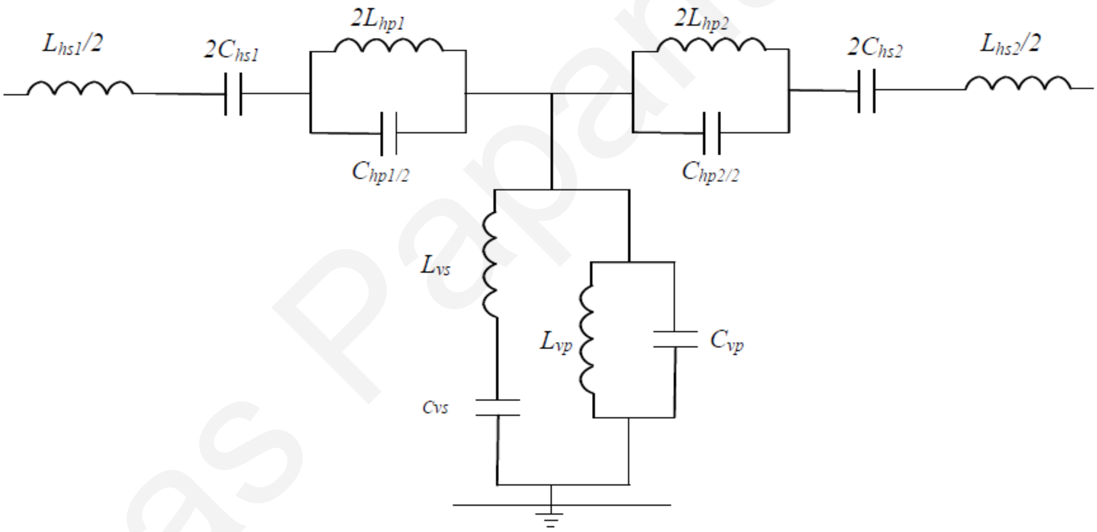

Fig. 3-10. Asymmetric GNRI-TL Unit Cell circuit

In contrast to the circuit of Fig. 2-7, this circuit has different impedances at the input and output series branches, which makes this unit cell asymmetric. The two impedances of the series branches can be written as:

$$Z_{h1} = j\omega L_{hs1}/2 + \frac{1}{j\omega 2C_{hs1}} + \frac{1}{j\omega C_{hp1}/2 + \frac{1}{j\omega 2L_{hp1}}} \tag{3.48}$$

$$Z_{h2} = j\omega L_{hs2}/2 + \frac{1}{j\omega 2C_{hs2}} + \frac{1}{j\omega C_{hp2}/2 + \frac{1}{j\omega 2L_{hp2}}} \tag{3.49}$$

The admittance of the vertical branch is the same as in (2.35):

$$Y_v = j\omega C_{vp} + \frac{1}{j\omega L_{vp}} + \frac{1}{j\omega L_{vs} + \frac{1}{j\omega C_{vs}}} \tag{3.50}$$

With the above equations, the ABCD matrix of the asymmetric GNRI-TL unit cell can be constructed and the dispersion relation expressed as:

$$\cos\beta d = A = (1 + Z_{hs1}Y_{vp})(1 + Z_{h3}Y_{vp}) + Y_{vp}(Z_{hs1} + Z_{hs2} + Z_{hs1}Z_{hs2}Y_{vp}) \tag{3.51}$$

The design equations for this unit cell then become:

$$q = \sqrt{q_1 q_2} \tag{3.52}$$

$$Y_{vp}^2 = -\frac{2(1-\cos\Phi)}{q^2} = -A \tag{3.53}$$

$$C_{vp} = \frac{A}{C_1} \tag{3.54}$$

$$\omega_{or}^2 = \frac{C_3}{C_1} \tag{3.55}$$

$$\omega_{vp}^2 = C_0 \frac{C_1}{C_3} \tag{3.56}$$

$$\omega_{vsvp}^2 = C_2 - \frac{C_3}{C_1} - C_0 \frac{C_1}{C_3} \tag{3.57}$$

$$L_{vp} = \frac{1}{\omega_{vp}^2 C_{vp}} \tag{3.58}$$

$$L_{vs} = \frac{1}{\omega_{vsvp}^2 C_{vp}} \tag{3.59}$$

$$C_{vs} = \frac{1}{\omega_{or}^2 L_{vs}} \tag{3.60}$$

$$L_{hs1} = q_1 C_{vp} \tag{3.61}$$

$$C_{hs1} = \frac{1}{\omega_{vp}^2 L_{hs1}} \tag{3.62}$$

$$L_{hs2} = q_2 C_{vp} \tag{3.63}$$

$$C_{hs2} = \frac{1}{\omega_{vp}^2 L_{hs2}} \tag{3.64}$$

$$C_{hp1} = \frac{4 L_{vs} C_{vp}}{L_{hs1}} \tag{3.65}$$

$$L_{hp1} = \frac{1}{\omega_{or}^2 C_{hp1}} \tag{3.66}$$

$$C_{hp2} = \frac{4 L_{vs} C_{vp}}{L_{hs2}} \tag{3.67}$$

$$L_{hp2} = \frac{1}{\omega_{or}^2 C_{hp2}} . \tag{3.68}$$

It is noted here that equations (3.54)- (3.60) are identical to the ones in (2.63)- (2.69) and are repeated here for completeness. Equations (3.48), (3.61)-(3.68) are the ones that are needed to make the unit cell operate as an asymmetric GNRI-TL circuit.

Using the following parameters, f_1=1.5 GHz, f_2=2.5 GHz, f_3=4 GHz, and f_4=5 GHz, q_1=50 Ohms and q_2=45 Ohms, equation (3.51) yields the dispersion plot of Fig. 3-11. When using this type of unit cells, a dual-band bandpass filter can be designed, with the f_1, f_2, f_3 and f_4 frequencies representing the 3 dB band edges, as long as the designed phase shift at these frequencies is chosen to be +/-π.

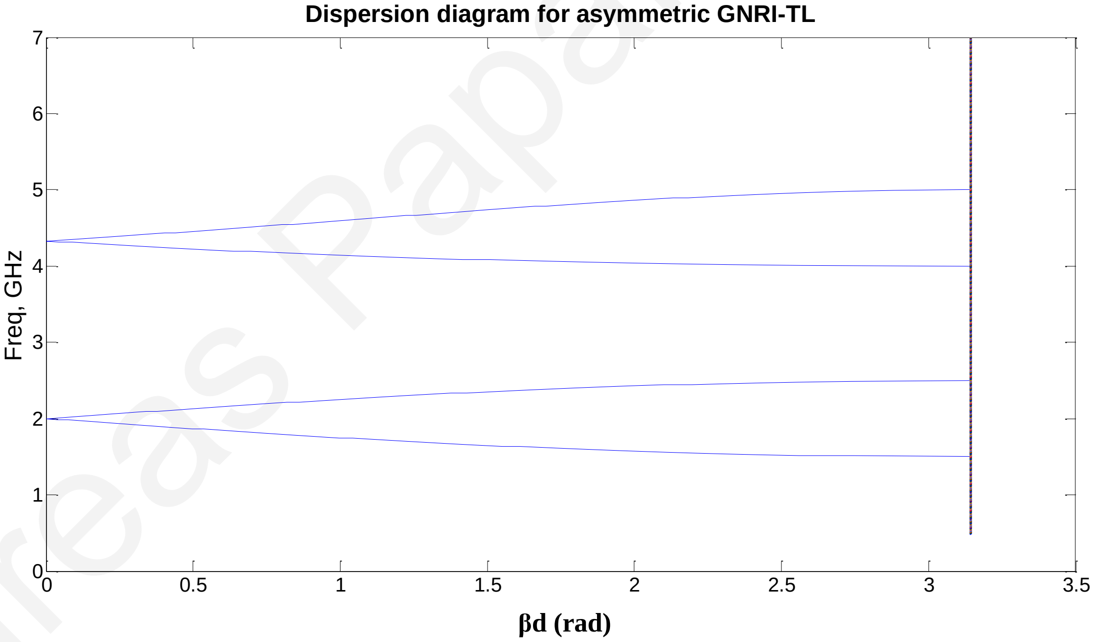

Fig. 3-11. Dispersion plot for the asymmetric GNRI-TL unit cell

From Fig. 3-11, one can observe that the intersection of the dispersion plot with the $x=\pi$ line happens at the four design frequencies as well as the absence of any stopband, which proves the validity of the equations developed. In Fig. 3-12, the magnitude response is shown. The two passbands are very prominent and the 3 dB cutoff points coincide with the design frequencies as well.

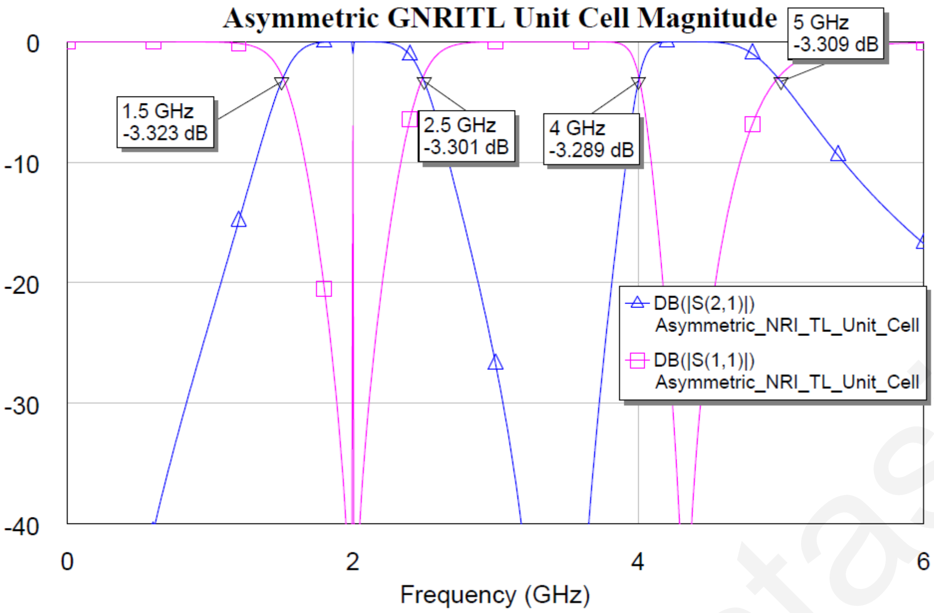

Fig. 3-12. Magnitude response of the example asymmetric GNRI-TL unit cell

From the above results, it is clear that the GNRI-TL unit cell theory can also be used as a straightforward method of designing any type of single and dual-band passive filters. For quad-band filters, a slightly different methodology has to be used. In this case, the four frequencies of operation have to be selected at the center of the desired bands of operation, and a different phase shift (e.g. 90 degrees) has to be used at each frequency, if for example one wants to design a shorted λ/4 bandpass filter. Such a design has been done in this work and is explained in the following sections.

3.3 Expanded GNRI-TL Theory

Any practical unit cells such as the ones discussed above, must unavoidably have transmission line sections to host the lumped element components that make up the unit cell. The effect of these transmission lines is a shift of the target frequencies at a desired phase shift. Thus a new model must be considered, where these effects are calculated and taken into account when designing such unit cells.

One way to calculate these effects is by following the same reasoning as above, but the unit cell model must also include the transmission lines. Fig. 3-13 shows how this is done.

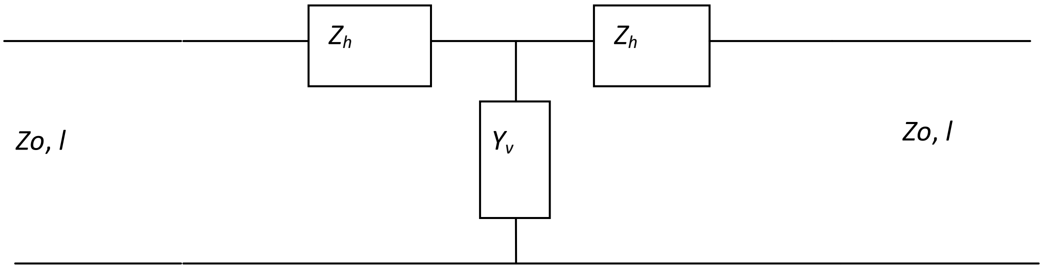

Fig. 3-13. Unit Cell two-port with host TL

The ABCD Matrix of the above 2-port circuit is given by the relation:

$$\begin{bmatrix} A & B \\ C & D \end{bmatrix} = \begin{bmatrix} cos\beta l & jZ_0 sin\beta l \\ jY_0 sin\beta l & cos\beta l \end{bmatrix} \begin{bmatrix} 1+Z_hY_v & Z_h(2+Z_hY_v) \\ Y_v & 1+Z_hY_v \end{bmatrix} \begin{bmatrix} cos\beta l & jZ_0 sin\beta l \\ jY_0 sin\beta l & cos\beta l \end{bmatrix} \qquad (3.69)$$

After evaluating the above matrix multiplication, the following ABCD parameters result:

$$A = (1+Z_hY_v)\cos^2\beta l + jZ_0Y_v[Z_h(1+Z_hY_v)+Z_h] \qquad (3.70)$$
$$\sin\beta l\cos\beta l + jY_0\sin\beta l\cos\beta l - Y_0Z_0(1+Z_hY_v)\sin^2\beta l = D$$

where *l* is the length of the host transmission line and βl represents the phase shift incurred by the transmission line.

Thus, the new dispersion relation, becomes:

$$\cos\beta d = (1+Z_hY_v)(\cos^2\beta l - \sin^2\beta l) + j\{Y_o[Z_h(1+Z_hY_v)+Z_h]\} \qquad (3.71)$$

The imaginary term of the above equation must be zero, which results in the following:

$$\cos\beta d = (1+Z_hY_v)(2\cos^2\beta l - 1) \qquad (3.72)$$

As an example, consider the case where a phase shift $\Phi=\beta d= 45^o$ is required at the frequencies f_1=1 GHz, f_2=2 GHz, f_3=4 GHz and f_4=5 GHz. The host transmission line used in this example, has a phase shift of 0.25 radians (around 15 degrees) at the center frequency of 3 GHz, which represents the typical phase shift of a 3mm length of transmission line which would be used for this type of unit cell. Plotting the above two dispersion relations with respect to frequency, results in the following graph of Fig. 3-14.

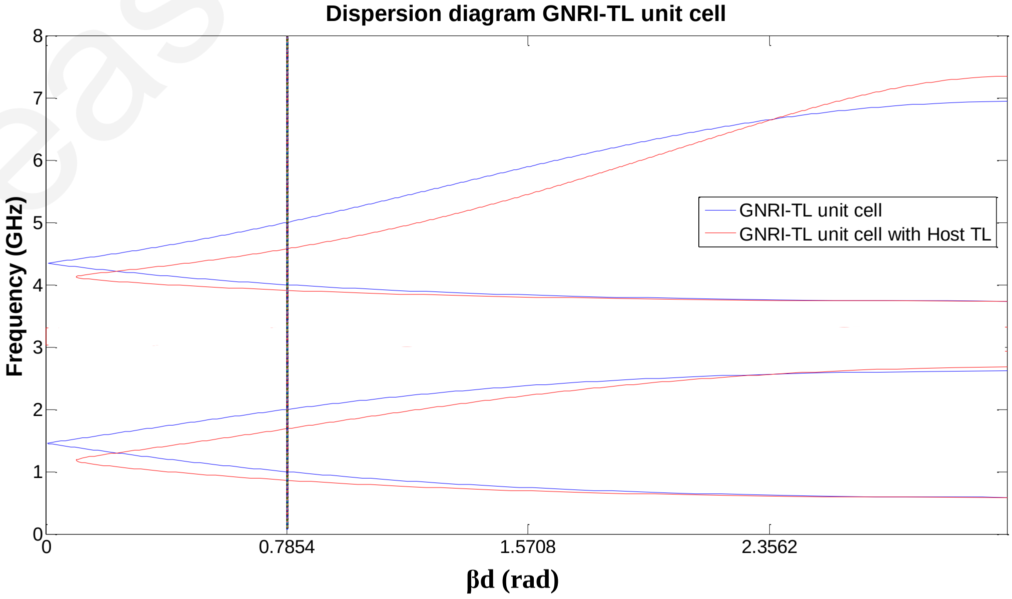

Fig. 3-14. Plot of the dispersion relations, with and without the host TL

The blue line represents the generalized NRI-TL dispersion and the red line represents the generalized NRI-TL dispersion with the host TL. The black vertical line is located at *βd*=45 degrees. The four points where the *βd*=45 degree line cuts the blue dispersion line, are the four design frequencies. It can be seen that this *βd*=45 degree line intersects the red dispersion line not at the design frequencies, but at frequencies that are offset by a certain amount. This is the error that should be rectified. To do this, the series inductance and the shunt capacitance of the host TL should be calculated and subtracted from the Generalized NRI-TL values of L_{hs} and C_{vp} respectively. Then a recalculation of all the other component values must be done, and the unit cell performance recalculated. Fig 3-15 below shows the correction that occurs and is represented by the green curve which now coincides with the blue curve of the original, theoretical unit cell at the four design frequencies and at the desired phase shift of 45 degrees.

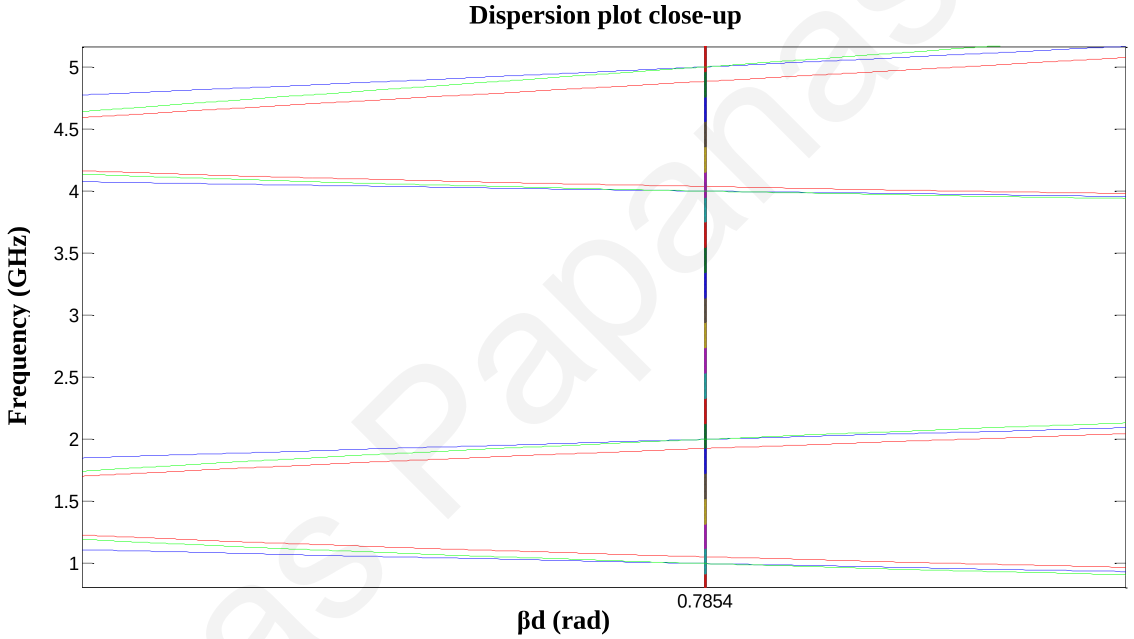

Fig. 3-15. Close-up of the corrected dispersion curve (in green)

The above expansion to the GNRI-TL theory, as first presented in [17], results in the correction of the frequency offsets caused by the existence of the host TLs. Using this correction model, a Quad-Band Wilkinson Divider [18] was designed and fabricated, and is subsequently presented in this work.

3.4 Summary

In this Chapter, a new NRI-TL unit cell was presented, that featured different input and output impedances. The new dispersion relation for this unit cell was derived along with the new relationship between the impedance and admittance of the horizontal and vertical branches of the unit cell respectively. The unit cell's component values were obtained from new equations that kept the closed stopband condition. An example unit cell was designed and subsequently a back-to-back configuration of two asymmetrical unit cells was simulated in a configuration of a typical 5-pole bandpass filter. The simulated results were compared to the simulated results of a standard 5-pole Chebyshev filter using classical filter theory. The two sets of results were shown to be nearly identical, which proved the applicability of such an asymmetrical unit cell in single-band bandpass filter applications.

Also in this Chapter, new equations yielding the component values of an asymmetrical GNRI-TL unit cell were presented. These equations were derived using the same methodology as for the NRI-TL unit cell and an example was shown on how a dual-band asymmetrical GNRI-TL bandpass filter can be constructed.

Chapter 3 also expanded on the existing GNRI-TL theory by means of adding into the GNRI-TL unit cell model, the host transmission lines using the line impedance and phase shift method and presenting the new dispersion relation that accounts for these host transmission lines.

Chapter 4

4 Device Implementations

Using the expanded GNRI-TL theory developed above, a variety of microwave devices can be designed. The following sections describe the design methodology and fabrication of such devices. Specifically, a quad-band Wilkinson power divider and a quad-band rat-race coupler are designed and implemented with simulated and measured results presented and compared. Also, a shorted $\lambda/4$ 3-pole bandpass filter is designed and simulated results are presented.

4.1 Quad-Band Wilkinson Divider using GNRI-TL unit cells

The classical equal split Wilkinson divider consists of two branches with characteristic impedance $\sqrt{2}Z_0$ and electrical length equal to $\lambda/4$. These two branches are connected by a shunt resistor $R = 2Z_0$. At the design frequency, the port return losses and the output port isolations are best [18]. Another characteristic of the Wilkinson divider is that the insertion phase at the design frequency is -90 degrees.

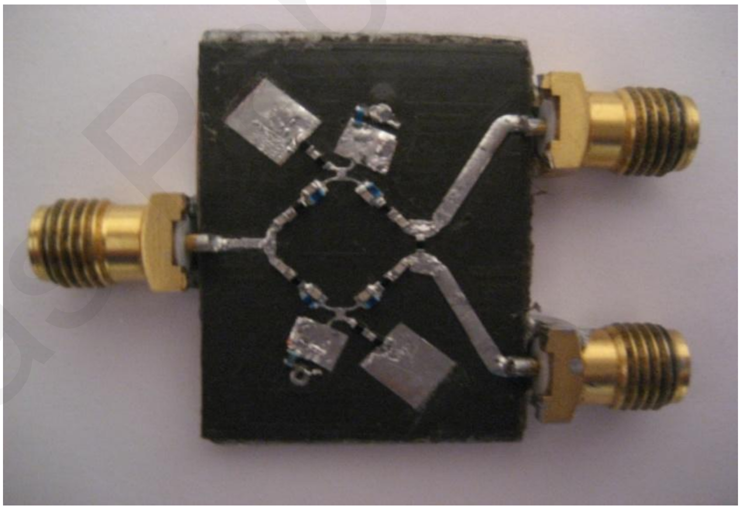

Fig. 4-1 Photograph of the fabricated quad-band generalized NRI-TL Wilkinson power divider in microstrip technology.

In the case of the proposed Wilkinson power divider there are two generalized NRI-TL unit cells in place of the $\lambda/4$ Wilkinson transmission-line branches. Fig. 4-2 shows the schematic diagram of the unit cell used for this purpose. The dispersion relation for this unit cell is given by:

$$\cos \beta d = (1+Z_B Y_B)(\cos^2 \beta l - Z_o Y_o \sin^2 \beta l) - j \sin \beta l \cos \beta l \left[Z_o Y_B + 2Y_o Z_B (1+Z_B Y_B) \right.$$

as shown in equation (3.71).

The dispersion diagram for this unit cell is shown in Fig. 4-3 where βd on the graph is the desired phase shift per unit cell. From the dispersion diagram in Fig. 4-3 it is clear that four alternating left-handed and right-handed bands are created, and for a given transmission phase there are four distinct frequencies corresponding to it. The goal here was to design the unit cell for a set of given frequencies and a corresponding insertion phase of $\beta d=\pi/4$.

The unit cell presented here consists of four distinct resonators, designed to operate at $\omega_{or} = 2\pi \times 2$ GHz. The choice of ω_{or} is done such that it is located roughly in the center of the four given design frequencies, which in this case are 850 MHz, 1.30 GHz, 2.65 GHz and 3.70 GHz. Each unit cell was designed to operate under the closed stopband condition as described in [17] and [26] where the horizontal and vertical branch zero frequencies of the unit cell are equal and are given by:

$$\omega_{hz1,2} = 0.5(2\omega_{or}^2 + \omega_{hshp}^2) \pm 0.5\sqrt{(2\omega_{or}^2 + \omega_{hshp}^2) - 4\omega_{or}^4} \tag{4.1}$$

$$\omega_{vz1,2} = 0.5(2\omega_{or}^2 + \omega_{vsvp}^2) \pm 0.5\sqrt{(2\omega_{or}^2 + \omega_{vsvp}^2) - 4\omega_{or}^4} \tag{4.2}$$

$$\omega_{hshp}^2 = 1/(L_{hs}C_{hp}) \tag{4.3}$$

$$\omega_{vsvp}^2 = 1/(L_{vs}C_{vp}) \tag{4.4}$$

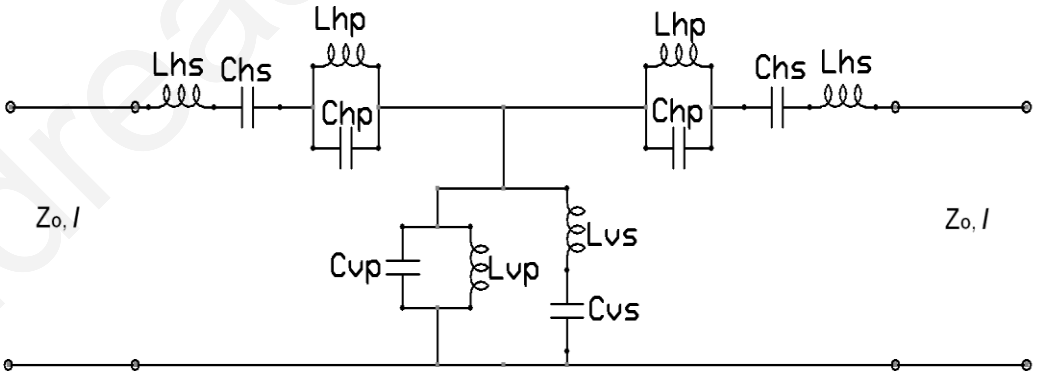

Fig. 4-2 Unit cell of the proposed generalized NRI-TL medium

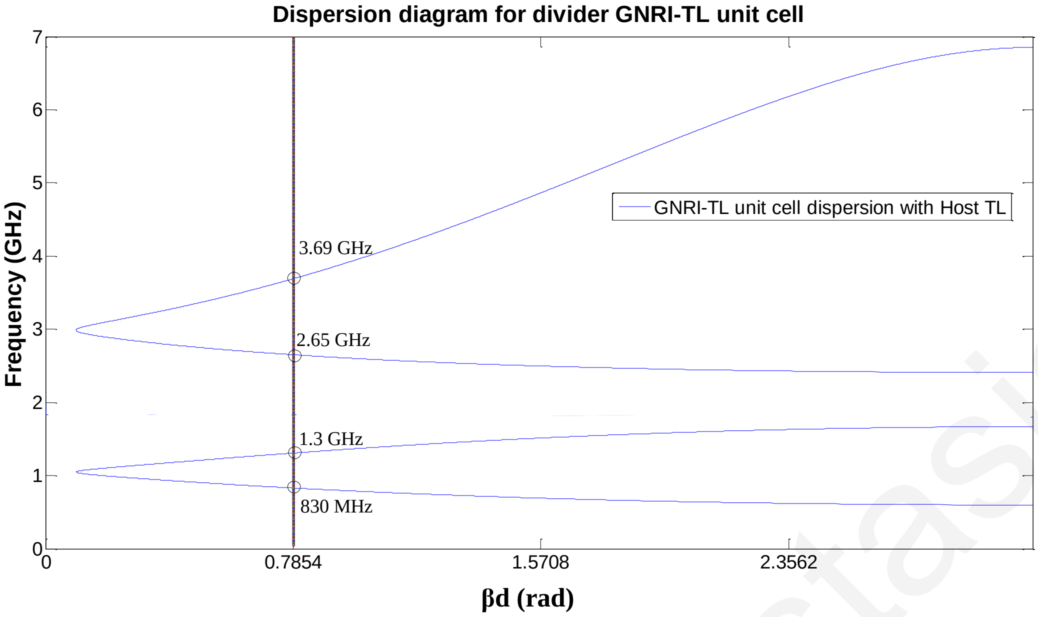

Fig. 4-3 Dispersion diagram of the generalized NRI-TL unit cell

It is obvious that for the closed stopband condition to hold, $\omega_{hshp} = \omega_{vsvp}$. For the design of the unit cell the zero transmission phase frequencies f_{hz1} and f_{hz2} must be placed around the center of the two lower (1.075 GHz) and higher (3.175 GHz) design frequencies respectively.

Once f_{hz1} and f_{hz2} have been found, the component values and frequency tuning can be calculated using Eq. 8 from [14]. The resulting component values are L_{hs} = 4.3 nH, L_{hp} = 4.9 nH, L_{vp} =7.36 nH, L_{vs} = 6.46 nH, C_{hs} = 1.47 pF, C_{hp} = 1.29 pF, C_{vp} = 0.86pF and C_{vs} = 0.98 pF.

The dispersion diagram shows that there are four distinct frequencies with the same insertion phase of 90 degrees at 830MHz, 1.31 GHz, 2.65 GHz and 3.69 GHz and the points of minimum insertion phase (βd=0.097) are located at 1.048 GHz and 2.988 GHz which are close to the theoretical design frequencies of the unit cells. This confirms the quad-band operation of each cell. In addition, each unit cell has been designed to have a characteristic impedance of 70.7 Ohms and the length of the unit cells is designed to be close to λ/4. Furthermore, a 100 Ohm resistor connects the output side of each branch, as in the case of the classical Wilkinson divider.

4.1.1 Physical realization

The specific topology of the proposed Wilkinson divider in microstrip is shown in Fig. 4-4. In the physical implementation of each unit cell, the four resonators making up each unit cell consist of both distributed and chip element capacitors and inductors. The chip capacitors have values of C_{hs} =1.6 pF and C_{hp} =1.2 pF, whereas the chip inductors used are L_{hs}=3.3 nH, L_{hp} =4.7 nH, L_{vs1} 1=3.3 nH and L_{vs2}=1.5 nH (in series) and

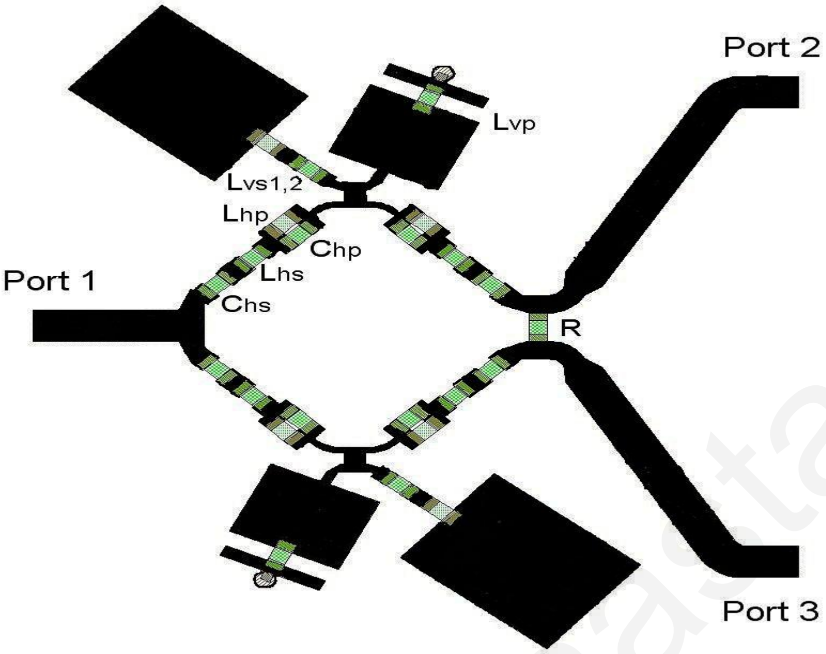

Fig. 4-4 NRI-TL Wilkinson divider topology in microstrip

L_{vp} =7.5 nH. The device is built using microstrip technology on a 0.381mm thick RT/5880 Duroid substrate with ε_r= 2.2, soldered on a 1 mm thick copper plate to provide for proper grounding and mechanical strength. The total size of the device excluding the SMA connectors is 27x22 mm.

The performance of the divider was first simulated using the commercially available Microwave Office circuit simulator package. The testing of the fabricated divider was performed using an Agilent E8363B Vector Network Analyzer. Fig. 4-5 shows the simulated S_{21} against the measured S_{21} of the divider. In this figure, the two major passbands are visible and a small frequency offset from the center frequency of 2 GHz can be observed in the measured data which is caused by component tolerances and a slightly undercut layout. This offset is of the order of 6.4 % at 2.13 GHz. The insertion loss is less than 5 dB from 700 MHz to 1.48 GHz in the first passband and from 2.7 GHz to 4.3 GHz. The power division is less than 1.3 dB flat across the passbands. Also, the experimental results have a maximum degradation from the simulated results of less than 1 dB across most of the bandwidth.

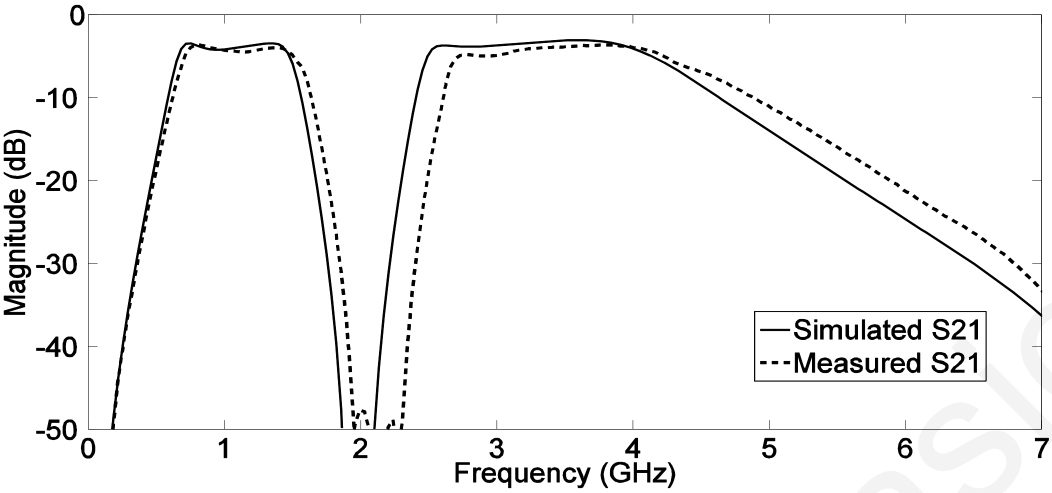

Fig. 4-5 Measured and simulated divider magnitude response S_{21}.

Furthermore, the insertion loss for the measured S_{31} tracks that of S_{21}. Another interesting feature of the divider is seen in the above figure as well. The deep rejection band at around the center frequency measures more than 47 dB of insertion loss between 1.9 GHz and 2.3 GHz. This feature can be particularly useful for isolation and noise rejection.

In Fig. 4-6 a comparison between the simulated and measured S_{11} can be seen.

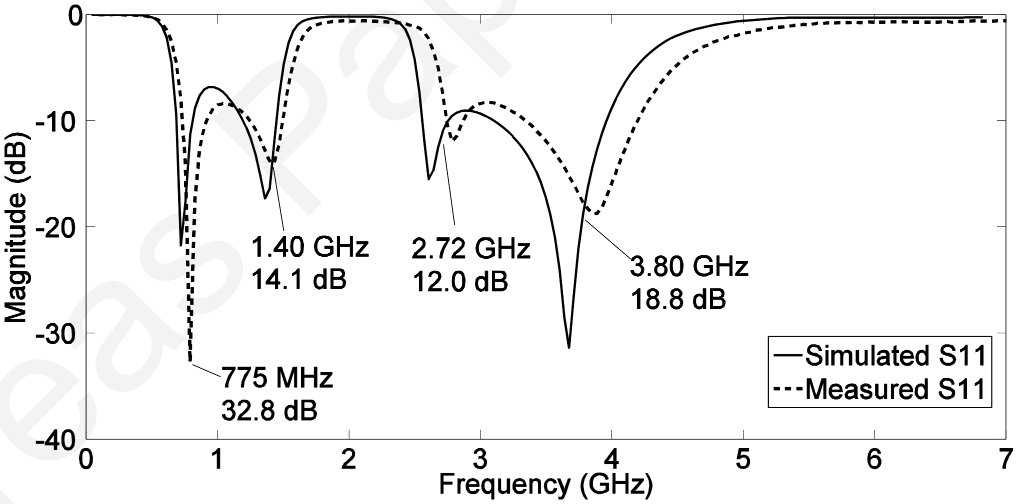

Fig. 4-6 Measured and simulated divider S_{11}.

From this figure, four prominent "dips" can be seen indicating that all four ports are matched around the design frequencies. It also verifies the quad band nature of the divider. The maximum frequency deviation of the measured results from the dispersion frequencies is 6.9 % at 1.4 GHz whereas the maximum deviation from the original design frequencies is 8.8 % at 775 MHz.

The output port return loss S_{22} is shown in Fig. 4-7 for the simulated and the fabricated divider. The quad band operation is verified from this plot as well. Once again the output ports are well matched around the design frequencies. A slight frequency offset is also observed between S_{11} and S_{22} which is caused by a slight imbalance between the output ports. However, taking the four frequencies shown in Fig. 4-6 as reference, the worst return loss of Fig. 4-7 is 21.8 dB at 1.40 GHz.

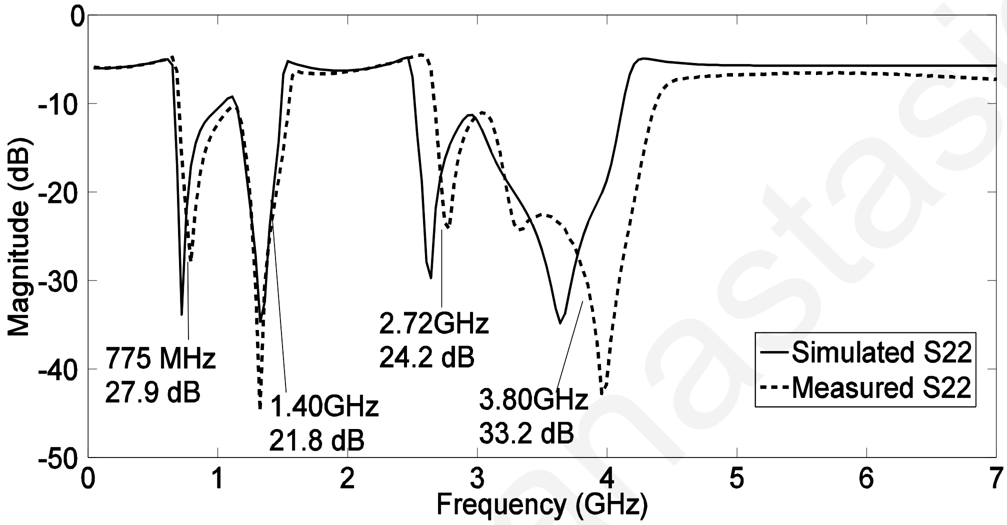

Fig. 4-7 Measured and simulated divider output return loss S22

The same pattern can be observed in Fig. 4-8 which shows the simulated against the measured isolation S_{23}. The divider's output ports can be seen to be well isolated near the four design frequencies.

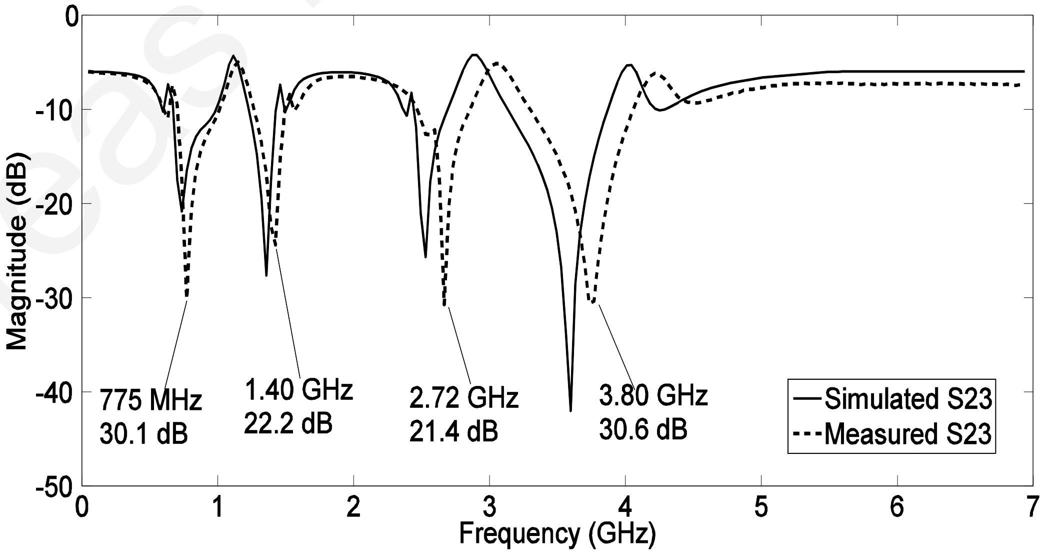

Fig. 4-8 Measured and simulated divider output port isolation.

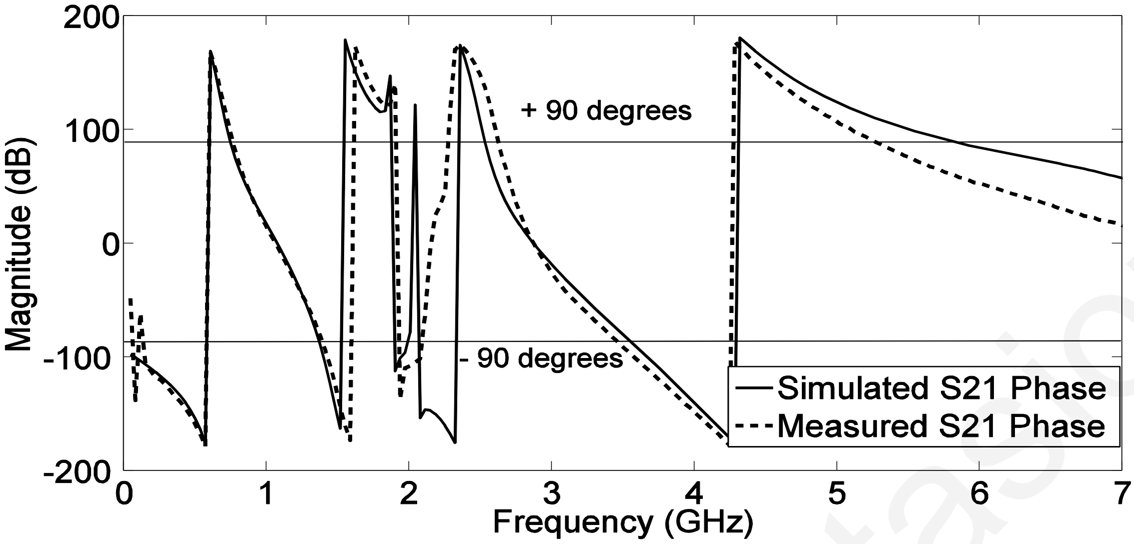

Fig. 4-9 . Measured and simulated divider insertion phase S21

Fig. 4-9 shows the measured and simulated insertion phase plots of the divider, which track each other closely. What is clear from Fig. 4-9 is that there are four distinct frequencies that exhibit insertion phase of either positive or negative 90 degrees. The points where the +90 and -90 degree lines intersect the graph can be seen to be very close to the design frequencies. For the measured data, these frequencies are at 760 MHz, 1.40 GHz, 2.64 GHz and 3.47 GHz.

From the above results, the quad-band GNRI-TL divider can be seen to clearly exhibit all the typical characteristics of a conventional singe-band design. The insertion loss degradation of nearly 2 dB from the ideal 3dB split, can be attributed to the individual lumped element component losses which originate mainly through the series resistance of the inductors.

4.2 A Quad-Band Rat-race Coupler using GNRI-TL unit cells

In the conventional design of the rat-race coupler, three sections of $\lambda/4$ and a $3\lambda/4$ transmission line (TL) section are used. For the design of this metamaterial coupler, a single GNRI-TL unit cell type has been used for simplicity of construction, each incurring a $\pm 90^0$ phase shift at the four design frequencies.

The four selected design frequencies chosen are f_1=900 MHz, f_2=1.55 GHz, f_3=2.017 GHz and f_4=2.55 GHz which correspond to the GSM 900, L1 GPS, UMTS and wifi frequencies respectively. The schematic for the unit cell is shown in Fig. 4-10, which is based on the GNRI-TL unit cell of [26]. The host TLs of length *l* and characteristic impedance Z_0 have also been included in this schematic which are unavoidable in any realizable circuit. Consequently, the effects of the host TL have to be included in the design of the unit cell. In general, the total of the TLs series distributed inductance has to be subtracted from the value of L_{hs}, and the TLs distributed shunt capacitance has to be subtracted from the value of the C_{vp}. For the calculation of the TL's inductance and capacitance, (4.5)- (4.8) have been used from [34]:

$$L_{TL} = 2x10^{-4} l \left[\ln\left(\frac{l}{W+t} \right) + 1.193 + 0.2235 \left(\frac{W+t}{l} \right) \right] K_g \quad (4.5)$$

$$K_g = 0.57 - 0.145 \ln\left(\frac{W}{h} \right) \quad (4.6)$$

$$Z_0 = 120\pi / \sqrt{\varepsilon_e} [W/h + 1.393 + 0.667 \ln(W/h + 1.444)] \quad (4.7)$$

$$C_{TL} = L_{TL} / Z_0^2 \quad (4.8)$$

In the above equations, *l, W, t, h,* Z_0 and ε_e are the microstrip length, width, thickness, substrate height, characteristic impedance and effective dielectric constant respectively. In order to obtain the smallest physically realizable unit cell, the TL portions that will host the lumped elements, have to be only big enough to accommodate the part. Using large TL sections to completely eliminate L_{hs} and C_{vp} is not the optimum method when designing for size minimization. A new value $L_{hs\_corrected} = L_{hs} - L_{TL}$ and $C_{vp\_corrected} = C_{vp} - C_{TL}$, can now be defined. Using the design equations from [26], (4.5)- (4.8), and the new component values $L_{hs\_corrected}$ and $C_{vp\_corrected}$ results in the following component values, which are summarized in Table 3 below.

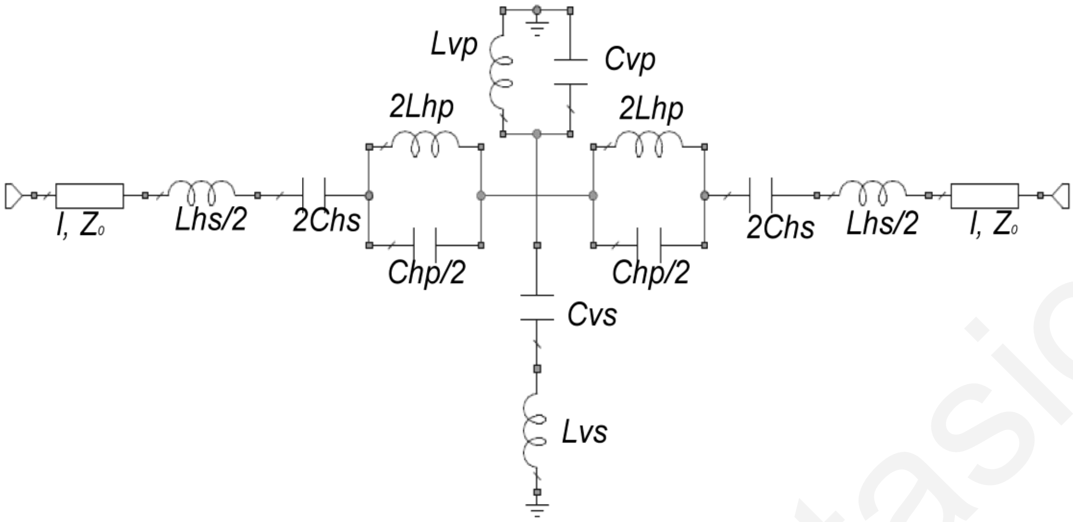

Fig. 4-10. GNRI-TL Unit Cell schematic with host TL included.

For the fabrication of the unit cell, the Rogers RO4003B was chosen with ε_r = 3.55 and 0.812 mm thickness and 18 μm copper. The use of metal- insulator- metal (MIM) capacitors instead of chip capacitors also leads to space savings. MIM capacitors also have the additional advantage of being very accurate in their values and have the highest series resonant frequencies. On the other hand, they add to the series inductance of the final circuit due to the ribbon required to connect them to the traces. This can be seen from the actual value of the $L_{hs\_corrected}$ in the table below. Fig. 4-11 shows the model of the unit cell, where the MIM capacitors, and chip inductors can be identified, yielding a very compact structure. Fig. 4-12 shows a photograph of the fabricated unit cell.

Component	Component Values	
	Designed Value	Actual Value
$L_{hs\_corrected}/2$	7.14 nH	6.8 nH
$2C_{hs}$	1.30 pF	1.2 pF
$2L_{hp}$	1.86 nH	2.7 nH
$C_{hp}/2$	3.96 pF	2.7 pF
L_{vs}	19.88 nH	20 nH
C_{vs}	0.37 pF	0.2 pF
L_{vp}	6.49 nH	7.5 nH
$C_{vp\_corrected}$	1.35 pF	1.0 pF

Table 3 GNRI-TL Unit Cell component values

4.2.1 Physical realization and performance of the GNRI-TL Rat-Race Coupler

The construction of the quad-band GNRI-TL rat-race coupler, requires six of the *λ*/4 unit cells, three of which are in series giving the required 270^0 phase shift of the 3*λ*/4 segment of the coupler.

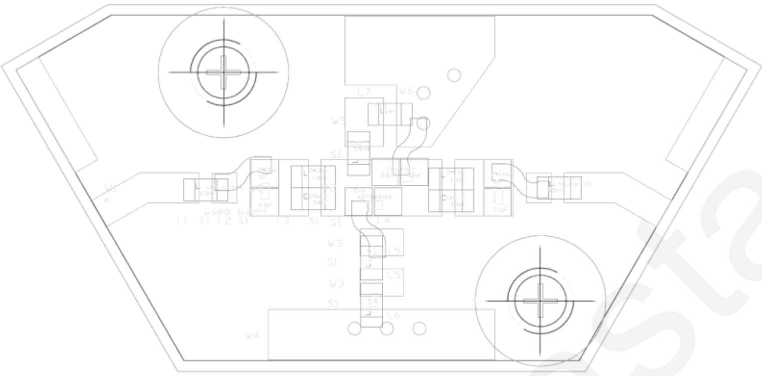

Fig. 4-11. AutoCAD model of the GNRI-TL unit cell. The maximum dimensions of the unit cell are x=17.5 mm and y=8.5mm.

Fig. 4-12. Photograph of the fabricated GNRI-TL unit cell

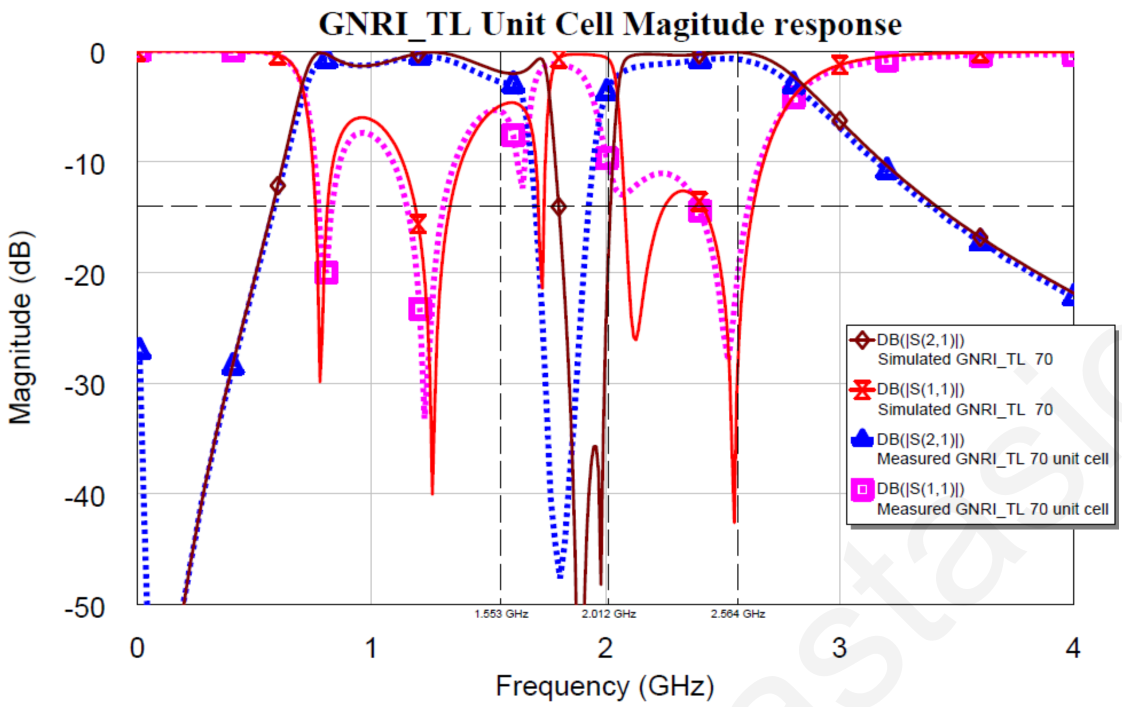

Fig. 4-13. Measured and simulated S- parameters of the GNRI-TL unit cell.

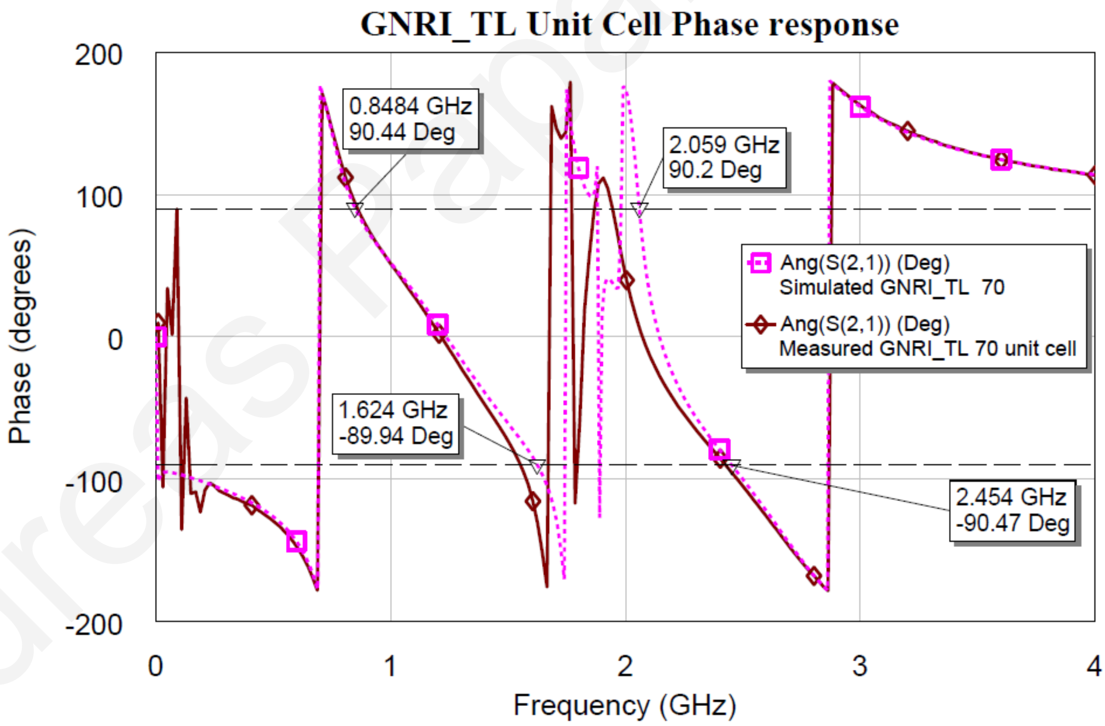

Fig. 4-14. Measured and simulated insertion phase of the GNRI-TL unit cell.

The unit cell was first designed using the corrections predicted by the theory detailed in the previous paragraphs. This design resulted in component values which were used in the circuit simulator and the full wave simulator to estimate performance. The unit cells were then fabricated using standard etching and soldering techniques. Fig. 4-13 and Fig. 4-14, show the simulated and measured magnitude and phase response of the GNRI-TL unit cell with the corrected component values. The four operating frequencies can be identified from the phase response. Good agreement between simulated and measured results can be seen. The discrepancies and slight frequency shifts can be attributed to component standard value tolerances.

The results taken from the measured GNR-TL unit cell were placed in the circuit simulator in the rat-race topology shown in Fig. 4-15. For comparison, the ideal GNRI-TL rat-race (without the host TLs), was constructed in the circuit simulator and its magnitude response is shown in Fig. 4-16. The four operating frequencies are clearly identified by the insertion loss (around 3dB) and the good return loss. The simulated response of the coupler using the measured unit cell is shown in Fig. 4-17. The four frequencies with the minimum insertion loss are the operating bands of the coupler. $|S_{21}|$ at f_1 is 3.3 dB. At f_2 $|S_{21}|$ is 3.8 dB, whereas the maximum insertion loss occurs at the third band, and is around 6.4 dB. This is caused by the proximity of this band to the strong rejection of the center band of the coupler. At f_4, the insertion loss is again around 3.3 dB. The next step was to construct six unit cells and connect them according to the arrangement of Fig. 4-15. A photograph of the fabricated rat-race coupler is shown in Fig. 4-18. The measured results of the fabricated coupler are shown in Fig. 4-16, Fig. 4-17 and Fig. 4-19. In Fig. 4-17 and Fig. 4-19, fabricated coupler results are compared to the simulated response of the coupler using the single measured unit cell. The purpose of making this comparison is to see the difference when non-identical cells are used for the coupler, which is always the case when building practical circuits, due to component variations between cells and workmanship variations in the hand-soldering process. From the results, two major conclusions can be drawn. The first one is that the insertion loss is higher in the case of the fabricated coupler, especially at f_3, with measured $|S_{21}|$ at -9.0 dB. The second conclusion is the downward frequency shift that occurs at all four operating frequencies. Both of these discrepancies compared to the simulation can be attributed to the interconnection of the six unit cells with ribbon, not included in the simulation and in effect, adding to the series inductance and the shunt capacitance that have to be subtracted from L_{hs} and C_{vp} respectively. Indeed, between each two unit cells a length of about 0.5 mm and 0.38 mm wide ribbon was used for their interconnection, resulting in an additional 0.3 nH per interconnection, or 1.8 nH overall. Modeling the ribbon in the simulator results in the downward frequency shift as well as the insertion loss of f_3 degrading to around -9.0 dB.

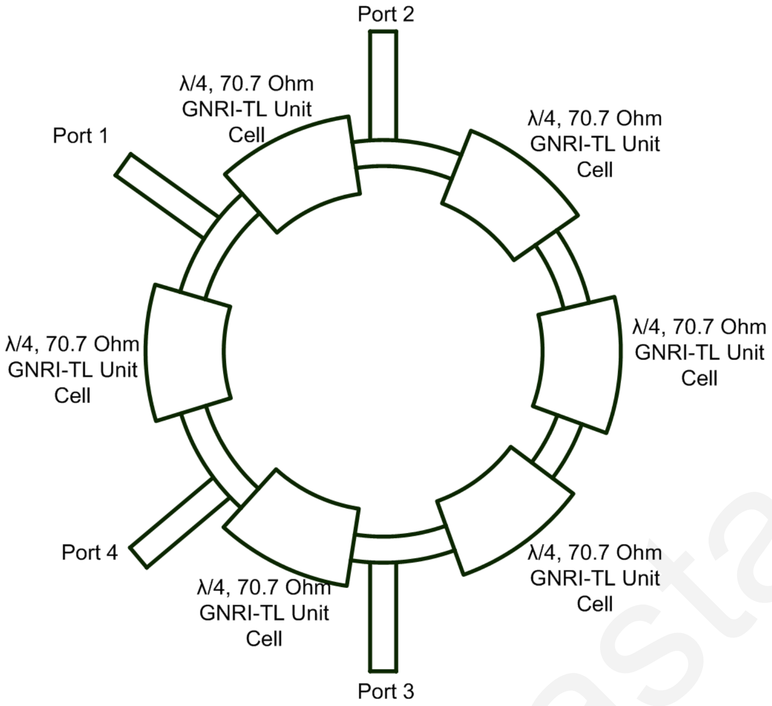

Fig. 4-15. Arrangement of the unit cells into a rat-race coupler

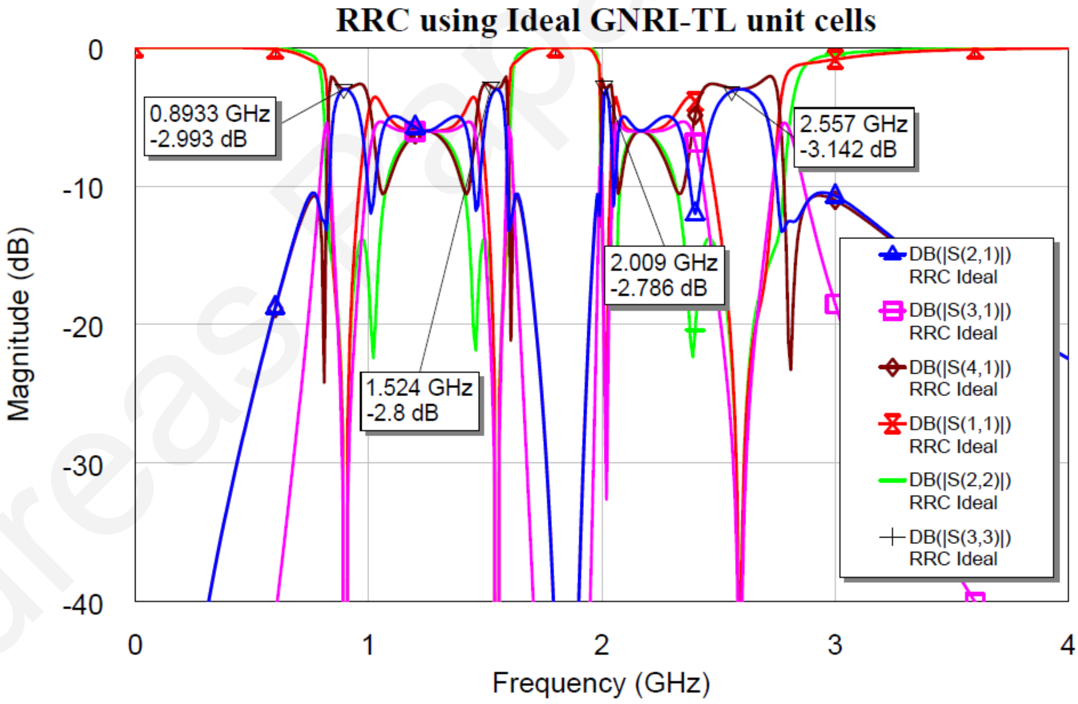

Fig. 4-16. Magnitude response of the ideal GNRI-TL rat race coupler, without the host TL effect.

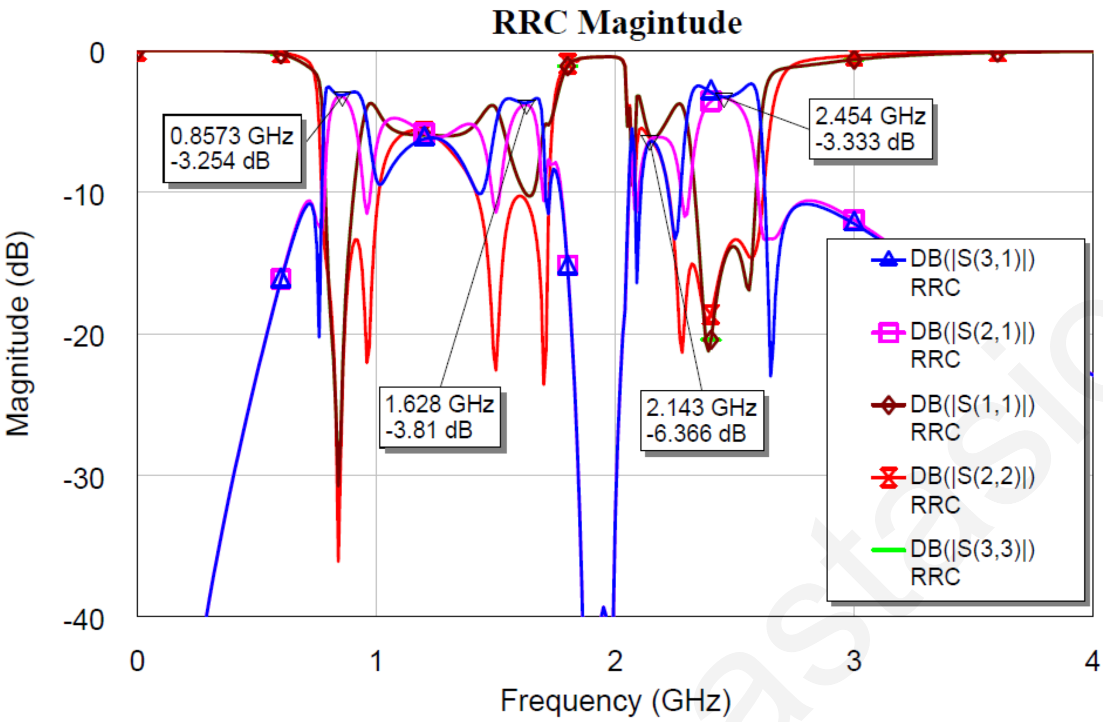

Fig. 4-17. Magnitude response of the quad-band rat-race coupler using the response of the measured GNRI-TL unit cell.

The diameter of the designed quad-band rat-race coupler is around 35 mm. In comparison, a conventional rat-race operating at 900 MHz, would have had a diameter of around 100 mm, on the same type of substrate. This shows that the metamaterial rat-race coupler also offers a 65% size reduction, compared to its conventional counterpart.

Fig. 4-18. Photograph of the fabricated GNRI-TL rat-race coupler

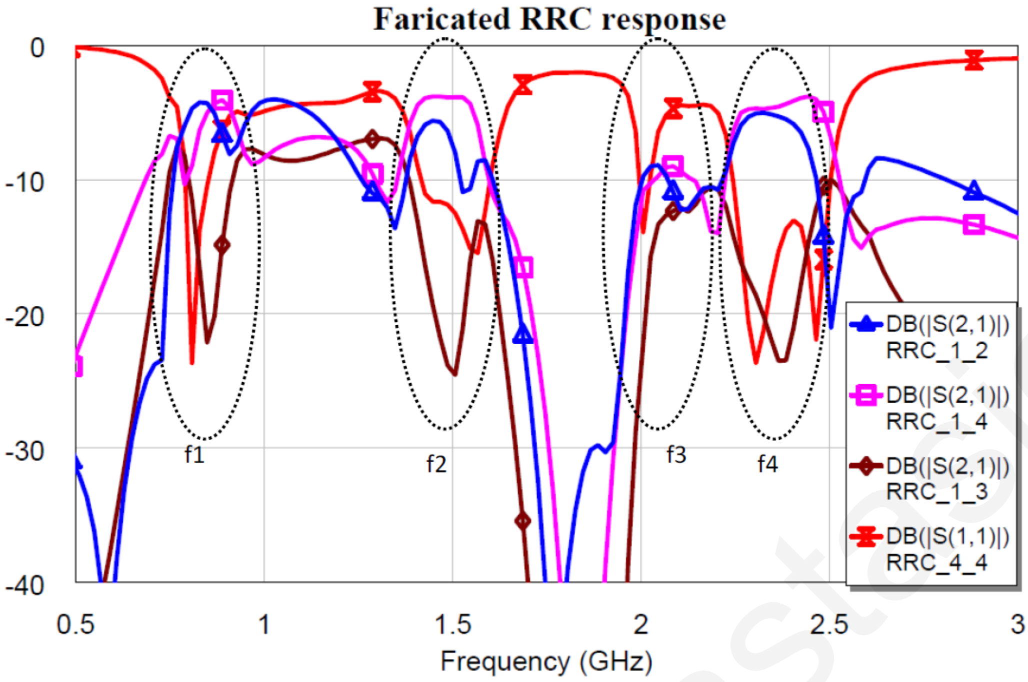

Fig. 4-19. Measured magnitude response of the fabricated rat-race coupler.

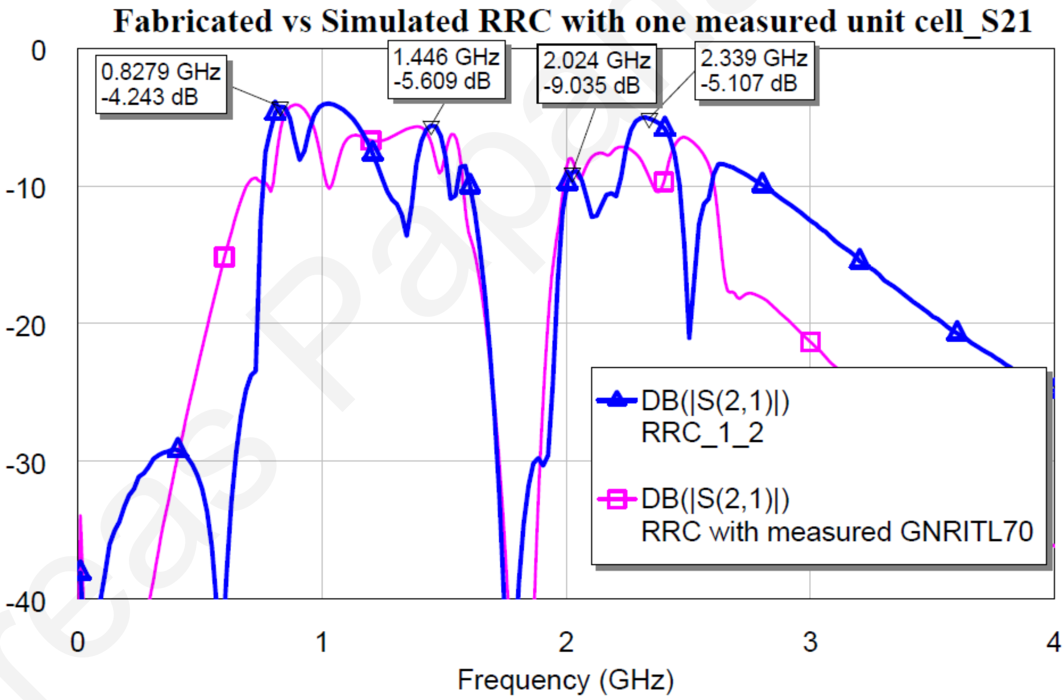

Fig. 4-20. │S_{21}│comparison of the fabricated vs. simulated rat-race coupler using one measured unit cell.

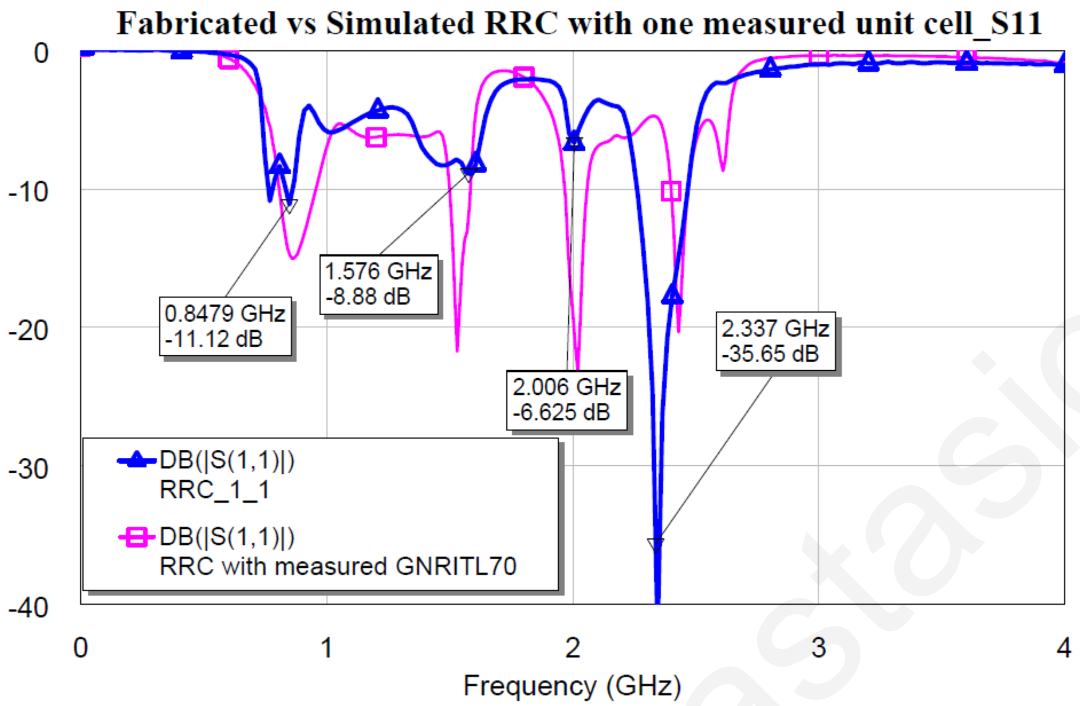

Fig. 4-21. │S_{11}│ comparison of the fabricated vs simulated rat-race coupler using one measured unit cell.

From the above results, the quad-band rat-race coupler can be seen to clearly exhibit all the typical characteristics of a conventional singe-band design. The insertion loss degradation of 1.2 dB from the ideal 3dB split for the 900 MHz operation up to 6 dB for the 2.017 GHz operation, can firstly be explained by the individual lumped element component losses which originate mainly through the series resistance of the inductors, and secondly by the lumped element tolerances, which create mismatches between the individual unit cells magnitude and phase performance. The design offers however a significant size reduction compared to a conventional single-band rat-race coupler.

4.3 A Narrow-Band Quad-Band Bandpass Filter Using Generalized GNRI-TL Unit Cells

The design of a Quad-Band Bandpass filter using quad-band GNRI-TL Unit Cells is presented in this section. The results shown here are theoretical results using the Microwave Office circuit simulator. The filter type chosen was a shorted λ/4, 3-pole Chebyshev bandpass filter.

Initially, a conventional shorted $\lambda/4$ 3-pole Chebyshev BPF was designed in Microwave Office. The circuit diagram and layouts are shown in Fig. 4-22 and Fig. 4-23.

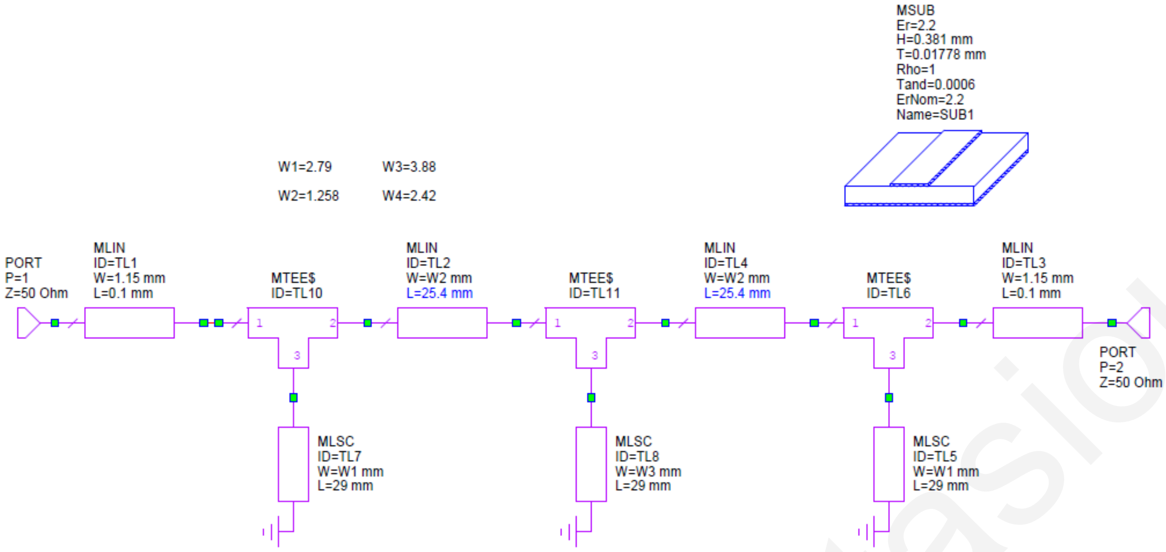

Fig. 4-22. Conventional 3-pole shorted λ/4 3-pole Chebyshev BPF

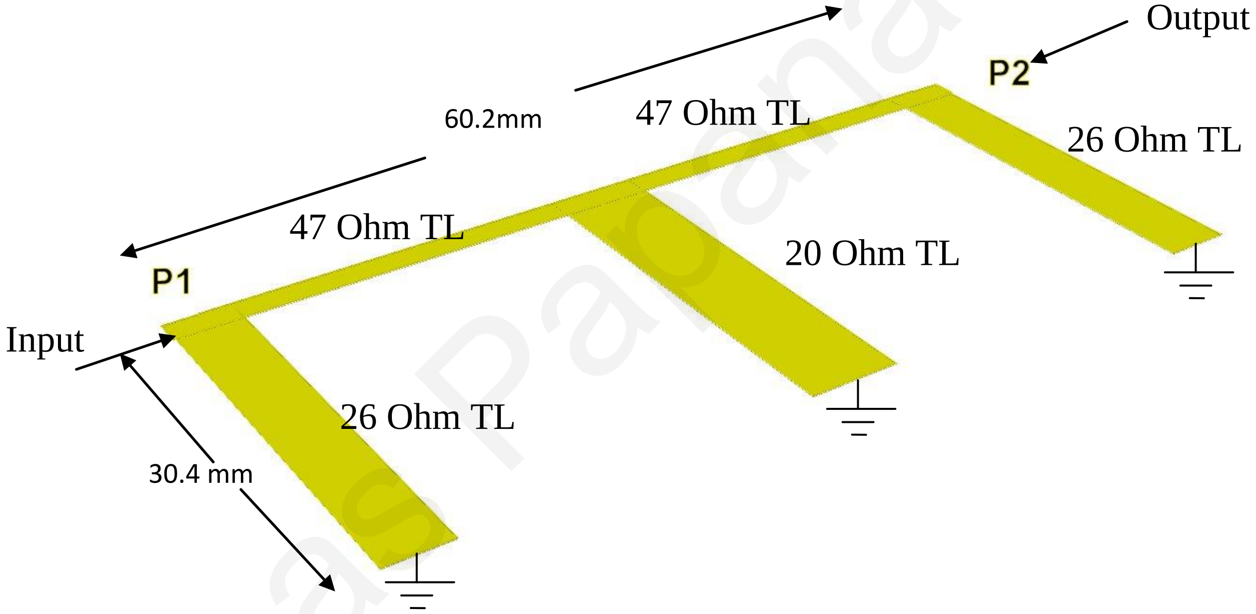

Fig. 4-23. Conventional 3-pole shorted λ/4 Chebyshev filter Layout (1.85 GHz operation)

Using the impedances of the transmission line sections, quad-band GNRI-TL unit cells were designed. Specifically, three different unit cells where designed. Their characteristic impedances were 20, 26 and 47 Ohms respectively. All three types of unit cells were designed to have a +/- 90 degree phase shift at the same four frequencies and the overall center frequency was *f*=3.089 GHz, such that at least three out of the four frequency bands was near common commercial communication frequencies. These four frequencies were *f*1=1.85GHz, *f*2=2.5GHz, *f*3=3.75GHz and *f*4=5GHz. Fig. 4-24 shows the typical schematic of the 20 Ohm unit cell.

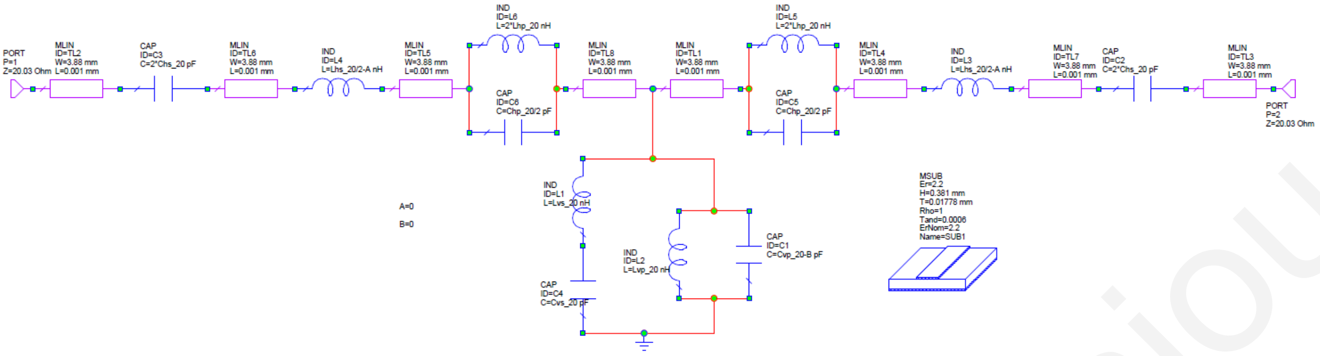

Fig. 4-24. 20 Ohm unit cell schematic

It is noted here that the capacitors and inductors are ideal, but the series connecting transmission lines are included in the model. Corrections in the series inductances and shunt capacitances are also included, to offset the effect of these TLs. Once the unit cells were designed, they were placed in an arrangement shown in Fig. 4-25.

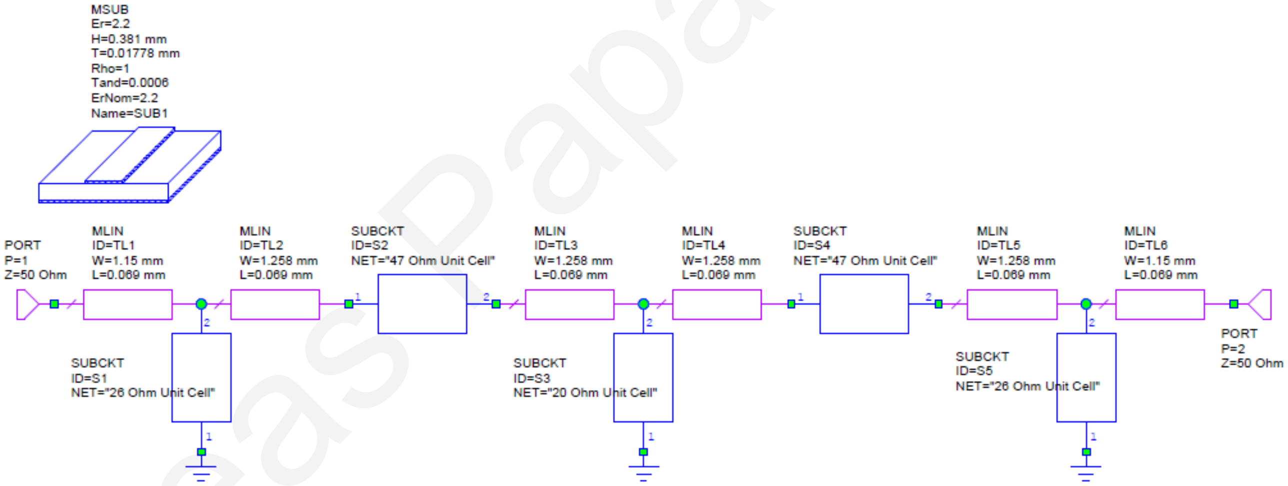

Fig. 4-25. 3-pole Chebyshev BPF using Quad-Band NRI-TL sections in place of standard $\lambda/4$ shorted sections

The simulated magnitude response of the above filter is shown in Fig. 4-26. The 3-dB frequencies are shown with markers.

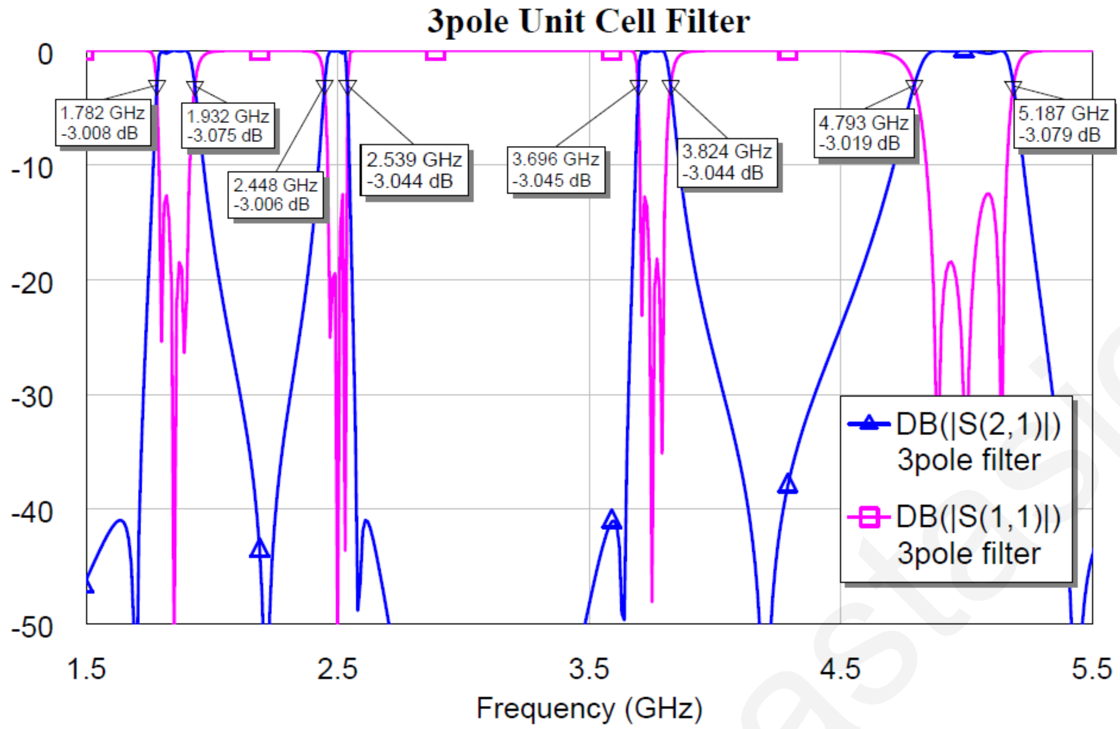

Fig. 4-26. Quad-Band shorted λ/4 GNRI-TL BPF magnitude response

The Quad-Band operation of the filter can be seen to be very prominent, with the 3dB points shown by the markers. In Fig. 4-27, the phase and unwrapped phase response is shown, with the passband centers also indicated by markers.

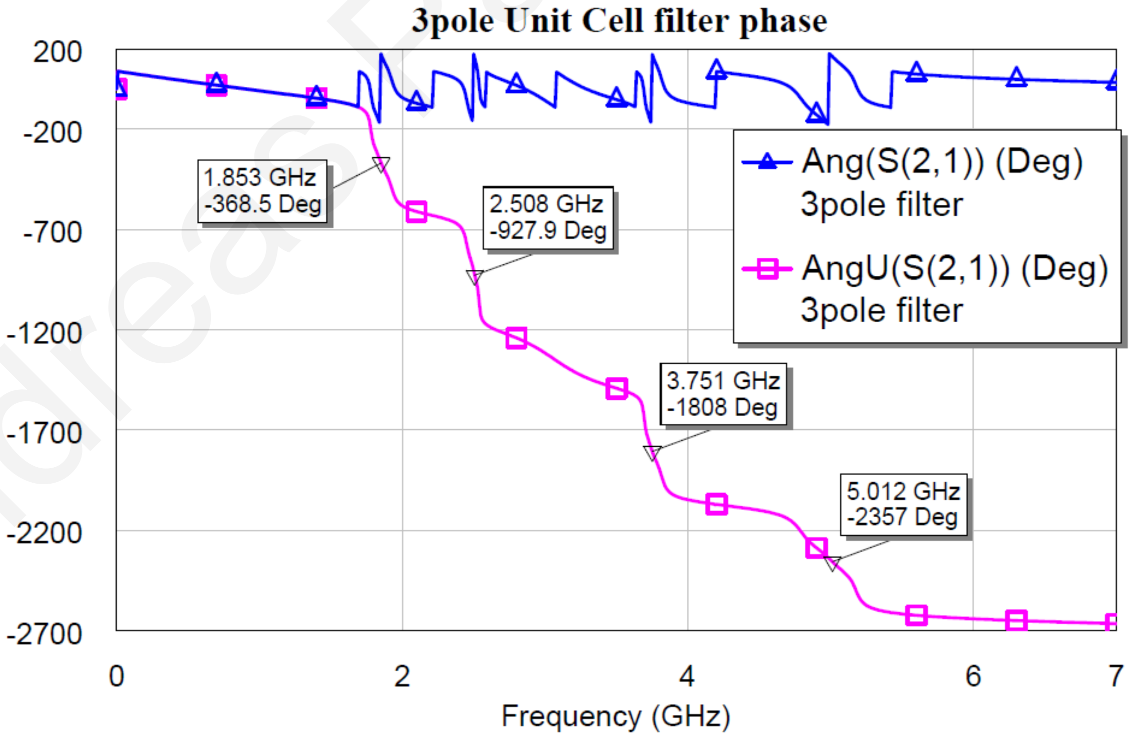

Fig. 4-27. Quad-Band BPF phase response

Again, the quad-band operation can be seen from the four nearly linear sections of the unwrapped phase, indicated by the markers.

Whereas the above result shows that in principle such a filter is possible, in reality any filter design is of little value if the design does not take into account the constituent component losses. If the unit cells were to be constructed using lumped components, most of the loss would originate from the series resistance of the inductors of the circuit. The capacitor's leakage resistances are typically negligible in most microwave-grade capacitors. In a separate simulation the series resistances of the inductors are included in the model, yielding the magnitude response of Fig. 4-28. The values for the resistance were taken using standard commercial microwave wire-wound inductors from Coilcraft, Inc.

As can be seen from Fig. 4-28, the insertion loss at mid-band ranges from 0.5 dB at f_4 (5 GHz) to 1.5 dB at f_2 (2.5 GHz). The return loss is around 13.5 dB in all bands. From these results, it can be seen that this type of design have an acceptable performance in a real-world application operating in similar frequency bands. At higher frequencies however, lumped components suffer from other parasitic effects such as the series or parallel resonance frequency, which would require a different type of implementation.

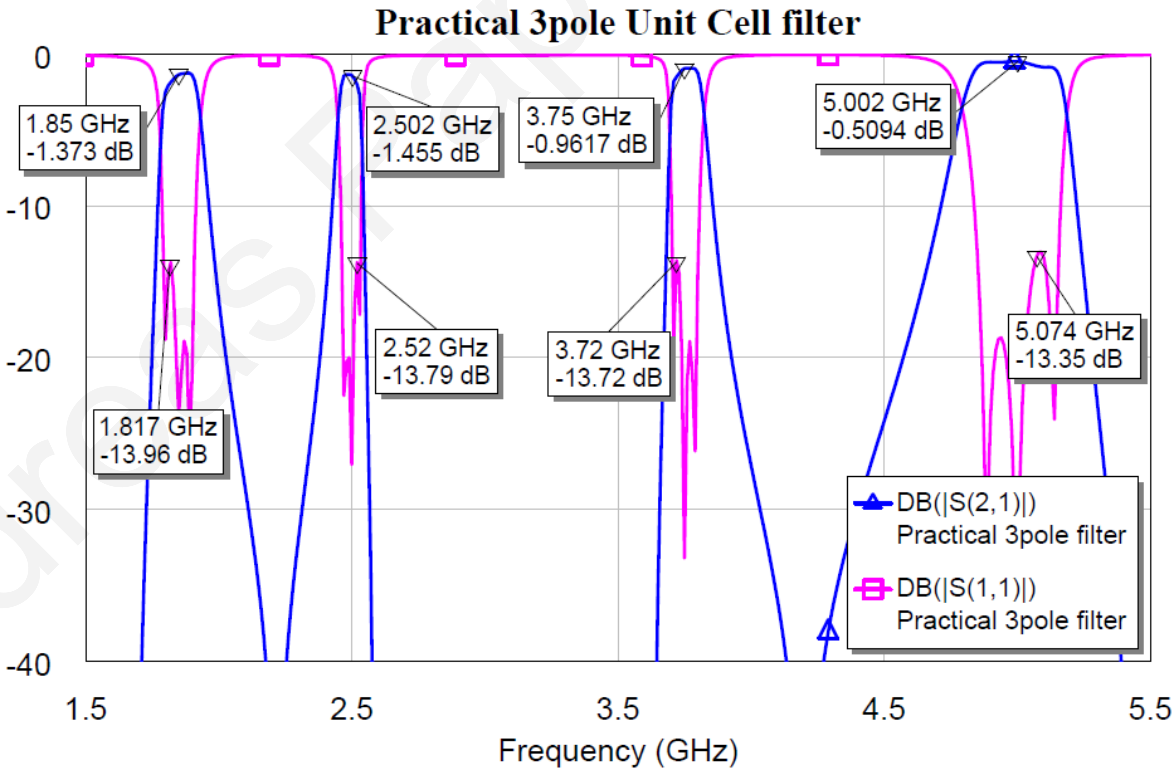

Fig. 4-28. Magnitude response of a realizable shorted $\lambda/4$ 3-pole filter including component losses

Furthermore, there is a significant size reduction benefit when using GNRI-TL unit cells. The filter using GNRI-TL unit cells would measure 38 mm in length and 18 mm in width. In contrast, at the lowest frequency of 1.85, a conventional shorted $\lambda/4$ 3-pole filter would measure 60.2 mm in length and 30.4 mm in width.

From the above filter designs, it can be seen that GNRI-TL theory can easily be applied as a straightforward means of designing any kind of narrowband conventional filter with a quad-band response by starting with a classical filter response (such as the shorted $\lambda/4$ BPF) and transforming it into a quad-band filter at the desired frequencies. When using this method, the bandwidth can be controlled through the variation of the impedance values of the unit cells, but in general, it is mostly suitable for narrowband designs. By varying the unit cells' impedances, a tradeoff is made with the return loss of the filter, so wider bandwidths would typically mean degraded return loss.

4.4 Summary

In this Chapter, a novel quad-band Wilkinson power divider was presented. This new type of Wilkinson divider replaced the conventional 70.7 Ohm/ 90^o transmission line sections with quad-band GNRI-TL unit cells, each with a Bloch impedance of 70.7 Ohms and a phase shift of 90^o at four different frequencies. Simulated and measured results were then compared.

A quad-band rat-race coupler was also presented in this Chapter. As in the case of the Wilkinson divider, the conventional transmission line sections were replaced by GNRI-TL unit cells of proper impedance and phase shift at four distinct frequencies. The modified GNRI-TL unit cells were designed using the host transmission line circuit parameter method in order to make the necessary component value corrections. Simulated and experimental results of both the single unit cell and the entire coupler were presented and compared.

Chapter 4 also discussed the method for the design of a quad-band shorted $\lambda/4$ 3-pole bandpass filter by means of replacing each transmission line section of the single-band conventional filter with GNRI-TL unit cells. The simulated magnitude and phase results were then shown for the ideal case with no component losses and for the case where component losses are taken into account, proving the feasibility of the design methodology for such filters.

Chapter 5

5 Complete Model of a GNRI-TL Unit Cell using Lossy Host Transmission Lines

During the course of this work, the main goal was to create a GNRI-TL model that would best describe the real world situation of successfully designing a metamaterial unit cell. Whereas so far, the host transmission line was considered lossless, in practice, the effects of the loss in the host TL have to be considered, or at least prove that they can be safely neglected. It might be true that for most microwave substrates these are typically very small and can be neglected, but in case the TL will be implemented on semiconductor material, they can be significant and the model has to be able to properly account for them.

5.1 Circuit Model

The general model of a transmission line can be seen in Fig. 5-1 below. The per-unit-length resistance, inductance, capacitance and conductance are denoted as *R', L', C'* and *G'* respectively.

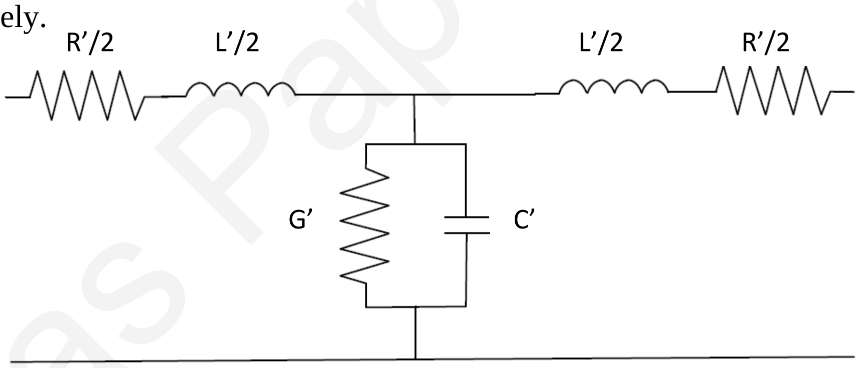

Fig. 5-1. Lossy Transmission Line circuit

It is a reasonable approximation to assume that each GNRI-TL unit cell will be connected on its input and output to small sections of loossy host transmission lines. The overall circuit model to be analyzed is shown in Fig. 5-2.

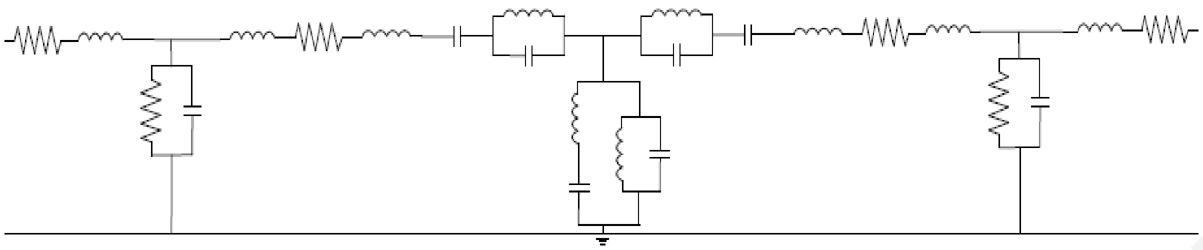

Fig. 5-2. GNRI-TL unit cell connected to low-loss host transmission lines

For a lossy transmission line the characteristic impedance is given by (5.1), [42].

$$Z_0 = \sqrt{\frac{R' + j\omega L'}{G' + j\omega C'}}\,. \tag{5.1}$$

If we consider a small length of lossy host transmission line l, the impedance of each of its series branches Z_{TL_H} and its admittance Y_{TL_V} are calculated as follows:

$$Z_{TL\_H} = \left(R + j\omega L_{TL}\right)/\,2 \tag{5.2}$$

$$Y_{TL\_V} = G + j\omega C_{TL}\,. \tag{5.3}$$

In (5.2) and (5.3), R, G, C_{TL} and L_{TL} are the actual resistance, conductance capacitance and inductance respectively incurred by the small transmission line segment l. The ABCD matrix of this transmission line segment is given in (5.4) as follows:

$$\begin{bmatrix} A2 & B2 \\ C2 & D2 \end{bmatrix} = \begin{bmatrix} 1 + Z_{TL\_H}Y_{TL\_V} & 2Z_{TL\_H} + Z_{TL\_H}^2 Y_{TL\_V} \\ Y_{TL\_V} & 1 + Z_{TL\_H}Y_{TL\_V} \end{bmatrix} \tag{5.4}$$

The ABCD matrix for the GNRI-TL unit cell is given in (1) and is repeated here for clarity:

$$\begin{bmatrix} A1 & B1 \\ C1 & D1 \end{bmatrix} = \begin{bmatrix} 1 + Z_h Y_v & Z_h(2 + Z_h Y_v) \\ Y_v & 1 + Z_h Y_v \end{bmatrix} \tag{5.5}$$

To obtain the overall ABCD matrix of the circuit schematic of Fig. 5-2, we need to use (5.3) and (5.4) by performing the following matrix multiplication:

$$\begin{bmatrix} A & B \\ C & D \end{bmatrix} = \begin{bmatrix} A2 & B2 \\ C2 & D2 \end{bmatrix} . \begin{bmatrix} A1 & B1 \\ C1 & D1 \end{bmatrix} . \begin{bmatrix} A2 & B2 \\ C2 & D2 \end{bmatrix} \tag{5.6}$$

which results in the following matrix:

$$\begin{bmatrix} A & B \\ C & D \end{bmatrix} = \begin{bmatrix} A2(A1A2 + B2C1) + C2(A2B1 + B2D1) & B2(A1A2 + B2C1) + D2(C2B1 + D2D1 \\ A2(C2A1 + D2C1) + C2(C2B1 + D2D1) & B2(C2A1 + D2C1) + D2(C2B1 + D2D1) \end{bmatrix} \tag{5.7}$$

By replacing $A2$ with $D2$ and $A1$ with $D1$, it can be verified that A=D, which is the expected result for a symmetric circuit.

5.2 Transmission Line Parameters

The next step in this development is to have the necessary equations to calculate the four transmission line parameters, namely, the per-unit-length resistance, inductance, capacitance and conductance, denoted as *R', L', C'* and *G'*.

Capacitance:

The characteristic impedance Z_0 of a microstrip transmission line on suspended in vacuum over its ground plane, is given by the following equation [21]:

$$Z_0 = \frac{\eta}{2\pi} \ln\left[\left(\frac{F1}{u} \right) + \sqrt{\frac{1}{(2/u)^2}} \right] \tag{5.8}$$

where

$$\eta = 120\pi \tag{5.9}$$

$$u = \frac{W}{h} \tag{5.10}$$

$$F1 = 6 + (2\pi - 6)e^{(-30.666/u)^{0.7528}} \tag{5.11}$$

The characteristic impedance Z_{0eff} of a microstrip transmission line on a substrate with dielectric constant ε_r is then given by [21]:

$$Z_{0eff} = \frac{Z_o}{\sqrt{\varepsilon_{eff}}} \tag{5.12}$$

where

$$\varepsilon_{eff} = \left(\frac{\varepsilon_r + 1}{2} \right) + \left(\frac{\varepsilon_r - 1}{2} \right) \left(1 + \frac{10}{u} \right)^{-ab} \tag{5.13}$$

and

$$a = 1 + \frac{1}{49} \ln\left[\frac{u^4 + \left(\frac{u}{52} \right)^2}{\left(u^4 + 0.432 \right)} \right] + \frac{1}{18.7} \ln\left[1 + \left(\frac{u}{18.1} \right)^3 \right] \tag{5.14}$$

$$b = 0.564 \left(\frac{\varepsilon_r - 0.9}{\varepsilon_r + 3} \right)^{0.053}. \tag{5.15}$$

The capacitance per unit length of the air transmission line is

$$C_0' = \frac{1}{cZ_0} \tag{5.16}$$

and that of the transmission line using a substrate is

$$C_{eff}' = \varepsilon_{eff} C_0' \,. \tag{5.17}$$

Since the symmetric unit cell is used in this work, the value for the capacitance of the host transmission line would use half the length *l* for its calculation, i.e, one section of length *l/2* is used on each side of the GNRI-TL. In other words,

$$C_{TL} = C_{eff}'(l/2) \tag{5.18}$$

Resistance:

The normalized series distributed resistance for the microstrip is given by [70]:

$$R1 = LR\left(\frac{1}{\pi} + \frac{1}{\pi^2}\ln\left(\frac{4\pi W}{t}\right)\right)\frac{R_m}{W} \tag{5.19}$$

Where LR is the loss ratio and it gives the increase in resistance that results from an unequal division of current between the strip and the ground plane. It is given by the following relation:

$$LR = 0.94 + 0.132\frac{W}{H} - 0.0062\left(\frac{W}{h}\right)^2 \tag{5.20}$$

which holds for 0.5<W/h<10.

The normalized series resistance of the ground plane is given by:

$$R2 = \left(\frac{W/h}{W/h + 5.8 + 0.03h/W}\right)\frac{R_m}{W} \tag{5.21}$$

which holds for 0.1<W/h<10

In the above equations, R_m is the skin-effect resistance given by:

$$R_m = \sqrt{\frac{\omega\mu}{\sigma}} \,. \tag{5.22}$$

The total series per-unit-length resistance is then simply:

$$R' = R1 + R2 \tag{5.23}$$

and the value of the resistance of the host transmission line on either side of the GNRI-TL is:

$$R = R'(l/2) \,. \tag{5.24}$$

Conductance:

The conductance per unit length *G*’ accounts for the dielectric loss of the substrate, described by the dielectric loss tangent, $\tan(\delta_\varepsilon)$ as follows:

$$G' = \omega C_{eff}' \tan(\delta_\varepsilon)\,. \tag{5.25}$$

The value of the conductance of the host transmission line on either side of the GNRI-TL is:

$$G = G'(l/2)\,. \tag{5.26}$$

Inductance:

For the calculation of the inductance per unit length *L’*, the external and internal part are computed separately. In the skin-effect range, where all conductor dimensions are large compared to the skin depth, the current flows only up to a small depth under the conductor surface. The external inductance L_{ext}' covering the magnetic field outside of the conductors is almost identical with the value in the lossless case and hence is frequency independent. One has:

$$L_{ext}' = \frac{1}{c^2 C_0'} \tag{5.27}$$

where C_0’ has been defined previously in (5.16).

Under skin-effect conditions, the internal inductance L_{int}', describing the magnetic field inside the conductors, is related to the resistance by (5.28) as follows:

$$L_{\text{int}}' = \frac{R_{se}'}{\omega} \tag{5.28}$$

where

$$R_{se} = 2 Z_{0eff}\, \alpha_c \tag{5.29}$$

$$\alpha_c = 7.0229 \cdot 10^{-6} \cdot A \frac{R_S Z_L \varepsilon_{eff}}{h} \left(\frac{W}{h} + \frac{0.667 \frac{W}{h}}{\frac{W}{h} + 1.444} \right) \tag{5.30}$$

which holds for W/h >1. In (5.30), *A* and R_s are defined as follows:

$$A = 1 + \frac{h}{W}\left(1 + \frac{1.25}{\pi} \cdot \ln\left(\frac{2h}{t}\right)\right) \tag{5.31}$$

$$R_S = \sqrt{\frac{\pi f \mu_0}{\sigma}}\,. \tag{5.32}$$

Thus, the total inductance per unit length in the skin-effect range is given simply by:

$$L' = L_{ext}' + L_{\text{int}}' \tag{5.33}$$

and the value for the inductance of the host transmission line section on either side of the GNRI-TL unit cell is:

$$L_{TL} = L_{eff}'(l/2)\,. \tag{5.34}$$

5.3 Theory development and analysis using lossy TL parameters

To test the ability of the complete GNRI-TL model theory to account for and rectify the effects of the lossy host Transmission Line, two simulations were run using the following assumptions:

Parameter	Value
F1	0.9 GHz
F2	1.55 GHz
F3	2.017 GHz
F4	2.45 GHz
Φ (phase shift at operating frequencies)	45^o
R.L.	>-14.1 dB
I.L.	< -0.1 dB
$Z_{0\_UnitCell}$	50 Ohms

Table 4. Unit Cell Requirements

Two different substrates have been used for the calculation of the transmission line parameters, one with a low dielectric constant and one with a high dielectric constant so that the effectiveness of the component corrections can be quantified for both cases, which represent the values of ε_r which practical microwave circuits would normally be implemented with. The first one is the Rogers RT/Duroid 5880 with ε_r=2.2 and $tan\delta$=0.0009 and the second is Rogers TMM13 with ε_r=12.85 and $tan\delta$=0.0019.

From the above unit cell requirements and using the equations from the original GNRI-TL theory [26], the set of ideal unit cell components are derived, as seen in Table 5 below :

Component Designation	Value
L_{hs}	5.96 nH
C_{hs}	2.17 pF
L_{hp}	0.24 nH
C_{hp}	29.55 pF
L_{vs}	20.75 nH
C_{vs}	0.35 pF
L_{vp}	6.10 nH
C_{vp}	2.12 pF

Table 5. Ideal Unit Cell Component values as derived from original theory

The above component values result in the S-parameter magnitude and phase plots shown in Fig. 5-3 and Fig. 5-4 below:

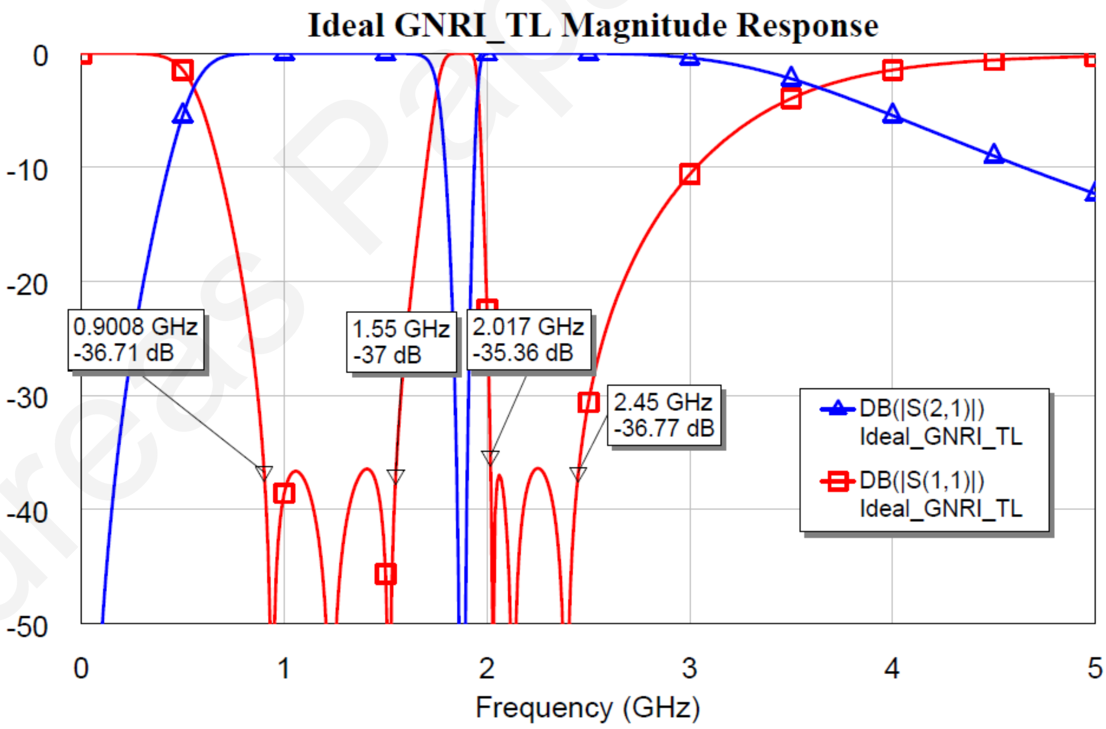

Fig. 5-3. S-Parameter magnitude response of ideal GNRI-TL unit cell

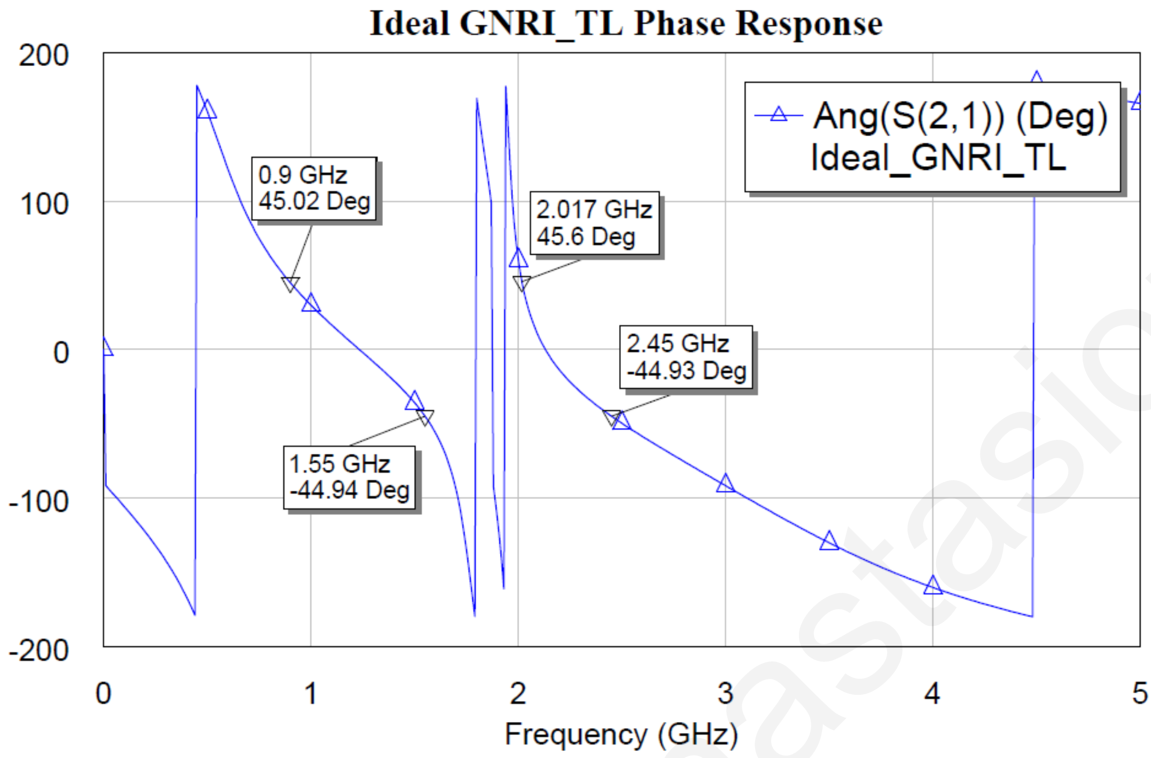

Fig. 5-4. Phase response of the Ideal GNRI-TL unit cell.

As can be seen from Fig. 5-3 and Fig. 5-4, all requirements for the unit cell are satisfied, as was expected for the ideal case.

If the above components of the unit cell were to be interconnected using short 50 Ohm microstrip line segments on a RT/Duroid 5880 and a TMM13 substrate under the assumptions of Table 6 , we would end up with the following transmission line parameters shown in Table 7 :

TL Physical Parameter	RT5880	TMM13
Length (*l*)	5 mm	5 mm
Width (*W*)	1.54 mm	0.56 mm
Substrate Height (*h*)	0.508 mm	0.762 mm
Trace thickness (*t*)	0.01788 mm	0.01788 mm
ε_r	2.2	12.8
$tan\delta$	0.0009	0.0019
Copper Conductivity	$5.8\text{x}10^8$ S/m	$5.8\text{x}10^8$ S/m

Table 6. Host TL physical parameters for RT5880 and TMM13

TL Circuit Parameter (for a length *l/2*=2.5mm)	RT5880	TMM13
C_{TL}	0.226 pF	0.48 pF
L_{TL}	0.578 nH	1.2 nH
R	41pΩ-0.29nΩ from 100MHz-5GHz	73pΩ-0.52nΩ from 100MHz-5GHz
G	0.128 $\mu\Omega^{-1}$-6.39 $\mu\Omega^{-1}$ from 100MHz-5GHz	2.71 $\mu\Omega^{-1}$-136 $\mu\Omega^{-1}$ from 100MHz-5GHz

Table 7. Host microstrip TL constituent parameters for RT5880 and TMM13 substrate

To be exact, L_{TL} and R and G do have a frequency dependant component. Fig. 5-5 and Fig. 5-6 below show that the frequency dependence of the TL inductance is negligible and for all practical purposes for the frequencies of interest, can be assumed constant. For R and G however, even though their values at these frequencies are small, their variation is not and cannot be neglected.

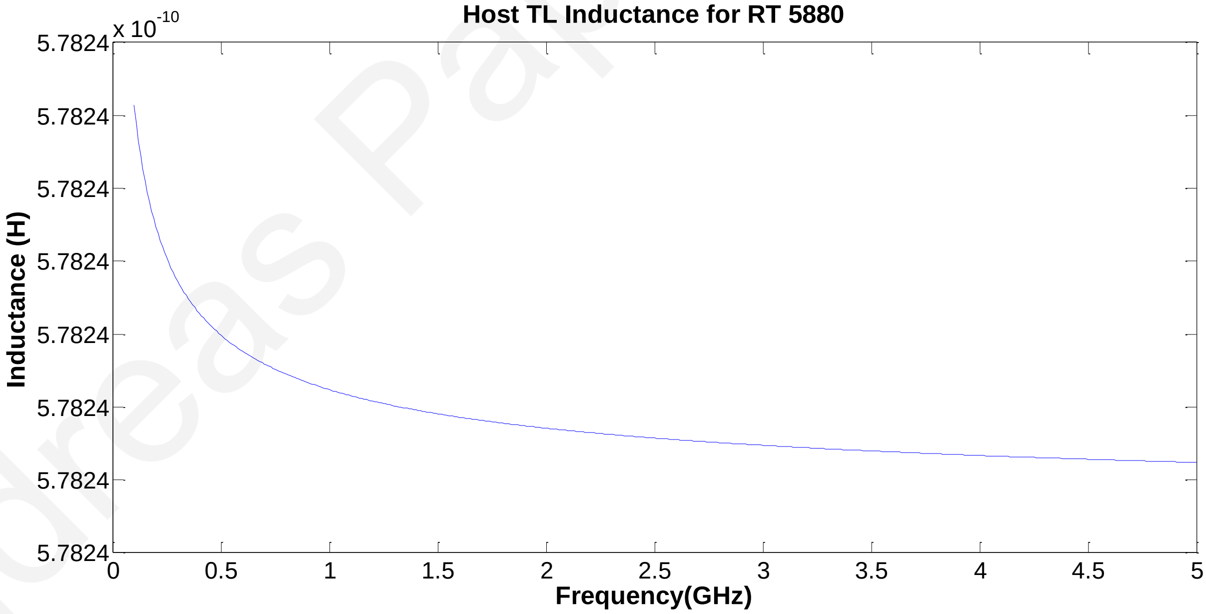

Fig. 5-5. Plot of inductance vs. frequency for a 5mm 50 Ohm host TL section on RT/ Duroid 5880

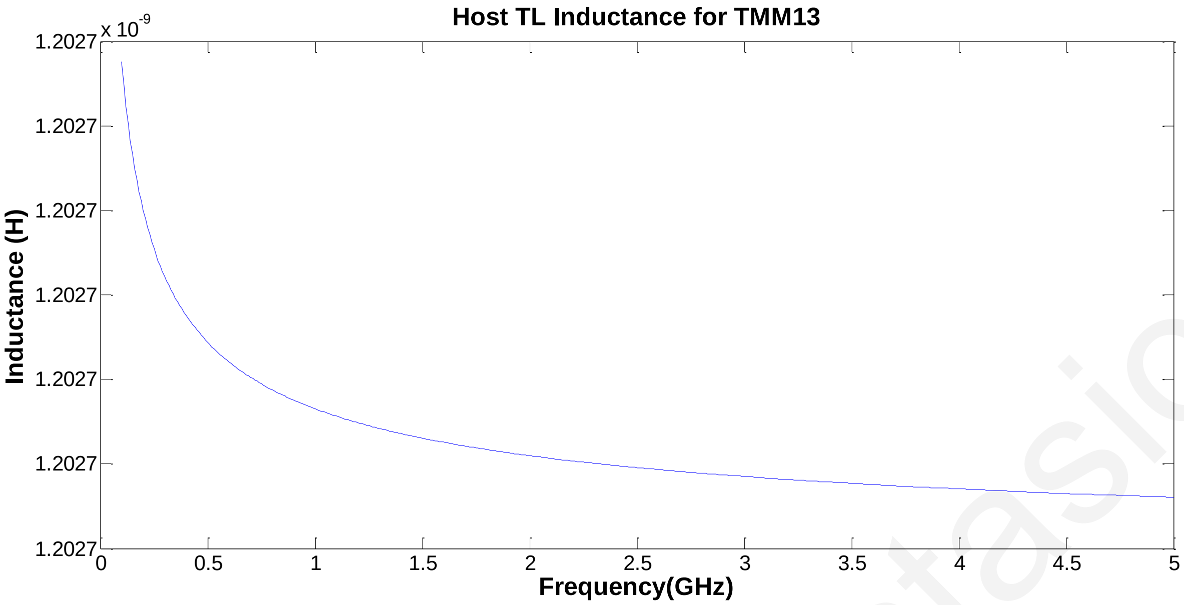

Fig. 5-6.Plot of inductance vs. frequency for a 5mm 50 Ohm host TL section on TMM13

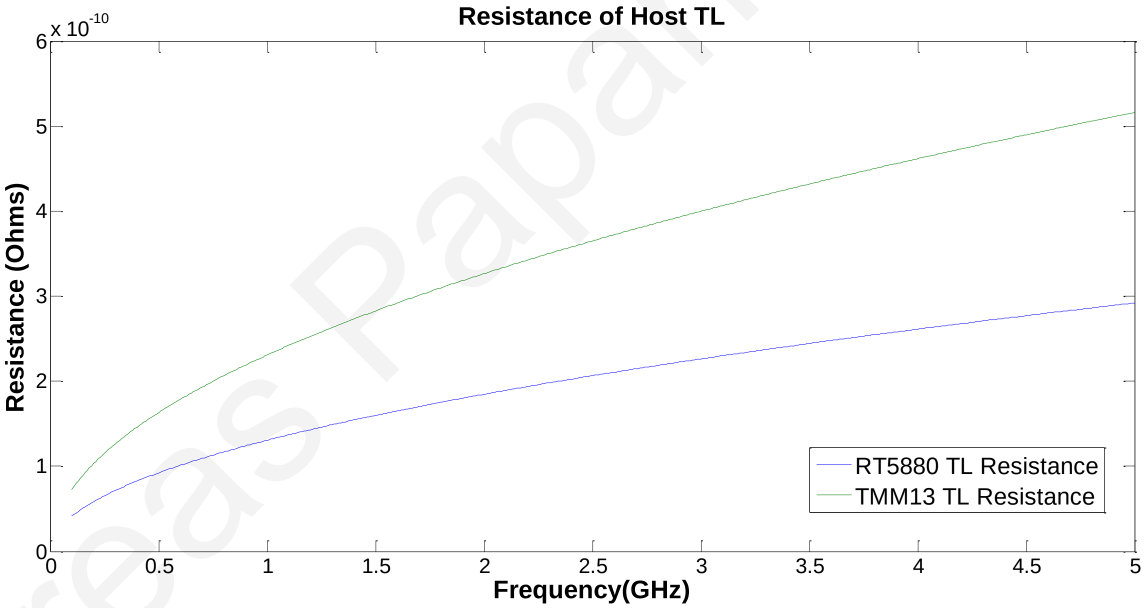

Fig. 5-7. Plot of resistance vs. Frequency for 5mm host TL sections on RT5880 and TMM13

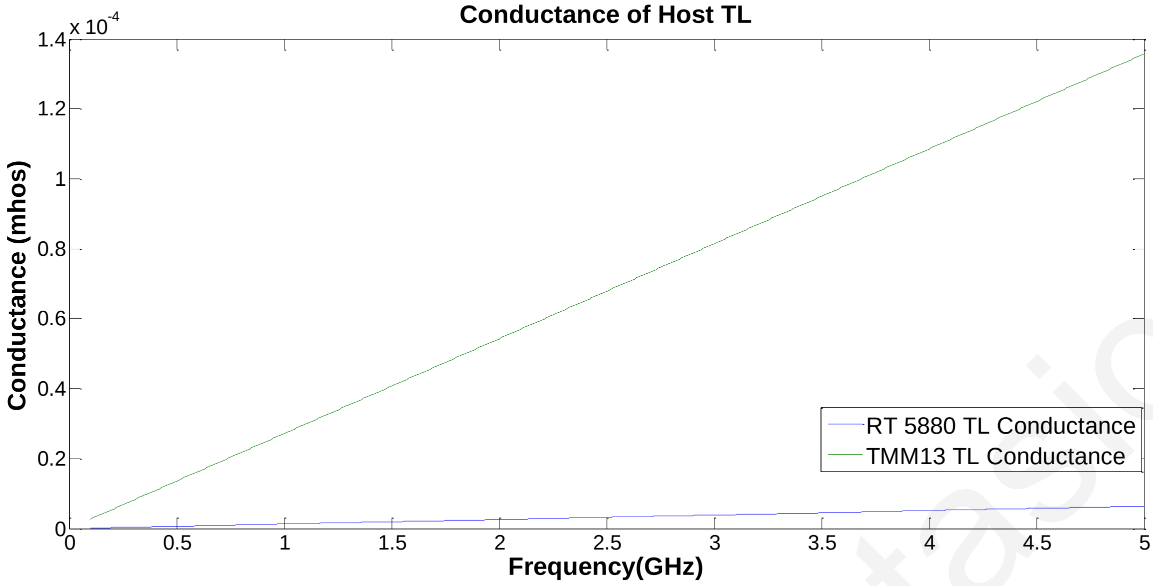

Fig. 5-8. Plot of conductance vs. frequency for 5mm host TL sections on RT5880 and TMM13

Using the above TL parameter results, the ABCD matrix parameters (5.4) can be calculated from the host TL impedance and admittance Z_{TL_H} (5.2) and Y_{TL_V} (5.3) respectively. This host TL ABCD matrix is used in turn to calculate the new ABCD matrix of the resultant unit cell, as given by (5.7) previously. The dispersion diagram of the resultant unit cell using host TLs on RT5880 and TMM 13 are given in below, with the dispersion of the ideal GNRI-TL Unit cell given for comparison and for a visualization of the degree of deviation from the ideal case, if a unit cell is made using the theoretical component values.

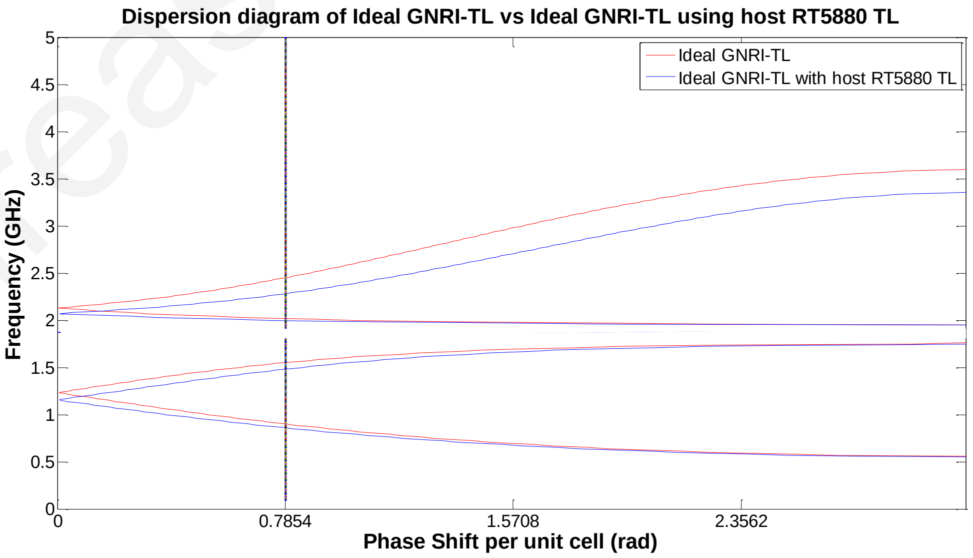

Fig. 5-9. Dispersion comparison of ideal GNRI-TL unit cell vs. ideal GNRI-TL unit cell using RT5880 host TL

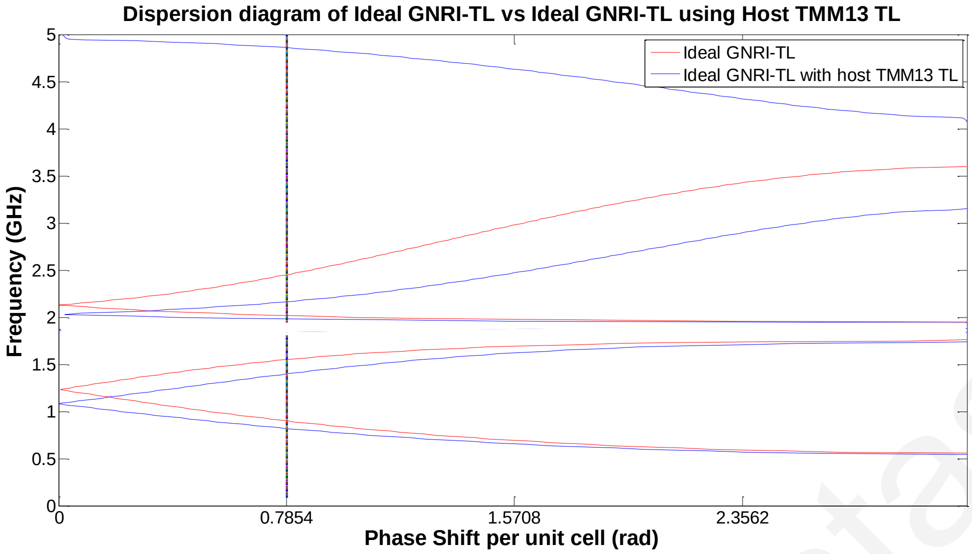

Fig. 5-10. Dispersion comparison of ideal GNRI-TL unit cell vs. ideal GNRI-TL unit cell using TMM13 host TL

From the above figures, it is immediately obvious that the β=0 frequencies are shifted and that the frequencies where the desired 45 degree phase shift occurs (as indicated by the intersection of the black vertical line with the blue dispersion curve) do not coincide with the required four operating frequencies. Table 8 below shows the resultant frequencies as well as the deviation from the desired frequencies.

Operating Frequency	RT5880 frequency	Deviation (%)	TMM13 frequency	Deviation (%)
0.9 GHz	0.859 GHz	-4.56	0.820 GHz	-8.89
1.55 GHz	1.481 GHz	-4.45	1.298 GHz	-9.81
2.017 GHz	1.998 GHz	-0.94	1.982 GHz	-1.74
2.45 GHz	2.281 GHz	-6.90	2.163 GHz	-11.71

Table 8. Resultant operating frequencies when using theoretical GNRI-TL component values with host TL

It is thus clear that the effect of the host TLs will result in a unit cell far from the desired one.

In the above calculation, the effects of the resistance and conductance of the transmission line are also included. It is now worth noting that these effects cannot be removed, since they represent ohmic and dielectric losses in the copper and the substrate. The effects of the inductance and capacitance can, however, be largely removed. To see how the effect of the transmission line can be removed, the mechanism of the frequency shift has to be first understood. By inspection of Fig. 5-2, it can be seen that the added TL inductance L_{TL}, will result in the pulling of the resonant frequency ω_{hs} by a certain amount

$$\Delta\omega_{hs} = \omega_{hs\_bef\_corr} - \omega_{hs} \tag{5.35}$$

In (5.35),

$$\omega_{hs\_bef\_corr} = \sqrt{\frac{1}{(L_{hs} + L_{TL}) \bullet C_{hs}}}, \tag{5.36}$$

Similarily, the shunt capacitance of the host TL, will result approximately in the pulling of the resonant frequency ω_{vp} by the amount

$$\Delta\omega_{vp} = \omega_{vp\_bef\_corr} - \omega_{vp} \tag{5.37}$$

In (5.37),

$$\omega_{vp\_bef\_corr} = \sqrt{\frac{1}{L_{vp} \bullet (C_{vp} + 2C_{TL})}}. \tag{5.38}$$

The factor of 2 for C_{TL} comes from the fact that in the calculations for C_{TL} only half the transmission line was used and one section of length *l/2* is used on each side of the GNRI-TL, as also expressed by equation (5.18). This approximation for the shunt TL capacitance being added to C_{vp} as a parallel capacitance only works due to the small size of the Host TL (smaller than λ/10 at the highest frequency of interest) and cannot be generalized beyond that, which of course is in agreement with the concept of the unit cell itself. It is also important to note that $\omega_{hs\_bef\_corr}$ and $\omega_{vp\_bef\_corr}$ are the resultant equivalent unit cell's series resonant frequency of the horizontal branch and the parallel resonant frequency of the vertical branch. For clarity, this equivalent unit cell would look like the one shown in Fig. 5-11 below where the transmission line inductance and capacitance would be consolidated into the components of this new unit cell (no TL resistance and conductance are shown in this figure).

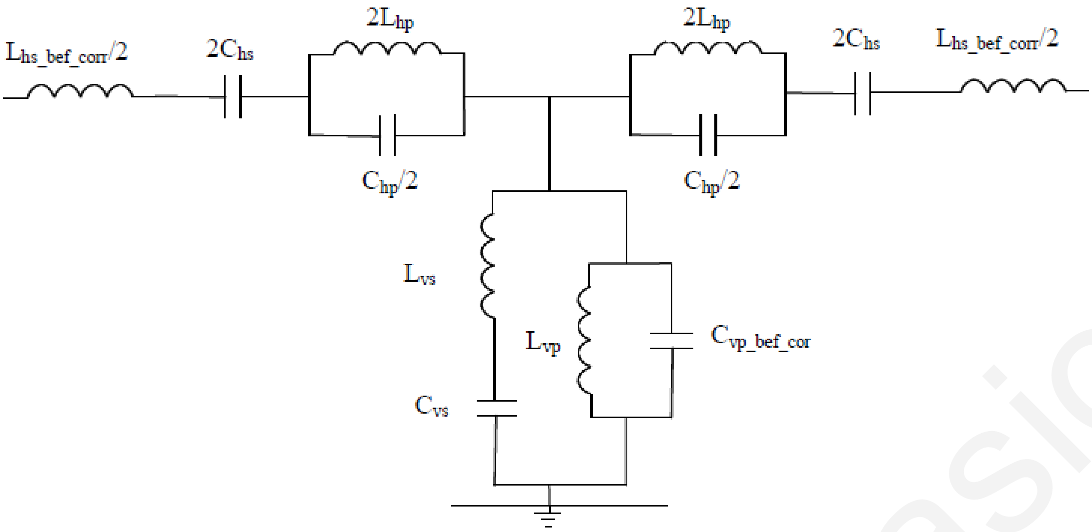

Fig. 5-11. Resultant simplified GNRI-TL schematic component values affected by the host TL and before any correction operations

To verify the applicability of the equivalent unit cell of Fig. 5-11, its dispersion is plotted and compared to the dispersion of the schematic shown in Fig. 5-2, for both substrates. These two plots are shown below:

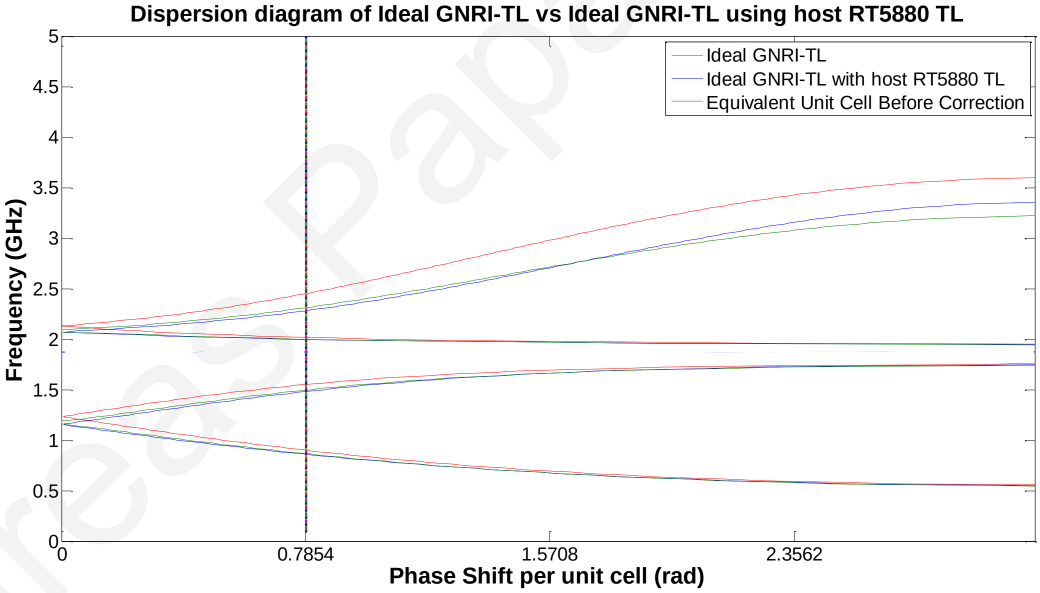

Fig. 5-12. Dispersion comparison of (approximately) equivalent unit cell circuit for the RT5880 case

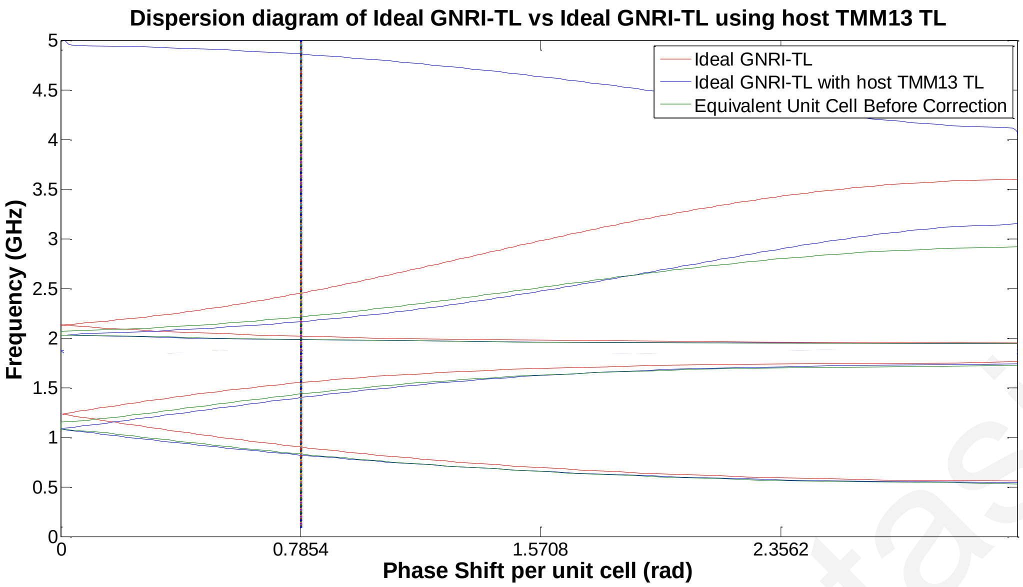

Fig. 5-13. Dispersion comparison of (approximately) equivalent unit cell circuit for the TMM13 case

From Fig. 5-12 and Fig. 5-13 above, it can be seen that the blue curve, which corresponds to the circuit of Fig. 5-2, closely tracks the green curve, which corresponds to the circuit of Fig. 5-11. This implies that the two circuits are very similar indeed and the approximation is a valid one.

So if :

$$L_{hs\_bef\_corr} = L_{hs} + L_{TL} \tag{5.39}$$

and

$$C_{vp\_bef\_corr} = C_{vp} + 2C_{TL} \tag{5.40}$$

it is reasonable then that in order to restore the resonant frequencies to the original levels, the following corrections need to be made to the original GNRI-TL unit cell component values:

$$L_{hs\_corr}=L_{hs} - L_{TL} \tag{5.41}$$

$$C_{vp\_corr}=C_{vp} - 2C_{TL}. \tag{5.42}$$

The amount of shift in frequency of the resonators will not be the same, however, i.e $\Delta\omega_{hs} \neq \Delta\omega_{vp}$. Thus if only these corrections given by (5.41) and (5.42) are performed, it is found that the unit cell still needs to be further tuned to recover the original (as specified) operation. The reason for that is because one of the conditions for the closed-stopband condition ($\omega_{hs} = \omega_{vp}$) will no longer be met for the new and corrected unit cell and as a result the zero frequencies of the horizontal and vertical branch of the corrected unit cell are no longer equal. To circumvent this problem, the resonator that deviates most from the original resonant frequency is chosen to be used as the new corrected resonant frequency of the other. So assuming $\Delta\omega_{vp} > \Delta\omega_{hs}$,, then

$$\omega_{vp\_bef\_corr} = \sqrt{\frac{1}{L_{vp}C_{vp\_bef\_corr}}} \tag{5.43}$$

$$\omega_{vp\_\%\_bef\_corr}=100\omega_{vp\_bef\_corr}/\omega_{vp} \tag{5.44}$$

$$\omega_{vp\_change\_from\_100\%}=100- \omega_{vp\_\%\_bef\_corr} \tag{5.45}$$

$$\omega_{vp\_\%\_corr}=100+\omega_{vp\_change\_from\_100\%} \tag{5.46}$$

$$\omega_{vp\_corr}=\omega_{vp}\cdot\omega_{vp\_\%\_corr}/100 \tag{5.47}$$

$$L_{vp\_corr} = \sqrt{\frac{1}{\omega^2_{vp\_corr}C_{vp\_corr}}} \tag{5.48}$$

and by setting

$$\omega_{hs\_corr} = \omega_{vp\_corr} \tag{5.49}$$

the value of C_{hs_corr} can be found as:

$$C_{hs\_corr} = \frac{1}{\omega^2_{hs\_corr}L_{hs\_corr}}. \tag{5.50}$$

Furthermore, to keep the closed stopband condition, (5.51) and (5.55) below also have to hold:

$$\omega_{hshp\_corr}=\omega_{vsvp\_corr} \tag{5.51}$$

where ω_{hshp_corr} and ω_{vsvp_corr} are defined as:

$$\omega_{hshp}=4/(L_{hs\_corr}C_{hp\_corr}) \tag{5.52}$$

$$\omega_{vsvp}=1/(L_{vs\_corr}C_{vp\_corr}) \tag{5.53}$$

which yields the following relation:

$$L_{vs\_corr}=L_{hs\_corr}C_{hp\_corr}/4C_{vp\_corr}. \tag{5.54}$$

and

$$\omega_{hp}=\omega_{vs=}\ \omega_{or} \tag{5.55}$$

where ω_{hp} and ω_{vs} are defined as :

$$\omega_{hp}=1/(L_{hp}C_{hp}) \tag{5.56}$$

$$\omega_{vs}=1/(L_{vs\_corr}C_{vs\_corr}) \tag{5.57}$$

which yields the following relation:

$$L_{vs\_corr}=L_{hs\_corr}C_{hp\_corr}/C_{vs\_corr}. \tag{5.58}$$

Setting (5.54)=(5.58) we obtain

$$C_{vs\_corr}=\frac{4L_{hp\_corr}C_{vp\_corr}}{L_{hs\_corr}}. \tag{5.59}$$

At this point the last of the corrected component values can be found as follows:

$$L_{vs\_corr}=\sqrt{\frac{1}{\omega_{vs}^{2}C_{vs\_corr}}}. \tag{5.60}$$

To apply the above equations and test their validity, the dispersion plots are regenerated using the new corrected component values, as shown in Fig. 5-14 and Fig. 5-15.

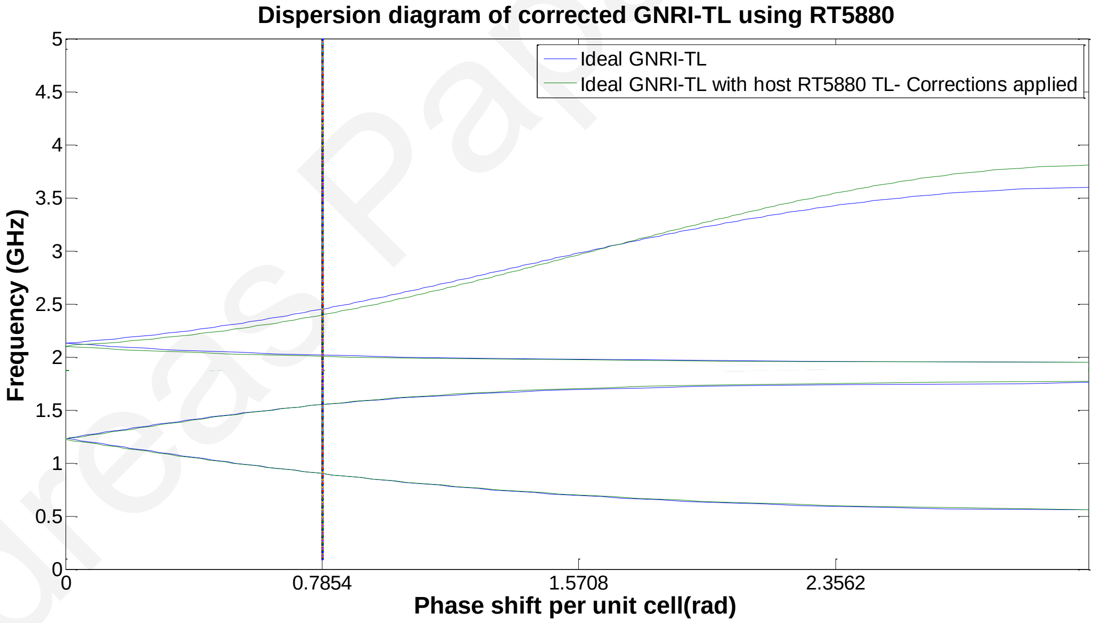

Fig. 5-14. Plot of the corrected RT5880-GNRI-TL dispersion relation

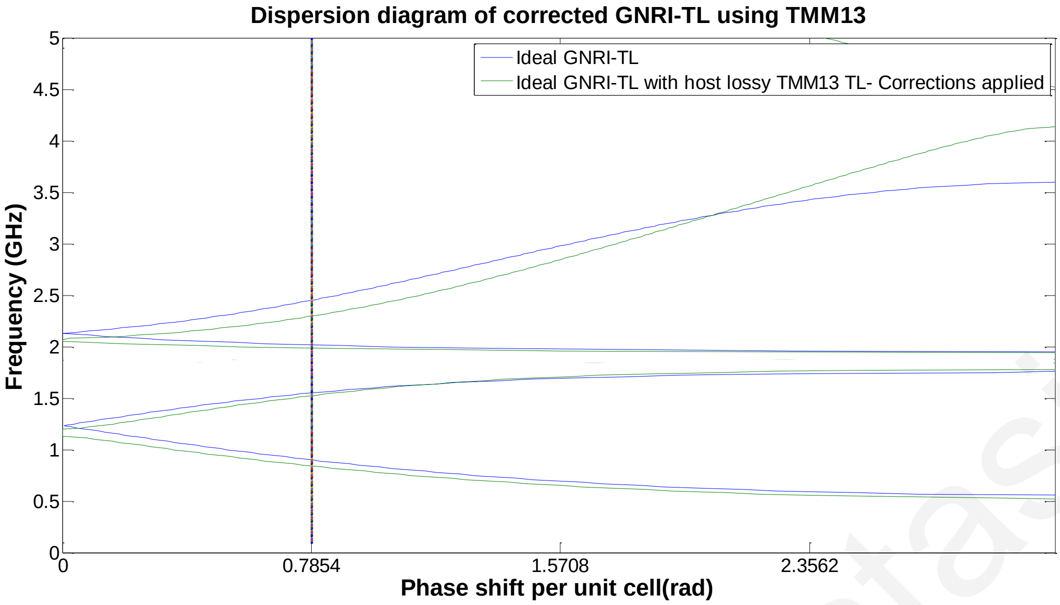

Fig. 5-15. Plot of the corrected TMM13-GNRI-TL dispersion relation

Table 9 below shows the new resultant operating frequencies as well as the new deviations from the desired frequencies.

Operating Frequency	**Corrected RT5880 frequency**	**Deviation (%)**	**Corrected TMM13 frequency**	**Deviation (%)**
0.9 GHz	0.900 GHz	0	0.841 GHz	-6.56
1.55 GHz	1.55 GHz	0	1.524 GHz	-1.68
2.017 GHz	2.006 GHz	-0.55	1.987 GHz	-1.49
2.45 GHz	2.397 GHz	-2.16	2.296 GHz	-6.29

Table 9. Comparison of corrected frequencies to the design ones and percentage deviation

The corrected frequencies are closer now to the design frequencies by the amounts shown in Table 10.

	GNRI-TL with RT5880 Host TL			**GNRI-TL with TMM13 Host TL**		
Operating Frequency	**Initial Deviation (%)**	**Corrected Deviation (%)**	**Improvement (%)**	**Initial Deviation (%)**	**Corrected Deviation (%)**	**Improvement (%)**
0.9 GHz	-4.56	0	**100**	-8.89	-6.56	**26.3**
1.55 GHz	-4.45	0	**100**	-9.81	-1.68	**89.7**
2.017 GHz	-0.94	-0.55	**42.1**	-1.74	-1.49	**14.3**
2.45 GHz	-6.90	-2.16	**68.6**	-11.71	-6.29	**46.3**

Table 10. Percentage of frequency deviation improvement after corrections

It can be seen from the above table as well as by visual inspection of the dispersion graphs, that there is a very significant improvement in the resultant frequencies, which proves that the above technique can be used as a good tool in designing realizable quad-band metamaterial devices. Whereas for the NRI-TL unit cell case, the effects of the host transmission line can be used completely as an integral part of the model, in the case of the GNRI-TL unit cell, an approximation is made with respect to the subtraction of the TLs shunt capacitance from the unit cell's $C_{vp.}$ Because of this, it is understood that the developed model and methodology has its limitations with respect to its applicability and special care has to be taken regarding the electrical length of the structure itself. This is the reason why the performance after the component corrections on the complete GNRI-TL model deviate from the ideal case as the physical size of the structure becomes longer, or equivalently as higher dielectric constant substrates are used, as shown previously. This is also the reason why the S-parameters after the corrections cannot be expected to coincide with the ones in the ideal GNRI-TL case. Instead, the aim is to enable the corrections to provide an acceptable performance for the specific design. The following graphs, compare the insertion loss and return loss of the ideal GNRI-TL to the case of the corrected GNRI-TL.

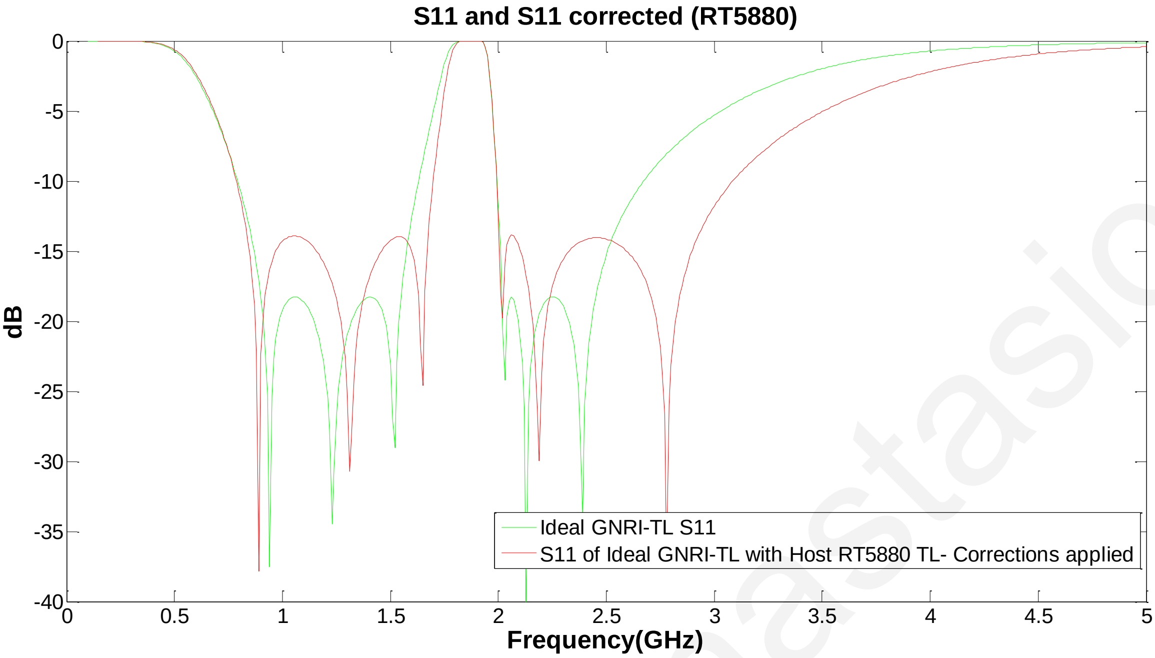

Fig. 5-16. Return loss comparison between ideal GNRI-TL and corrected GNRI-TL unit cells for RT5880

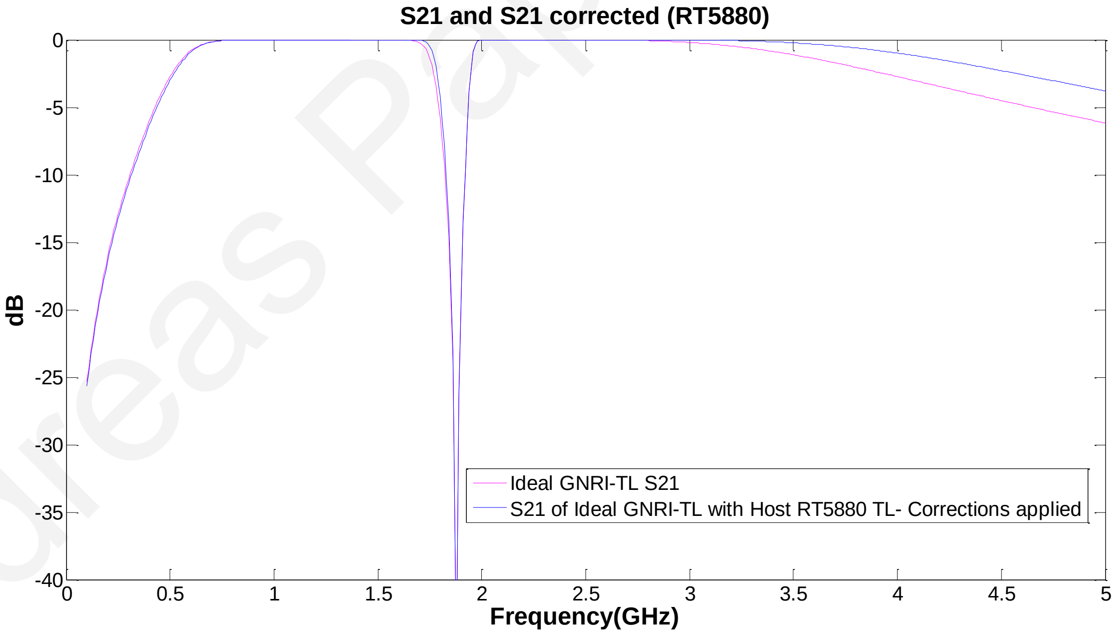

Fig. 5-17. Insertion loss comparison between ideal GNRI-TL and corrected GNRI-TL unit cells for RT5880

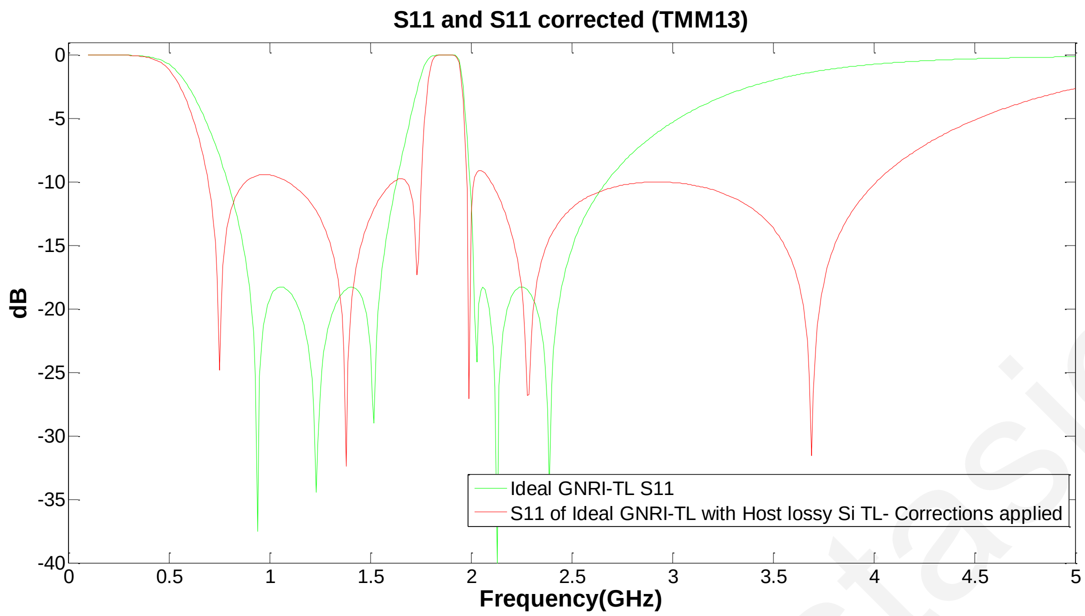

Fig. 5-18. Return Loss comparison between ideal GNRI-TL and corrected GNRI-TL unit cells for TMM13

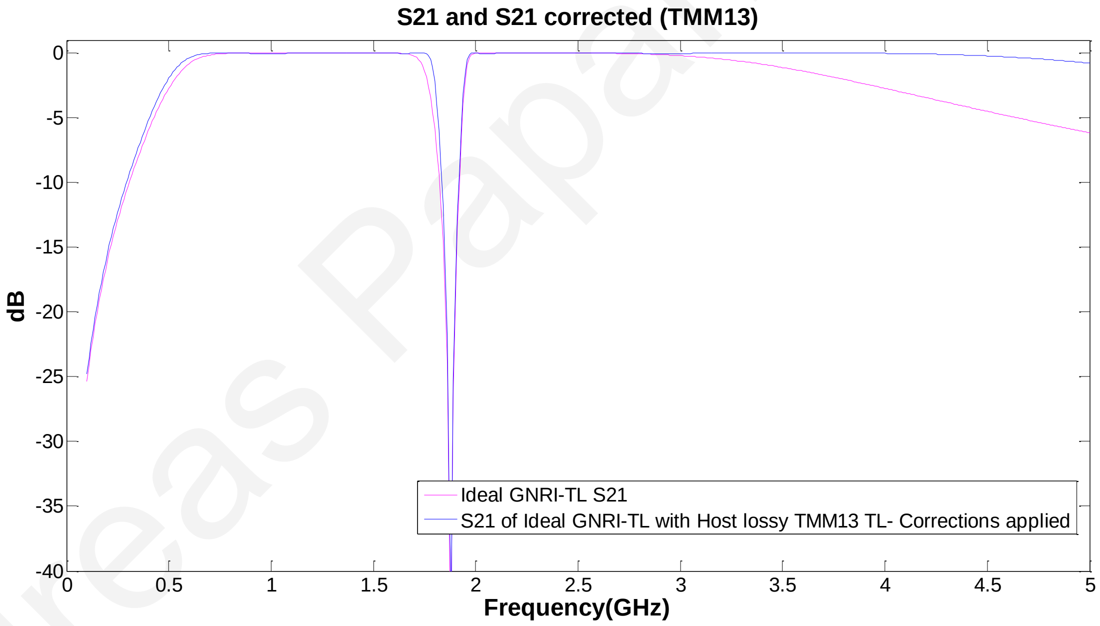

Fig. 5-19. Insertion loss comparison between ideal GNRI-TL and corrected GNRI-TL unit cells for TMM13

Even though the shape of the return loss performance in Fig. 5-16 and Fig. 5-18 seems distorted compared to the ideal case, it is 18.3 dB or better in all four operating frequencies, which satisfies the requirements set out in Table 4. The insertion loss also satisfies those requirements, thus the corrections made are useable in a realizable design.

5.4 Loss mechanisms of the Complete GNRI-TL model

It is also worth noting that the corrections developed above, do not rectify any effects the transmission line resistance and conductance have on the performance of the unit cell. Where we would expect the resistance and conductance to have an effect is the insertion loss of the unit cell. The comparison is made between the insertion loss of the GNRI-TL unit cell on its own, and the case when the host TL is added, in Fig. 5-20 and Fig. 5-21 below.

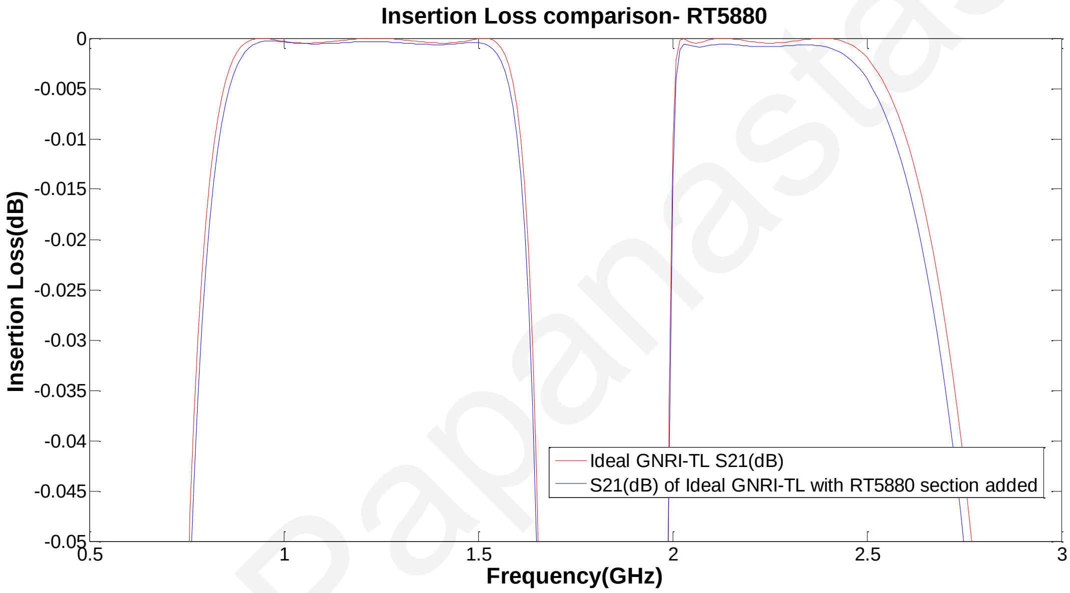

Fig. 5-20. Comparison of Insertion Loss for the ideal GNI-TL vs. the case of ideal GNRI-TL + RT5880 Host TL

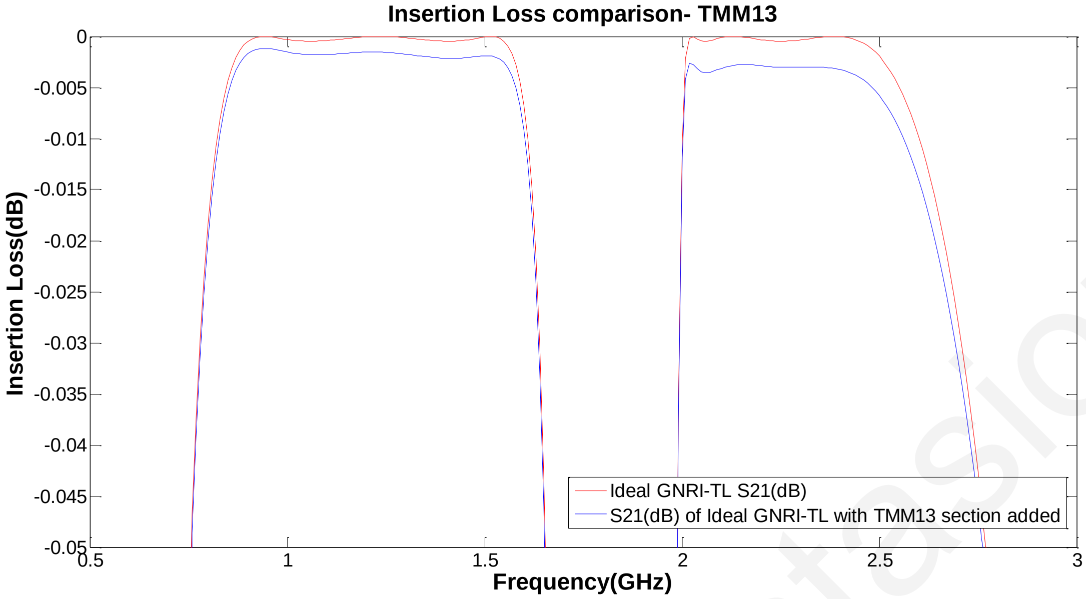

Fig. 5-21. Comparison of Insertion Loss for the ideal GNI-TL vs. the case of ideal GNRI-TL + TMM13 Host TL

By observation, the insertion loss for the case of using the TMM13 transmission line is more prominent (albeit still very small) than the case of the RT5880 substrate. The reason for this is the higher conductivity losses that come from the higher loss tangent of that substrate as well as its significantly higher dielectric constant. The ohmic (resistive) losses are expected to be very similar and only differ due to the geometry of the host TL.

To quantify how much of loss comes from resistive and the conductive parts of the TL, first *R* and subsequently *G* have been deliberately set to zero. The graphs in Fig. 5-22 and Fig. 5-23 show the insertion loss effect of the host TLs conductance alone, whereas the ones in Fig. 5-24 and Fig. 5-25 show the resistance’s effect on the host TLs insertion loss.

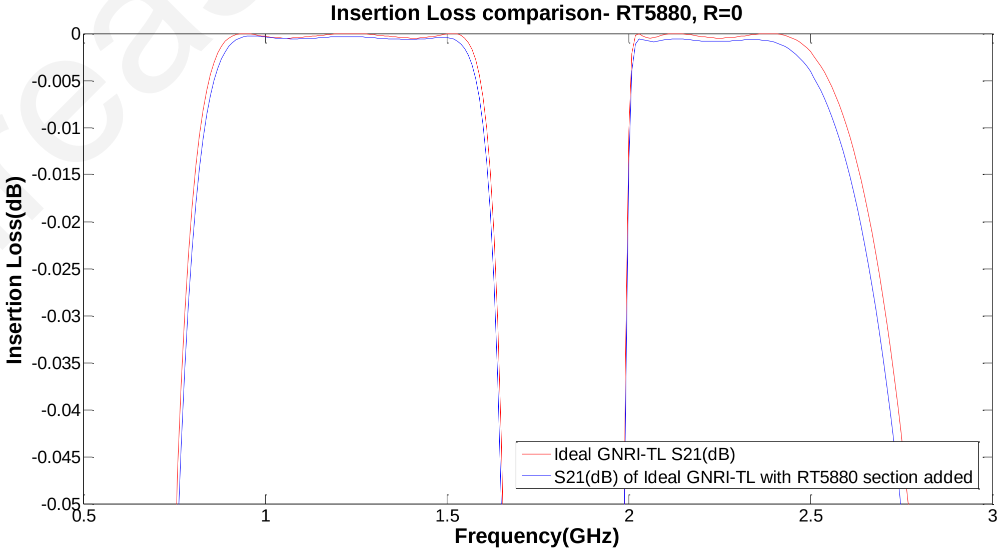

Fig. 5-22. Comparison of insertion loss between ideal GNRI-TL case vs. ideal GNRI-TL with RT5880 TL after neglecting the effects of the TL’s resistance

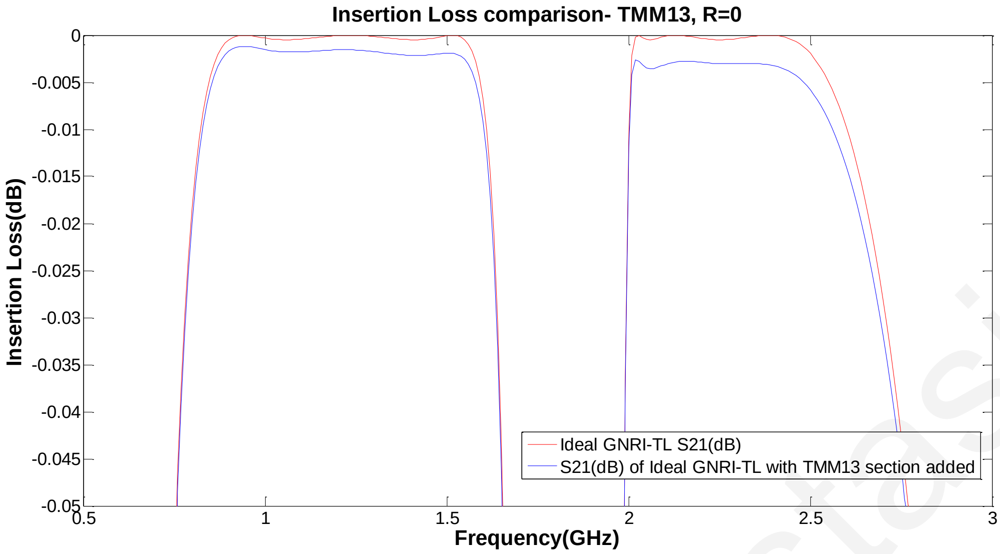

Fig. 5-23. Comparison of insertion loss between ideal GNRI-TL case vs. ideal GNRI-TL with TMM13 TL after neglecting the effects of the TL's resistance

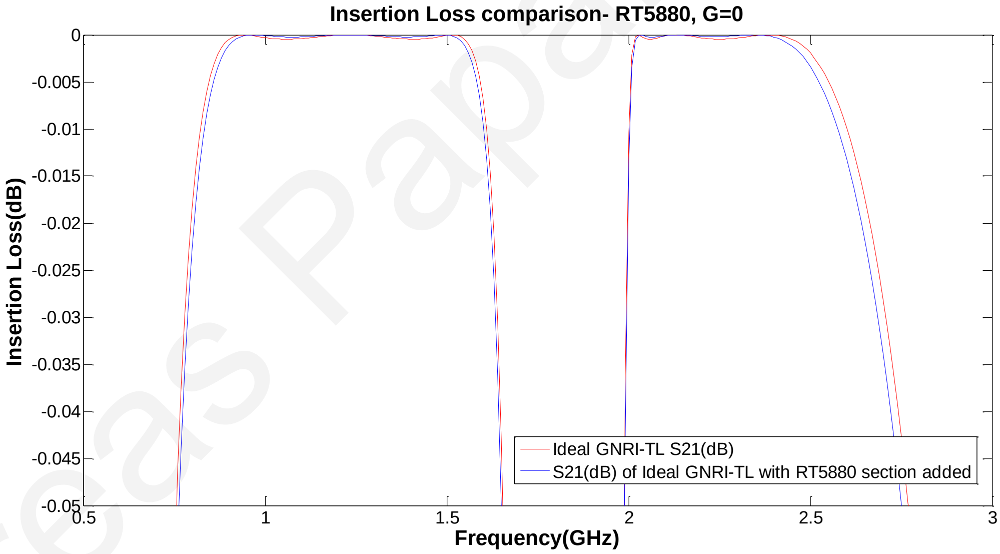

Fig. 5-24. Comparison of insertion loss between ideal GNRI-TL case vs. ideal GNRI-TL with RT5880 TL after neglecting the effects of the TL's conductance

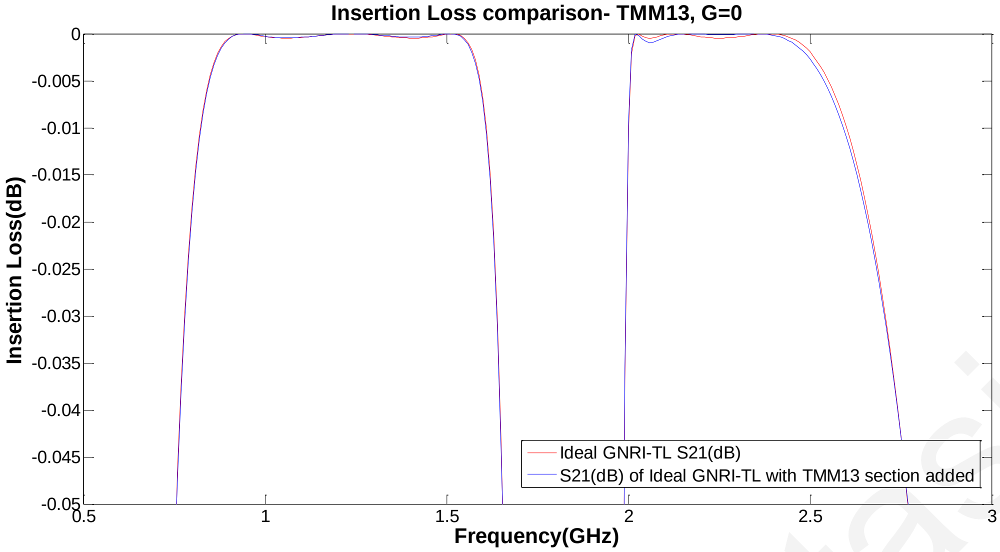

Fig. 5-25. Comparison of insertion loss between ideal GNRI-TL case vs. ideal GNRI-TL with TMM13 TL after neglecting the effects of the TL's conductance

In Table 11 below, the losses originating from the resistance and conductance (at the lowest and the highest frequency) for both substrates are shown separately.

R=0, *G*≠0			
	GNRI-TL I.L. (dB)	RT5880 I.L. (dB)	TMM13 I.L. (dB)
0.9 GHz	0.000475	0.001382	0.001649
2.45 GHz	0.000475	0.001904	0.00403
G=0, *R*≠0			
	GNRI-TL I.L. (dB)	RT5880 I.L. (dB)	TMM13 I.L. (dB)
0.9 GHz	0.000475	0.00115	0.0005569
2.45 GHz	0.000475	0.00124	0.0009353

Table 11. Resistive and conductive losses for RT5880 and TMM13 substrate materials

Table 11 shows that conductive losses are greater than the respective resistive ones, thus contribute more to the overall losses of the structure. The frequency dependence is also greater due to the conductance compared to the resistance of the host TL. Therefore, the choice of the dielectric becomes crucial at higher frequencies. For the frequencies of interest and for the host TLs with the physical characteristics chosen previously, the effects of *R* and *G* can be safely neglected. At much higher frequencies or with substrates of much higher loss tangent, these losses should be quantified and possibly taken into account during the design phase. As an extreme case, if a material with *tanδ*=0.1 is considered for hosting the TLs, the insertion loss plot of the GNRI-TL would look like the one in Fig. 5-26.

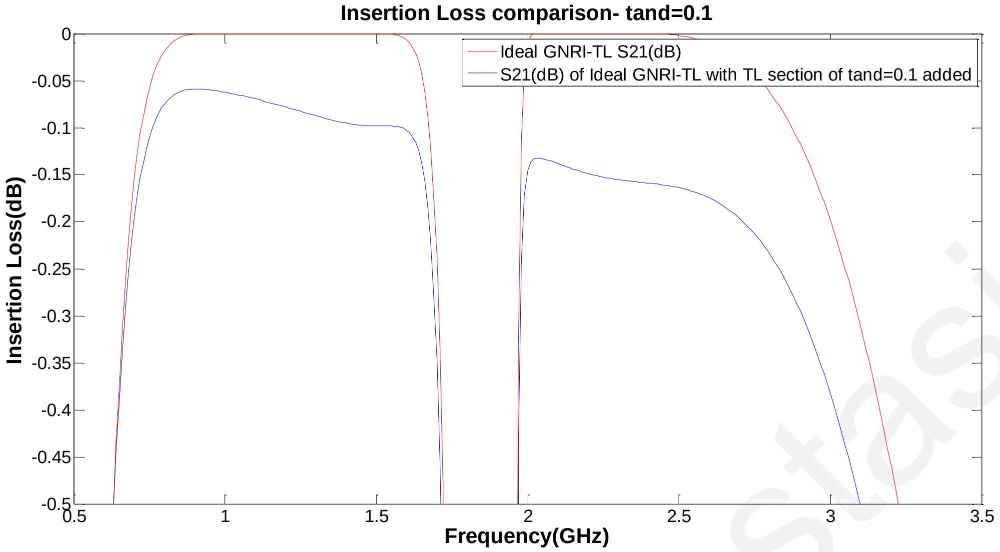

Fig. 5-26. Comparison of insertion loss between ideal GNRI-TL case vs. ideal GNRI-TL using a substrate of tanδ=0.1 for its host TL

Only at such extreme values of the loss tangent does the insertion loss begin to degrade significantly (0.16 dB at 2.45 GHz) with the lengths of TL typically used to host a GNRI-TL unit cell.

Chapter 6

6 Conclusions

6.1 Review of work

In this thesis, the negative-refractive-index transmission-line theory has been reviewed and analyzed based on the combination of positive-refractive-index and negative-refractive-index transmission line segments. The generalized negative-refractive-index transmission-line theory has also been reviewed as the groundwork laying out the foundations for the theory developed in this work.

The analysis of the NRI-TL unit cell has been extended to the case where the impedances of the input and output series branches of the unit cell are not equal. In this fashion, the asymmetrical NRI-TL unit cell can be used for the design of single-band bandpass filters. The new dispersion relation has been developed and the equations needed to calculate the required component values presented. The simulated results of two NRI-TL unit cells in a back-to-back configuration were shown and compared to an equivalent Chebyshev filter. Also, the analysis of asymmetrical GNRI-TL was performed and new equations presented for the calculation of the dispersion characteristics and component values. A dual-band bandpass filter was simulated using the theory developed.

A quad-band Wilkinson power divider has been designed and tested for the first time, using the extended GNRI-TL theory. Simulated and measured results were shown. A GNRI-TL quad-band Rat-race Coupler has also been implemented for the first time and its simulated and measured results were presented. Another contribution was the design of a quad-band shorted $\lambda/4$ bandpass filter using GNRI-TL unit cells.

A more complete model of the GNRI-TL unit cell was also presented, which includes the effects of a realistic host transmission line, including its resistance and conductance. After the evaluation of the host transmission parameters, an equivalent model has been created to verify its validity and its dispersion characteristics analyzed. Subsequently, a method was shown for making all the necessary corrections to the original GNRI-TL unit cell, using new equations that keep the unit cell in the closed stopband condition. Example designs have been calculated and the effects of the transmission line parameters that cannot be rectified were quantified.

The end result of this work was to develop the tools that enable the microwave device designer to build dual and quad-band metamaterial circuitry with confidence and reliability. Through the device implementation in this work, the necessary theory has been laid down that yields a good first approximation in the required GNRI-TL unit cell component values. A methodology has been put in place that shows the way to use the unit cells into useful multiband devices, through proper simulation and modeling. Fabrication techniques that can be used have also been detailed for the specific case of a quad-band divider, a rat-race coupler and a bandpass filter.

6.2 Future work

One of the limitations of LC loaded metamaterial structures is their limited power handling capability. For high-power applications, such as satellite and radar front ends, bulky waveguide components are typically used. As an extension to the NRI-TL and GNRI-TL theory, the way to load the waveguide with the necessary inductive and capacitive elements could be found, so that new waveguide structures can be developed that benefit from the unconventional properties of metamaterials. Waveguide phase shifters for example, typically depend on the electrical length of the waveguide itself. A metamaterial waveguide phase shifter could potentially reduce the size of the structure, while keeping the high-power benefits that a waveguide device offers. Metamaterial devices have been already implemented using substrate-integrated waveguide (SIW) technology (see [25]), which is already a small form-factor planar waveguide structure. Similar techniques for loading the waveguide (e.g. using slots instead copper etching) can thus be used in full-height waveguide structures in order to take advantage of their high power-handling capabilities.

Another extension to this research could be done by using the very broadband characteristics of the lattice, but more preferably the bridged-T configuration of the dual and quad-band unit cell. If the fabrication difficulties could be overcome, then the all-pass behavior of these types of unit cells, could result in microwave devices that perform better and over wider bandwidth than the simpler NRI-TL and GNRI-TL counterparts. Such very broadband devices can find immediate use in electronic warfare and countermeasure applications, where the operating frequency range of a single system might be anywhere between 0.5-18 GHz.

Whereas metamaterial matching networks have been used previously in antenna applications [119], [120], they have not been seen in the literature for amplifier matching, with the exception of [122], where a dual-band matching network has been designed using CRLH-TL's. It would be more useful however to exploit the potential of the GNRI-TL structures for quad-band amplifier impedance matching, where a single unit cell could provide λ/4 or 3λ/8 TL sections with the desired impedances at four arbitrary frequencies simultaneously. This application is considered to be a very logical extension of this work since all the necessary tools have been developed in the Thesis to ensure successful realizable designs. By following the same methodology used in the process of transforming a single-band device (e.g. Wilkinson, rat-race, shorted $\lambda/4$ bandpass filter) to a quad-band device, a conventional amplifier design can be also transformed to support quad-band operation as long as the active device has sufficient bandwidth to cover the desored frequencies.

Other devices that could be implemented using GNRI-TL unit cells are step recovery diode multipliers, where the λ/4 TL section at the output as well as the subsequent filtering, could be through GNR-TL designs. Transmit- receive (TR) switches could also benefit from GNRI-TL's where again, the conventional TL sections could be replaced accordingly and provide multiband isolation between transmitter, receiver and antenna.

Any true multiband system requires the antenna to operate at the design frequencies simultaneously. Metamaterials enable physically small but electrically large air-interface components, with minimal coupling among closely spaced devices. The metamaterial antenna field has boomed in recent years, however the GNRI-TL structure has not been examined in detail so for an antenna implementation, except for the case of [123], where a leaky wave antenna has been designed using an SIW extended-composite right/ left-handed (E-CRLH) unit cell.

Finally, another potentially interesting application of metamaterials, would be their application to non-reciprocal devices, namely isolators and circulators. The dominant technology for these devices uses magnetically biased ferrites, which makes them bulky and incompatible with planar fabrication technologies. Even though [125] and [126] have examined one way of implementing such devices using metamaterials, the possibility of using NRI-TL and GNRI-TL technology for this purpose might give the added benefit of the ease and versatility of the design and fabrication process.

7 References

[1] V.G. Veselago, “The elelctrodynamics of substances with simultaneously negative values of ε and μ,” Sov. Phys. Ups., vol. 10, pp. 509-514, Jan.-Feb. 1968.

[2] R. A. Shelby, D. R. Smith, S. Schultz, “Experimental verification of a negative index of refraction,” *Science*, vol. 292, pp. 77-79, 6 April 2001.

[3] D.R. Smith, W.J. Padilla, D.C. Vier, S.C. Nemat-Nasser, and S. Schultz, “Composite medium with simultaneously negative permeability and permittivity,” *Phys.Rev. Lett.*, vol. 84, no. 18, pp. 4184–4187, May 2000.

[4] A. K. Iyer, G. V. Eleftheriades, “Negative refractive index metamaterials supporting 2-D waves,” *IEEE MTT-S Int. Microwave Symp. Dig.*, vol. 2, Seattle, WA, pp. 1067–1070, June 2–7, 2002.

[5] M. A. Antoniades and G. V. Eleftheriades, “Compact linear lead/ lag metamaterial phase shifters for broadband applications,” *IEEE Antennas Wireless Propag. Lett.*, vol. 2, pp. 103-106, 2003.

[6] H. Kim, A. Kozyrev, A. Karbassi, and D.W. van der Weide, “Linear tunable phase shifter using a left-handed transmission line,” *IEEE Microw. Wireless Compon.Lett.*, vol. 15, no. 5, pp. 366–368, May 2005.

[7] C. Damm, M. Schussler, M. Oertel, and R. Jakoby, “Compact tunable periodically LC loaded microstrip line for phase shifting applications,” in *Proc. IEEE Int.Microw. Symp.*, Long Beach, CA, Jun. 2005, pp. 2003–2006.

[8] D. Kuylenstierna, A. Vorobiev, P. Linner, and S. Gevorgian, “Composite right/left handed transmission line phase shifter using ferroelectric varactors,” *IEEE Microw.Wireless Compon. Lett.*, vol. 16, no. 4, pp. 167–169, Apr. 2006

[9] R. Islam and G. V. Eleftheriades, “A planar metamaterial co-directional coupler that couples power backwards,” in Proc. IEEE Intl. Symp. On Microwave Theory and Tech., vol. 1, Philadelphia, PA, June 2003, pp. 321-324.

[10] G.V. Eleftheriades, A. Grbic, and M.A. Antoniades, “Negative-refractive-index transmission-line metamaterials and enabling electromagnetic applications,” in *Proc. IEEE Int. Symp. Antennas and Propag.*, vol. 2, Monterey, CA, Jun. 2004,pp. 1399–1402.

[11] R. Islam, F. Elek, and G.V. Eleftheriades, “Coupled-line metamaterial coupler having co-directional phase but contra-directional power flow,” *Electronics Letters,* vol. 40, no. 5, pp. 315–317, Mar. 2004.

[12] M. A. Antoniades and G. V. Eleftheriades, "A broadband 1:4 series power divider using metamaterial phase-shifting lines," *Microwave Conference, 2005 European* , vol.2, no., pp.4 pp.,, 4-6 Oct. 2005.

[13] R. Islam and G.V. Eleftheriades, “Printed high-directivity metamaterial MS/NRI coupled-line coupler for signal monitoring applications,” *IEEE Microw. WirelessCompon. Lett.*, vol. 16, no. 4, pp. 164–166, Apr. 2006.

[14] C. Caloz and T. Itoh, “Novel microwave devices and structures based on the transmission line approach of meta-materials” 2003 IEEE Intl. Microwave Symposium Digest, pp. 195 -198, June 2003.

[15] I.-H. Lin, M. De Vincentis, C. Caloz,and T. Itoh, “Arbitrary dual-band components using composite right/left handed transmission lines,” *IEEE Trans. Microwave. Theory Tech.*, vol. 52, no. 4, pp. 1142–1149, Apr.2004.

[16] P.-L. Chi, C.-J. Lee, and T. Itoh, “A compact dual-band metamaterial-based ratrace coupler for a MIMO system application,” in *Proc. IEEE Int. Microw. Symp.*, Atlanta, GA, Jun. 2008, pp. 667–670.

[17] G. V. Eleftheriades, “A generalized negative-refractive-index transmission- line (NRI-TL) metamaterial for dual-band and quad-band applications,” *IEEE Microw. Wireless Compon. Lett.*, vol. 17, no. 6, pp. 415–417, Jun. 2007.

[18] A. C. Papanastasiou, G. E. Georghiou, and G. V. Eleftheriades, "A quadband Wilkinson power divider using Generalized NRI Transmission Lines," *Microwave and Wireless Components Letters,* IEEE, vol. 18, pp. 521-523, 2008.

[19] A. Sanada, C. Caloz, and T. Itoh, “Planar distributed structures with negative refractive index,” *IEEE Trans. Microw. Theory Tech.*, vol. 52, no. 4, pp. 1252–1263, Apr. 2004.

[20] M.A. Antoniades and G.V. Eleftheriades, “A broadband series power divider using zero-degree metamaterial phase-shifting lines,” *IEEE Microw. Wireless Compon.Lett.*, vol. 15, no. 11, pp. 808–810, Nov. 2005.

[21] P. de Paco, R. Villarino, G. Junkin, O. Menéndez, E. Corrales and J Parrón, “A dual-band mixer using composite right/left-handed transmission lines,” *IEEE Microwave Wireless Component Letters*, vol. 17, no. 8, August, 2007.

[22] Pei-Ling Chi, Cheng-Jung Lee, and Tatsuo Itoh, “A compact dual-band metamaterial-based rat-race coupler for a MIMO system application,” *IEEE MTT-S International Microwave Symposium Digest*, pp. 667-670, June 2008.

[23] G. Sisó, J. Bonache and F. Martín, Dual-band Rat Race Hybrid Coupler Implemented Through Artificial Lines Based on Complementary Split Ring Resonators, *IEEE International Microwave Symposium* 2009,625-628.

[24] G. Siso, J. Bonache, and F. Martin, “Dual-band rat race hybrid coupler implemented through artificial lines based on complementary split ring resonators," *International Microw. Symp. Digest*, 625-628, Jun. 2010.

[25] D. Yuandan. and T. Itoh, "Application of composite right/left-handed half-mode substrate integrated waveguide to the design of a dual-band rat-race coupler," *International Microw. Symp. Digest*, 712-715, 2010.

[26] G. V. Eleftheriades, “Design of generalised negative-refractive-index transmission lines for quad-band applications,” *IET Antennas and Propagation*, vol. 4, no. 8, pp. 977-981, 2010.

[27] I. H. Lin, C. Caloz, and T. Itoh, "A branch-line coupler with two arbitrary operating frequencies using left-handed transmission lines," in 2003 IEEE MTT-S Int. Microwave Symp. Dig., pp. 325-328.

[28] I. H. Lin, M. DeVincentis, C. Caloz, and T. Itoh, "Arbitrary dual-band components using composite right/left-handed transmission lines," *IEEE Trans. Microwave Theory and Tech*., vol. 52, pp. 1142-1149, Apr. 2004.

[29] B.H. Chen, Y.N. Zhang, D. Wu, K. Seo, "Novel composite right/left-handed transmission line for quad-band applications," *Communication Systems, 2008. ICCS 2008. 11th IEEE Singapore International Conference on* , vol., no., pp.617,620, 19-21 Nov. 2008

[30] A. Dupuy, A. Gummalla, M. Achour, G. Poilasne, “Compact Single and Dual Zero-degree Metamaterial Nway Radial Power Combiner/Divider,” *Microwave Symposium Digest, 2008 IEEE MTT-s International*, pp. 659-662, June 2008.

[31] C.-H. Tseng and T. Itoh, “Dual-band bandpass and bandstop filters using composite right/left-handed metamaterial transmission lines,” in *Proc. IEEE Int. Microw.Symp.*, San Fransisco, CA, Jun. 2006, pp. 931–934.

[32] R. Islam and G.V. Eleftheriades, “Elliptic-type bandpass filter and bandstop notch filter inspired by metamaterial NRI-TL topology,” *Electronics Letters*, vol. 44,no. 25, pp. 1470–1472, Dec. 2008.

[33] D. S. Elles, Yoon Yong-Kyu, “Compact dual-band three way bagley polygon power divider using composite right/ left handed (CRLH) transmission lines, ” *Microwave Symposium Digest, 2009 IEEE MTT-s International*, pp. 485-488, June 2009.

[34] K.C. Gupta, R. Garg, I.Bahl, P. Bhartia, *Microstrip lines and slotlines*, 2nd ed. Boston: Artech House, 1996, pp. 105, 129-131.

[35] G. Matthaei, L. Young, and E.M.T. Jones, *Microwave Filters, Impedance-Matching Networks, and Coupling Structures*. Norwood, MA: Artech House, 1980.

[36] G.V. Eleftheriades, A.K. Iyer and P.C. Kremer, "Planar negative refractive index media using periodically L-C loaded transmission lines," *IEEE Trans. on Microwave Theory and Techniques*, vol. 50, no. 12, pp. 2702-2712, Dec. 2002.

[37] C. Caloz and T. Itoh, “Novel microwave devices and structures based on the transmission-line approach of metamaterials,” *IEEE MTT-S International Microwave Symposium*, pp. 195-198, vol. 1, June 2003.

[38] A. Rennings, S. Otto, J. Mosig, C. Caloz, and I. Wolff, "Extended composite right/left-handed metamaterial and its application as quadband quarter-wavelength transmission line," in Proc. Asia-Pacific Microwave Conference (APMC), Yokohama, Japan, Dec. 2006.

[39] M. Studniberg and G.V. Eleftheriades, “Physical Implementation of a generalized NRI-TL medium for quad-band applications,” *European Microwave Conference*, Munich, Germany, Oct. 2007.

[40] R. Islam and G.V. Eleftheriades, “Phase-agile branch-line couplers using metamaterial lines,” *IEEE Microw.Wireless Compon. Lett.*, vol. 14, no. 7, pp. 340–342, Jul. 2004.

[41] H. Okabe, C. Caloz, and T. Itoh, “A compact enhanced-bandwidth hybrid ring using an artificial lumped-element left-handed transmission-line section,” *IEEE Trans. Microw. Theory Tech.*, vol. 52, no. 3, pp. 798–804, Mar. 2004.

[42] D.M. Pozar, *Microwave Engineering*, 2nd ed. New York: Wiley, 1998, pp. 363-367.

[43] G. V. Eleftheriades and R. Islam, “Miniaturized microwave components and antennas using negative-refractive-index transmission-line (NRI-TL) metamaterials,” *Metamaterials*, vol.1, pp. 53-61, 2007.

[44] I. A. Mocanu, T. Petrescu, “Novel Dual Band Hybrid Rat-Race Coupler with CRLH and D-CRLH Transmission Lines”, Proceedings of the Asia-Pacific Microwave Conference 2011

[45] L. Piazzon, P. Saad, P. Colantonio, F. Giannini , K. Andersson and C. Fager, “Branch-Line Coupler Design Operating in Four Arbitrary Frequencies”, *Microwave and Wireless Components Letters*, IEEE, vol. 22, pp. 67-69, 2012.

[46] M. A. Antoniades and G. V. Eleftheriades, “A folded-monopole model for electrically small NRI-TL metamaterial antennas," *IEEE Antennas and Wireless Propagation Letters*, Vol. 4, 333-336, September 2005.

[47] A. Grbic and G.V Eleftheriades, “Periodic analysis of a 2-D negative refractive index transmission line structure,” *IEEE Microwave Wireless Compon. Lett.*, vol. 51, no. 10, pp. 2604–2611, Oct. 2003.

[48] G.V. Eleftheriades, O. Siddiqui, and A.K. Iyer, “Transmission line models for negative refractive index media and associated implementations without excess resonators,’’ *IEEE Microwave Wireless Compon. Lett.*, vol. 13, no. 2, pp. 51–53, Feb. 2003

[49] A. Gummalla, C. Lee, M. Achour, “Compact metamaterial quadband antenna for mobile application”, *Antennas and Propagation Society International Symposium,* 2008. AP-S 2008. IEEE

[50] M. A. Antoniades and G. V. Eleftheriades, “A broadband dual-mode monopole antenna using NRI-TL metamaterial loading," *IEEE Antennas Wireless Propag. Lett.* , No. 8, 258-261, 2009.

[51] J.-X. Niu,, “Dual-band dual-mode patch antenna based on resonant-type metamaterial transmission line," *Electron. Lett.*, Vol. 46, No. 4, 266-268, 2010.

[52] Zhu, J., M. A. Antoniades, and G. V. Eleftheriades, “A compact tri-band monopole antenna with single-cell metamaterial loading," IEEE Trans. Antennas Propag. , Vol. 54, No. 8, 1031-1038, 2010.

[53] M. Durán-Sindreu, G. Sisó, J. Bonache, F. Martin, "Planar Multi-Band Microwave Components Based on the Generalized Composite Right/Left Handed Transmission Line Concept", *Microwave Theory and Techniques*, IEEE Transactions on, On page(s): 3882 - 3891 Volume: 58, Issue: 12, Dec. 2010

[54] J. Selga, A. Rodriguez, V.E. Boria, F. Martin, "Synthesis of Split-Rings-Based Artificial Transmission Lines Through a New Two-Step, Fast Converging, and Robust

Aggressive Space Mapping (ASM) Algorithm", *Microwave Theory and Techniques, IEEE Transactions on,* On page(s): 2295 - 2308 Volume: 61, Issue: 6, June 2013

[55] M. Bemani, S. Nikmehr, "Dual-Band N-Way Series Power Divider Using CRLH-TL Metamaterials With Application in Feeding Dual-Band Linear Broadside Array Antenna With Reduced Beam Squinting", *Circuits and Systems I: Regular Papers, IEEE Transactions on,* On page(s): 3239 - 3246 Volume: 60, Issue: 12, Dec. 2013

[56] Lijuan Su; Naqui, J.; Mata-Contreras, J.; Martin, F. "Modeling Metamaterial Transmission Lines Loaded With Pairs of Coupled Split-Ring Resonators", *Antennas and Wireless Propagation Letters, IEEE,* On page(s): 68 - 71 Volume: 14, 2015

[57] G. Siso, J. Bonache, F. Martin, "Dual-band rat race hybrid coupler implemented through artificial lines based on complementary split ring resonators", *Microwave Symposium Digest, 2009. MTT '09. IEEE MTT-S International,* On page(s): 625 – 628

[58] M.A. Fouad, M.A. Abdalla, "A compact and new CPW dual BPF based on generalized metamaterial CRLH transmission line", *Antennas and Propagation Society International Symposium (APSURSI), 2013 IEEE,* On page(s): 628 – 629

[59] M. Durán-Sindreu, G. Sisó, J. Bonache, F. Martín, "Fully planar implementation of generalized composite right/left handed transmission lines for quad-band applications", *Microwave Symposium Digest (MTT), 2010 IEEE MTT-S International,* On page(s): 25 – 28

[60] D. Draskovic, D. Budimir, "Quad-band power dividers with generalized NRI metamaterial transmission lines", *Antennas and Propagation Society International Symposium, 2009. APSURSI '09. IEEE,* On page(s): 1 – 4

[61] A.C. Papanastasiou, G.E. Georghiou, G.V. Eleftheriades, "A quad-band rat-race coupler based on the Generalized Negative Refractive-Index Transmission-Line concept", *Microwave Conference (EuMC), 2013 European,* On page(s): 302 - 305, Volume: Issue: , 6-10 Oct. 2013.

[62] M. Durán-Sindreu, J. Bonache, F. Martin, "Compact CPW dual-band bandpass filters based on semi-lumped elements and metamaterial concepts", *Microwave Conference Proceedings (APMC), 2010 Asia-Pacific,* On page(s): 670 - 673, Volume: Issue: , 7-10 Dec. 2010.

[63] M. Durán-Sindreu, J. Bonache, F. Martin, T. Itoh, "Novel fully-planar extended-composite right/left handed transmission line based on substrate integrated waveguide for multi-band applications", *Microwave Conference (EuMC), 2012 42nd European,* On page(s): 578 - 581, Volume: Issue: , Oct. 29 2012-Nov. 2012.

[64] C.G.M. Ryan and G.V. Eleftheriades, “A single-ended all-pass generalized negative-refractive-index transmission-line using a Bridged-T circuit”, *IEEE Intl. Microwave Symposium*, Montreal, Canada, 3 pages, June 17-22, 2012.

[65] S. Ramo, J.R. Whinnery, and T. Van Duzer, *Fields and Waves in Communication Electronics,* 3rd ed. New York, NY: John Wiley & Sons, 1994.

[66] G.V. Eleftheriades, A.K. Iyer, and P.C. Kremer, “Planar negative refractive index media using periodically L-C loaded transmission lines,” *IEEE Trans. Microw. Theory Tech.*, vol. 50, no. 12, pp. 2702–2712, Dec. 2002.

[67] G.V. Eleftheriades and K.G. Balmain, Eds., *Negative-Refraction Metamaterials: Fundamental Principles and Applications*. Hoboken, NJ: John Wiley & Sons, 2005.

[68] C.Caloz, T.Itoh *"Electromagnetic Metamaterials"*, IEEE press, Wiley, Hoboken NJ, 2006.

[69] J.-S. Hong, *Microstrip Filters for RF/Microwave Applications*, John Wiley & Sons, Hoboken, NJ, USA, 2nd edition, 2011

[70] R. E. Collin, *Foundations for Microwave Engineering*, 2nd ed. New York, NY: McGraw-Hill, 1992.

[71] A. Lai, T. Itoh, and C. Caloz, “Composite right/left-handed transmission line metamaterials,” *IEEE Microwave Magazine*, vol. 5, no. 3, pp. 34–50, Sept. 2004.

[72] F. Bongard, J. Perruisseau-Carrier, J.R. Mosig, “Enhanced CRLH transmission line performances using a lattice network unit cell”, *IEEE Microw. Wireless Comp. Lett*., vol. 19, pp. 431-433, July 2009.

[73] J. Esteban, C. Camacho-Penalosa, J. E. Page, and T. M. Martin-Guerrero, “Generalized lattice network-based balanced composite right-/left-handed transmission lines,” *IEEE Trans. Microw. Theory Techn.*,vol. 60, no. 8, pp. 2385–2393, Aug. 2012.

[74] M.A. Antoniades and G.V. Eleftheriades, “A broadband Wilkinson balun using microstrip metamaterial lines,” *IEEE AntennasWireless Propag. Lett.,* vol. 4, no. 1,pp. 209–212, 2005.

[75] Y. Dong and T. Itoh, “Composite right/left-handed substrate integrated waveguide and half-mode substrate integrated waveguide,” in IEEE MTT-S Int. Microw. Symp. Dig., Boston, 2009, pp. 49–52.

[76] Y. Dong; Itoh, T. "Composite Right/Left-Handed Substrate Integrated Waveguide and Half Mode Substrate Integrated Waveguide Leaky-Wave Structures", *Antennas*

and Propagation, IEEE Transactions on, On page(s): 767 - 775 Volume: 59, Issue: 3, March 2011.

[77] F. Falcone, et al, "Effective negative ε−stop-band microstrip lines basedd on complementary split ring resonators,"*IEEE Microw. Wireless Compon. Lett*., vol. 14, no. 6, pp. 280-282, Jun.2004.

[78] F. Falcone et al, "Babinet principle applied to the design of metasurfaces and metamaterials,"*Phys. Rev. Lett*., vol. 93, pp. 197401:1-4, Nov. 2004.

[79] A. Sanada, et al, "Characteristics of the composite right/left-handed tranmission lines," IEEE *Microw. Wireless Compon. Lett*, vol. 14, no. 2, pp. 68-70, Feb. 2004.

[80] G. Sisó, J. Bonache, and F. Martín, "Dual-band Y-junction power dividers implemented through artificial lines based on complementary resonators," *IEEE MTT-S Int. Dig*., Atlanta, GA, Jun. 2008, pp.663–666.

[81] C.-H. Tseng and C.-L. Chang, "Wide-band balun using composite right/left-handed transmission line," *Electronics Letters*, vol. 43, no. 21, pp. 1154–1155, Oct. 2007.

[82] G. Siso, M. Gil, J. Bonache, F. Martin, "Generalized Model for Multiband Metamaterial Transmission Lines", *Microwave and Wireless Components Letters, IEEE*, On page(s): 728 - 730 Volume: 18, Issue: 11, Nov. 2008

[83] N. Engheta and R.W. Ziolkowski, Eds., *Metamaterials: Physics and Engineering Explorations.* Hoboken, NJ: John Wiley & Sons, 2006.

[84] R. Marques, F. Martin, and M. Sorolla, *Metamaterials with Negative Parameters: Theory, Design and Microwave Applications.* Hoboken, NJ: John Wiley & Sons,2007.

[85] G.V. Eleftheriades, "Analysis of bandwidth and loss in negative-refractive-index transmission-line (NRI-TL) media using coupled resonators," *IEEE Microw. WirelessCompon. Lett*., vol. 17, no. 6, pp. 412–414, Jun. 2007.

[86] S.-G. Mao and Y.-Z. Chueh, "Broadband composite right/left-handed coplanar waveguide power splitters with arbitrary phase responses and balun and antenna applications," *IEEE Trans. Antennas Propag*., vol. 54, no. 1, pp. 243–250, Jan. 2006.

[87] C.-H. Tseng and C.-L. Chang , "A broadbanad quadrature power splitter using metamaterial transmission line," *IEEE Microw. Wireless Compon. Lett*., vol. 18, no. 1, pp. 25–27, Jan. 2008

[88] Cheng-Jung Lee; Leong, K.M.K.H.; Itoh, T., "Broadband Quadrature Hybrid Design Using Metamaterial Transmission Line and Its Application in the Broadband

Continuous Phase Shifter," *Microwave Symposium, 2007. IEEE/MTT-S International* , vol., no., pp.1745,1748, 3-8 June 2007

[89] L. Markley, G.V. Eleftheriades, "Quad-band negative-refractive-index transmission-line unit cell with reduced group delay," *Electronics Letters* , vol.46, no.17, pp.1206,1208, August 19 2010.

[90] P. Velez, M. Duran-Sindreu, J. Bonache, F. Martin, "Compact right-handed (RH) and left-handed (LH) lattice-network unit cells implemented in monolayer printed circuits," *Microwave Conference Proceedings (APMC), 2011 Asia-Pacific* , vol., no., pp.534,537, 5-8 Dec. 2011

[91] Rennings, S. Otto, J. Mosig, C. Caloz and I. Wolff, "Extended composite right/left-handed (E-CRLH) metamaterial and its application as quadband quarter-wavelength transmission line", *Asia-Pacific Microwave Conference (APMC)*, Yokohama, Japan, December 2006.

[92] J. Mata-Contreras, T.M. Martin-Guerrero, C. Camacho-Peñalosa, "Assessment of a Composite Right/Left-Handed Transmission Line-based Distributed Amplifier implemented in microstrip technology," *Microwave Conference, 2006. 36th European* , vol., no., pp.1586,1589, 10-15 Sept. 2006.

[93] Chenggang Xie, "Directional dual band distributed power amplifier with composite left/right-handed transmission lines," *Microwave Symposium Digest, 2008 IEEE MTT-S International* , vol., no., pp.1135,1138, 15-20 June 2008 doi: 10.1109/MWSYM.2008.4633257.

[94] R. Keshavarz, A. Mohammadi, A. Abdipour, "A Quad-Band Distributed Amplifier With E-CRLH Transmission Line," *Microwave Theory and Techniques, IEEE Transactions on* , vol.61, no.12, pp.4188,4194, Dec. 2013.

[95] Jaewon Choi; Seungin Yang; Yong Moon; Changkun Park; Byung-Jun Jang; Jun-Kyung Cho; Chulhun Seo, "Quad-band inverse class-F power amplifier using novel composite right/left-handed transmission line," *Microwave Symposium Digest (MTT), 2010 IEEE MTT-S International* , vol., no., pp.1078,1081, 23-28 May 2010.

[96] T. Kokkinos, A.P. Feresidis, J.C. Vardaxoglou, "Analysis and Application of Metamaterial Spiral-Based Transmission Lines," *Antenna Technology: Small and Smart Antennas Metamaterials and Applications, 2007. IWAT '07. International Workshop on* , vol., no., pp.233,236, 21-23 March 2007.

[97] R. Islam, G.V. Eleftheriades, "Compact Negative-Refractive-Index Transmission-Line (NRI-TL) coupler, filter and diplexer," *Antennas and Propagation Society International Symposium, 2007 IEEE* , vol., no., pp.4957,4960, 9-15 June 2007.

[98] V. Gonzalez-Posadas, J.L. Jimenez-Martin, L.E. Garcia-Munoz, D. Segovia-Vargas, "Novel Diplexer made with Dual-Composite Right/Left-Handed Lines (D-CRLH)," *Microwave Techniques, 2008. COMITE 2008. 14th Conference on* , vol., no., pp.1,4, 23-24 April 2008

[99] Kuan Deng; Wenquan Che; Chao Li; Russer, P., "Novel microwave diplexer system based on planar waveguide and metamaterial technologies," *Microwave Conference, 2008. APMC 2008. Asia-Pacific* , vol., no., pp.1,4, 16-20 Dec. 2008 doi: 10.1109/APMC.2008.4958656.

[100] Changjun Liu; Menzel, W., "A microstrip diplexer from metamaterial transmission lines," *Microwave Symposium Digest, 2009. MTT '09. IEEE MTT-S International* , vol., no., pp.65,68, 7-12 June 2009.

[101] M.M Mansour, A.-A.T. Shalaby, E.-S.M El-Rabaie, N.W.Messiha, "Design and simulation of microwave diplexer based on D-CRLH metamaterials," *Engineering and Technology (ICET), 2014 International Conference on* , vol., no., pp.1,5, 19-20 April 2014.

[102] A. Dupuy, K.M.K.H Leong, R. Staraj., G. Jacquemod T. Itoh, "Inverse Class-F Power Amplifier Using Composite Right/Left-Handed Transmission Lines as a Harmonic Trap," *Microwave Conference, 2006. 36th European* , vol., no., pp.360,363, 10-15 Sept. 2006.

[103] K. Murase.; R. Ishikawa, K. Honjo, "Group delay compensation technique for UWB MMIC using composite right/left-handed circuit," *Microwave Conference, 2006. APMC 2006. Asia-Pacific* , vol., no., pp.1409,1412, 12-15 Dec. 2006.

[104] Chao-Hsiung Tseng; Chih-Lin Chang, "Microwave push-pull oower amplifier using metamaterial-based baluns," *Microwave Conference, 2008. APMC 2008. Asia-Pacific* , vol., no., pp.1,4, 16-20 Dec. 2008.

[105] Chao-Hsiung Tseng; Chih-Lin Chang, "Improvement of Return Loss Bandwidth of Balanced Amplifier Using Metamaterial-Based Quadrature Power Splitters," *Microwave and Wireless Components Letters, IEEE* , vol.18, no.4, pp.269,271, April 2008.

[106] Chenggang Xie, "Directional dual band distributed power amplifier with composite left/right-handed transmission lines," *Microwave Symposium Digest, 2008 IEEE MTT-S International* , vol., no., pp.1135,1138, 15-20 June 2008.

[107] O.G. Perez, A. Garcia-Lamperez, V. Gonzalez-Posadas, M. Salazar-Palma, D. Segovia-Vargas, "Dual-Band Recursive Active Filters With Composite Right/Left-Handed Transmission Lines," *Microwave Theory and Techniques, IEEE Transactions on* , vol.57, no.5, pp.1180,1187, May 2009.

[108] Wei Fei; Hao Yu; Kiat Seng Yeo; Xiong Liu; Wei Meng Lim, "A 44-to-60GHz, 9.7dBm P1dB, 7.1% PAE power amplifier with 2D distributed power combining by metamaterial-based zero-phase-shifter in 65nm CMOS," *Microwave Symposium Digest (MTT), 2012 IEEE MTT-S International* , vol., no., pp.1,3, 17-22 June 2012.

[109] Kyoung Youl Park; Wiwatcharagoses, N.; Chahal, P., "A metamaterial-inspired high-Q X-band oscillator," *Antennas and Propagation Society International Symposium (APSURSI), 2012 IEEE* , vol., no., pp.1,2, 8-14 July 2012 doi: 10.1109/APS.2012.6349272.

[110] J.S. Hummelt, W.C. Guss, M.A. Shapiro, R.J. Temkin, "Design of a high power S-band amplifier utilizing a metamaterial interaction cavity," *Plasma Science (ICOPS), 2013 Abstracts IEEE International Conference on* , vol., no., pp.1,1, 16-21 June 2013.

[111] Ki-Cheol Yoon; Jaegook Lee; Hyunwook Lee; Jong-Chul Lee, "Low noise and high gain dual-band active band-pass filter with GaAs MESFET using CRLH metamaterial," *Microwave Conference Proceedings (APMC), 2013 Asia-Pacific* , vol., no., pp.697,699, 5-8 Nov. 2013.

[112] R. Keshavarz, A. Mohammadi, A. Abdipour, "A Quad-Band Distributed Amplifier With E-CRLH Transmission Line," *Microwave Theory and Techniques, IEEE Transactions on* , vol.61, no.12, pp.4188,4194, Dec. 2013 doi: 10.1109/TMTT.2013.2288939.

[113] R. Islam, G.V. Eleftheriades, "A compact highly-selective filter inspired by Negative-Refractive-Index Transmission Lines," *Microwave Symposium Digest, 2008 IEEE MTT-S International* , vol., no., pp.895,898, 15-20 June 2008.

[114] M. Studniberg, G.V. Eleftheriades, "A Dual-Band Bandpass Filter Based on Generalized Negative-Refractive-Index Transmission-Lines," *Microwave and Wireless Components Letters, IEEE* , vol.19, no.1, pp.18,20, Jan. 2009.

[115] M.A. Antoniades, B. Henin, A. Abbosh, "A compact crossover using NRI-TL metamaterial lines," *Antennas and Propagation Society International Symposium (APSURSI), 2012 IEEE* , vol., no., pp.1,2, 8-14 July 2012.

[116] S. Simion, G. Sajin, R. Marcelli, G. Bartolucci, "Frequency doubler and short pulse generator, based on nonlinear composite right/left-handed transmission line," *Microwave Conference, 2008. APMC 2008. Asia-Pacific* , vol., no., pp.1,4, 16-20 Dec. 2008.

[117] R. Islam, G.V. Eleftheriades, "Compact Corporate Power DividerUsing Metamaterial NRI-TLCoupled-Line Couplers," *Microwave and Wireless Components Letters, IEEE* , vol.18, no.7, pp.440,442, July 2008.

[118] P. Velez, M. Duran-Sindreu, A. Fernandez-Prieto, J. Bonache, F. Medina, F. Martin, "Compact Dual-Band Differential Power Splitter With Common-Mode Suppression and Filtering Capability Based on Differential-Mode Composite Right/Left-Handed Transmission-Line Metamaterials," *Antennas and Wireless Propagation Letters, IEEE* , vol.13, no., pp.536,539, 2014.

[119] M. Selvanayagam, G.V. Eleftheriades, "A Compact Printed Antenna With an Embedded Double-Tuned Metamaterial Matching Network," *Antennas and Propagation, IEEE Transactions on* , vol.58, no.7, pp.2354,2361, July 2010.

[120] T. Kokkinos, A.P. Feresidis, J.C. Vardaxoglou, "A Low-Profile Monopole-Like Small Antenna with Embedded Metamaterial Spiral-Based Matching Network," *Antennas and Propagation, 2007. EuCAP 2007. The Second European Conference on* , vol., no., pp.1,5, 11-16 Nov. 2007.

[121] T. Kawai, M. Nakamura, S. Tanigawa, I. Ohta, A. Enokihara, "Band-broadening design technique of CRLH-TLs branch-line couplers operating at two arbitrary frequencies using CRLH-TLs matching networks," *Microwave Conference, 2009. EuMC 2009. European* , vol., no., pp.1295,1298, Sept. 29 2009-Oct. 1 2009.

[122] Seung Hun Ji; Choon Sik Cho; Lee, J.W.; Jaeheung Kim, "Concurrent Dual-Band Class-E Power Amplifier Using Composite Right/Left-Handed Transmission Lines," *Microwave Theory and Techniques, IEEE Transactions on* , vol.55, no.6, pp.1341,1347, June 2007.

[123] M. Duran-Sindreu, Jun Choi; J. Bonache, F. Martin, T. Itoh, "Dual-band leaky wave antenna with filtering capability based on extended-composite right/left-handed transmission lines," *Microwave Symposium Digest (IMS), 2013 IEEE MTT-S International* , vol., no., pp.1,4, 2-7 June 2013.

[124] M. Studniberg, G,V, Eleftheriades, "A quad-band bandpass filter using negative-refractive-index transmission-line (NRI-TL) metamaterials," *Antennas and Propagation Society International Symposium, 2007 IEEE* , vol., no., pp.4961,4964, 9-15 June 2007.

[125] T. Kodera, D.L. Sounas, C. Caloz, "Tunable magnet-less non-reciprocal metamaterial (MNM) and its application to an isolator," *Microwave Conference Proceedings (APMC), 2012 Asia-Pacific* , vol., no., pp.73,75, 4-7 Dec. 2012.

[126] T. Kodera, D.L. Sounas, C. Caloz, "Magnetless Nonreciprocal Metamaterial (MNM) Technology: Application to Microwave Components," *Microwave Theory and Techniques, IEEE Transactions on* , vol.61, no.3, pp.1030,1042, March 2013.